# ADDITIVE MANUFACTURING OF 3D PRINTED SIC COMPOSITES: STRENGTHENING AND DENSIFICATION THROUGH SURFACE MODIFICATION AND USE OF MINERAL BINDERS

by

Sujithra Chandrasekaran

A dissertation submitted to the faculty of
The University of North Carolina at Charlotte
in partial fulfillment of the requirements
for the degree of Doctor of Philosophy in
Mechanical Engineering

Charlotte

2023

Approved by:

_____
Dr. Ahmed El-Ghannam

_____
Dr. Harish Cherukuri

_____
Dr. Youxing Chen

_____
Dr. Charles Lee

_____
Dr. Didier Dreau

# ABSTRACT

SUJITHRA CHANDRASEKARAN. Additive Manufacturing of 3D printed SiC Composites: Strengthening and densification through Surface Modification and use of Mineral Binders.
(Under the direction of DR. AHMED EL-GHANNAM)

Manufacturing of dense SiC composites counts mainly on the thermal oxidation of the carbide into silica. The irregularity of the silica layer and its limited thickness weaken the bond between particles and diminish the good thermo-mechanical properties of SiC making it highly unfavorable for many applications. In the present study, a novel sintering method to produce highly dense and strong SiC composites using mineral binders such as cordierite and spodumene is introduced. To overcome the poor quality of the silica layer formed by thermal oxidation we chemically created a silica gel layer by alkali treatment. Rapid prototyping of ceramic bodies using the powder binder jetting technique has been gaining attention in the past few years to overcome the manufacturing difficulty of SiC. However, obtaining green bodies without damage and maintaining the structural integrity of the printed discs is a challenge. In this work, the following areas are addressed: i) a route for densifying and strengthening the powder bed binder jet-printed SiC through the mixing of particles of different sizes, formation of siloxane bonding, secondary surface modification, and sintering, ii) strengthening and densification of SiC composites using mineral binders using powder metallurgy technique, and iii) realizing the properties of SiC-mineral binder composites for space mirror and thermal applications. Part (ii) of the project was preliminary work done in order to realize the outcomes of SiC-mineral binder composites in strengthening so that it can be adopted into additive manufacturing mentioned in part (i). Future work will involve the inclusion of SiC-mineral binders into the feedstock in a

powder bed binder jet in order to reduce the voids between the interspace of SiC particles and to have a strong interfacial region comprising of mineral binders that can fuse the SiC particles together and densify the printed part. This eliminates the need for the post-processing techniques such as melt infiltration, polymer impregnation, or chemical vapor infiltration.

SiC ceramics are 3D printed into cylindrical discs in a powder bed binder jet using a water binder. In this method, SiC of an average particle size of 40 μm was surface activated with NaOH to form a silica gel layer at room temperature, to which, 30% of 2 μm and 600 nm SiC particles were added and mixed homogeneously through milling. The presence of $OH^-$ ions in silica gel, creates a repulsion between SiC particles which eliminates agglomeration of particles upon spreading. The mixing of coarse and fine particle sizes reduced the percentage porosity by 50%. The as-printed green part was heat treated to 650 °C for 5h to create siloxane bonding which provided an improved handling strength. The heat-treated parts were then impregnated in various concentrations of NaOH to create silica gel through secondary surface activation. SEM images showed that the impregnated samples had more silica nucleation droplets that gave rise to silica nanowires upon sintering at temperatures between 800 °C – 1000 °C. The silica nanowires are responsible for fusing the SiC particles and bridging the pores. The optimum NaOH concentration for secondary surface activation, sintering temperature, and dwell time were determined. Moreover, the formation of nanowires under an oxygen environment proved that silica nanowires can be formed at a temperature as low as 800 °C, and in air, the discs are oxygen deprived which hinders the growth of silica nanowires. Hence the mechanism of the growth of nanowires was found to be similar to the solid-vapor phase deposition.

Cordierite and spodumene are silicate minerals that are known for their excellent thermal properties namely nearly zero thermal expansion coefficient. SiC is a ceramic with excellent

mechanical and thermal properties. SiC, Cordierite, and Spodumene are materials that are considered for space mirrors, mirror substrates, and high-temperature applications. However, the glass ceramic form of Cordierite and Spodumene are less considered for space applications due to their poor stiffness and fracture toughness. On the other hand, SiC is highly considered for such applications however manufacturing them is a challenge considering their high melting point and hardness. Hence, in this work, a combination of SiC and the mineral format of cordierite and spodumene is introduced as SiC-mineral binder composites. SiC-mineral binder composites are 80% SiC and 20% Cordierite or Spodumene minerals prepared through the powder metallurgy technique. SiC-mineral binder composites were found to have good mechanical and thermal properties and can be a promising candidate for space mirror applications. SiC-mineral binders were combined with 1% of NaOH, pressed at 250 MPa, and heat treated to 1200 °C for 8 h. The SEM-EDX analysis showed a strong interfacial region of cordierite or spodumene fusing the SiC particles together. The fracture mechanism was found to be transgranular which is due to the strong interfacial bond that was created by the atomic diffusion of Si and Al at the grain boundary of SiC and the mineral interface. The characterization involves the comparison of SiC-mineral binders to the control SiC-cristobalite without mineral binders. The phase analysis from XRD showed the presence of cordierite, spodumene, and cristobalite phases. A transformation of β-SiC to α-SiC was also observed. A slight shift in the d-spacing, the lattice constants, and crystallite size was observed as a result of a solid solution of phases. The density and porosity of these composites were measured using Archimedes and mercury porosimetry. Further pore size analyses were done using SEM and ImageJ analysis. The results showed that the introduction of mineral binders reduced the pore size and the porosity percentage. The compressive strength of the SiC-Cordierite and SiC-

Spodumene was 282.57 MPa and 184.58 MPa which was much higher than the control SiC-Cris, 97.45 MPa. The average compressive strength of SiC-Cord was three times higher than control SiC-Cris ($p < 9.7 \times 10^{-7}$) and two times higher than that of SiC-Spod ($p < 0.003$). Moreover, the average compressive strength of the SiC-Spod was significantly higher than that of the control SiC-Cris ($p < 9.8 \times 10^{-7}$). Elastic modulus was found using the nanoindentation technique and was 380.54 GPa and 341.04 GPa for SiC-Cord and SiC-Spod composites. Thermal shock resistance is an important factor for materials to qualify for space applications. SiC-mineral composites showed excellent thermal shock resistance and dimensional stability when quenched from 1200 °C to room temperature. A thermal expansion coefficient of $3 \times 10^{-6}$ /K was obtained for both SiC-Cord and SiC-Spod composites. The SiC-mineral composites were polished to a mirror finish. The surface roughness of areas comprised of SiC particles and the mineral binder without pores measured using atomic force microscopy was 20.89 nm. The mean roughness of the SiC microconstituent in the SiC-Cord composite was found to be $2.37 \pm 0.28$ nm. Owing to these excellent thermos-mechanical properties, SiC-mineral binder composites are promising candidates for space mirror applications, mirror substrates, substrates for high-temperature devices, and catalytic converters. Also, porous SiC-mineral binder composites can be used as gas/fuel filters for automobile industries.

# DEDICATION

This work is dedicated to the memory of my mother, Kanchana, who loved me, supported me, and encouraged me at every tiny step of my life. Without her continual support and love, this would not have been possible. Secondly, my father, Chandrasekaran, who provided me with a good education and supported me immensely in my career. Finally, to my loving husband and daughter, Manikandan Karunan and Iyanya Manikandan for cheering me up throughout my Ph.D. endeavor. Thank you all.

# ACKNOWLEDGEMENTS

I would like to express my deepest gratitude and sincere thanks to my advisor, Dr. Ahmed El-Ghannam, for his significant guidance, and support throughout my Ph.D. journey. Dr. El-Ghannam's immense knowledge of materials science and biomaterials inspired and motivated me to do good research work. Dr. El-Ghannam's patience, freedom to work, and constant motivation helped tremendously to keep up with my passion for research. His guidance during the time of COVID-19 is noteworthy. I would also like to thank Dr. Harish Cherukuri, Dr.Youxing Chen, Dr. Charles Lee and Dr. Didier Dreau for being a part of my advisory committee and for their valuable inputs in the preparation of this dissertation. I would like to thank Dr. Chenying Xu, Dr. Lin Ma, and Dr. James Monroe for helping with the electrical and thermal measurements. I would like to thank Dr. Konstantinos Falaggis and Prithiviraj Shanmugam for helping with the CSI measurements. I would like to thank my labmate, Ms. Farjana Sultana for her assistance in 3D printing. Special thanks to the staff of the Mechanical Engineering department, whose help and support have been indispensable. I would like to thank UNC Charlotte for the financial support offered by the Graduate Assistant Support Plan (GASP) award. I would also like to thank the Department of Defense, for funding the research project (Funding Opportunity Announcement W911NF-17-S-0010). I would like to thank my siblings and in-laws (Smitha, Hari Prasad, Rajitha TR, Shyam Prasad, Karthika Devi) and friends Pavitra, Balaje, Shank, and Pedram for their unending support and encouragement throughout my career. Finally, I would like to thank all my extended family and friends for their support.

TABLE OF CONTENTS

# LIST OF FIGURES

# LIST OF TABLES

# CHAPTER 1: INTRODUCTION

## 1.1. Background and Motivation

Dense and porous Silicon Carbide (SiC) ceramics and composites are used in a wide range of applications that require high thermal, mechanical, and electrical stability, excellent corrosion, and wear resistance [1-8]. However, manufacturing SiC through conventional powder metallurgy technique techniques is often challenging. Due to the covalent bonding between Si and C, they have a high melting point. Hence high temperatures, pressures, and controlled atmospheres are required during sintering to manufacture SiC ceramic with good mechanical and thermal strength [9]. Other techniques to manufacture SiC at relatively low temperatures involve thermal oxidation [10-13], pressureless sintering [14-18], and the addition of sintering additives [18-21]. Some applications like biological scaffolds, ballistic armor, space mirror substrates, and ceramic filters involve complex geometries [22, 23]. Manufacturing of complex geometries through the conventional route involves machining or molding. Machining SiC is a challenge due to its extreme hardness and abrasiveness. Molding a pre-form utilizes polymer resin which can cause shrinkage to the final product. upon debinding and sintering. Hence, the additive manufacturing route is considered feasible for the manufacturing of SiC ceramics or composites [24-28]. Additive manufacturing (AM) enables 3D printing of complex geometries from a CAD model. Multiple direct AM methods were realized for the printing of SiC such as selective laser sintering (SLS), selective laser melting (SLM), stereolithography (SL), direct ink writing (DIW), and binder jetting (BJ). Among these techniques, the binder jetting technique was found to be easier to manufacture complex geometries of SiC as it does not require, i) polymer additives that cause shrinkage of the part upon sintering and it doesn’t require, ii) high laser power to melt SiC,

and iii) ceramic slurry, where the amount of ceramic used is less. Binder jetting also allows the mixing of different ceramic particles and additives that can help in the densification and strengthening of the printed part [29].

## 1.2. Silicon Carbide and conventional manufacturing

Silicon Carbide (SiC) is a compound of Silicon and Carbon that are covalently bonded to each other which makes it stronger and thermally stable as its melting point is around 2730 °C. SiC is industrially manufactured for many applications included the production of ceramics with outstanding mechanical properties. The above-mentioned properties of SiC make them a reasonable alternative to pure metals for space mirror applications [30,31]. Similar deflection amplitude was achieved with only fewer support points in SiC mirrors than glass ceramic mirrors as SiC is much stronger than glass materials. SiC mirror manufacturing is a multiple step process that includes: Molding, Machining and Cladding. In molding, the carbon fibers are impregnated in phenolic resin to near-net geometry. The green body is then milled and machined to obtain desired shape. To this, molten liquid silicon is infiltrated to form C/SiC mirror blank. Cladding is a coating phase where SiC layer is coated either through reaction bonding, chemical vapor deposition, or chemical vapor infiltration techniques. Following cladding, these substrates are grounded finely and polished to obtain mirror like surface. Hot pressing, high temperature sintering and foaming are other manufacturing techniques adopted to manufacture SiC mirrors [31-35]. However, these techniques involves a lot of manufacturing difficulties such as: i) drying of the large scale blanks lead to shrinkage (>10%) and introduction of cracks, ii) sintering requires high temperature >1600 °C so that large furnaces and controlled atmospheres are required, iv) risk of material failure during milling in the light-weighting process, iii)

temperature un-uniformity occurs during sintering due to the large size of the mirrors, iv) polishing difficulties in SiC can only be polished with diamond powder and requires a different technique than the traditional glass polishing [34,35]. Due to these manufacturing difficulties, composites such as Metal-Matrix composite (AlBeMet), SiC/Al, Si/SiC, hybrid carbon fiber-reinforced SiC (HB-Cesic) composites are preferred than pure metals and ceramics [36-38]. Light-weighting is a crucial step in mirror design as it involves milling and machining the mirror material to complex geometries. The three predominant mirror designs are arched mirrors, open-back mirrors and sandwich mirrors. Machining of these complex geometries to high precision greatly increases the manufacturing cost. Hence, additive manufacturing (AM) is recently considered in the development of mirror systems as it requires less material consumption, less manpower which reduces the manufacturing cost [39-45].

### 1.3. Binder Jetting of ceramic powders: Pros and Cons

In the binder jetting technique, the ceramic powders are spread layer by layer and every layer and particle are bonded together through a liquid binder [29,46]. Binder jetting technique doesn't require any support part unlike other printing techniques, the requirement of sacrificial material is minimal and it is highly scalable. However, the major disadvantage of this technique is that the printed part is usually highly porous [47]. To overcome the porosity of the printed part, post-processing such as sintering, chemical reaction, infiltration and isostatic pressing are carried out. Each technique has its own advantage and disadvantages. Sintering is usually done at high temperatures and the elimination of solid/vapor interfaces during sintering removes voids and the space between particles [48]. Sintering density greatly depends on the green density of the printed part. If the printed part has poor density, sintering would not improve the density any

further [49]. The green density of the printed part depends on the particle size of the powder feedstock. Fine (0.5 μm) and coarse particle sizes (10 μm) of alumina were tested to understand the effect of particle size on the density of the green part and the sintered part. It was observed that the green parts that were printed from fine and coarse particles showed same green density, however, upon sintering the parts printed with fine particles showed a density of ~99% compared to the ~58% obtained from the part printed from coarse particles [50,51]. However, the parts printed with coarse particles showed minimum volume shrinkage upon sintering, comparatively. The other technique of densification involves mixing of a metal additive [52-55] to the feedstock such that the molten additive can fill the interspace, immersing the printed parts in phosphoric acid to obtain calcium phosphate and phosphate bonds [56], immersion of silicone increased the density up to 87.01 % in the printed upon sintering at 1200 ºC for 1 h. This immersion technique cannot be performed on the larger parts as it involves mass transport of the reagents [57]. Hence, an infiltration technique is carried out, where a molten metal [58,59] is poured into the porous printed part. Infiltration of metals can lead to formation of weak secondary phases that can have a negative effect on the strength of the composite. Other infiltration techniques are solution infiltration and precursor infiltration where fine powder of the same printed material are mixed with a solvent (for solution) and with an aqueous solution of the material which undergoes hydrothermal reaction upon heat treatment. Disadvantage in both techniques are the amount of solution infiltrating would be non-homogenous. Maleksaeedi et.al., found that the depth of infiltration decreased when the amount of solid loading was increased [60]. Cold isostatic (CIP) or hot isostatic (HIP) techniques were used to apply equal pressure on the printed with water, oil or gas as a medium [61-64]. Isostatic pressing can significantly increase the strength of the printed part however this technique is not suitable for complex geometries. Moreover, even with

the printing modifications and post-treatments, there is not enough studies on spreading behavior of fine powders. Challenges in spreading with fine particles are identified as interparticle cohesion (i.e., van der Waals or electrostatic attraction). Hydrogen bonding and capillary bridging can also play a huge role in spreading and densification of fine particles that are unfortunately not addressed in many researches [47].

### 1.4. SiC for optical mirrors

Optical mirrors are used in space telescopes and satellites for various astronomical and earth science observations. Space mirrors are used to power satellites by deflecting sun's energy and energy from the moon is beamed to earth by microwave or laser for energy restoration. Space mirrors are further used for illuminating earth for urban lighting, nighttime agricultural work, agricultural enhancements such as weather stabilization, precipitation management, bio-enrichment, crop drying and desalination [65].

### 1.5. Material criteria for space mirrors

Space mirrors undergo different kinds of material degradation factors such as thermal stress, radiation and charging, space debris and oxidation due to atomic oxygen. These factors can negatively impact the thermo-mechanical behavior of the mirrors leading to failure. Therefore, failure to choose the right material for space mirrors can even lead to the early failure of the satellites and the mission [66]. Considering the material degradation, the materials for space mirrors are required to have: low density, high specific stiffness, high thermal conductivity, and low coefficient of thermal expansion (CTE) [67]. Conventionally, Beryllium (Beryllium O30), Aluminum (Aluminum 6061) and Titanium metals are used as space mirrors due to their

lightweight, excellent strength, polishing capabilities and low machinability [68]. However, these metals release toxic gases during processing and are found to have poor thermal stability. On the other hand, glass ceramics and fused silica are preferred such as they have low thermal expansion and good thermal stability. Ultra-low expansion glass (e.g., ULE®) or extremely low expansion glass ceramic (e.g., ZERODUR® or CLEARCERAM®), or ultra-low thermal expansion ceramic NEXCERA™ are currently used mirror materials that are glass ceramics and fused silica [68-71]. The major disadvantage of glass ceramics are low mechanical strength and high charging. Glass ceramics are mostly dielectrics and are prone to charging due to space radiation. The charge build up can cause optical discharge that can lead to loss of transmittance. Hence, a conductive layer of indium-tin-oxide is coated to eliminate the mirrors from charging [72]. Apart from glass ceramics, Silicon Carbide ceramics (Boostec® SiC) are used as mirror materials. as they possess excellent properties such as high strength and elastic modulus, high hardness, low thermal expansion, corrosion resistance, and low density.

### 1.6. Additive manufacturing of lightweight mirrors

Mirror components are also 3D printed and they can also be used for stress polishing for the creation of free-form super-smooth optics [73]. Also, lightweight structures that has honeycomb structures, topology optimized structures and periodical structures can also be additively manufactured as they have complex geometries [74-78].

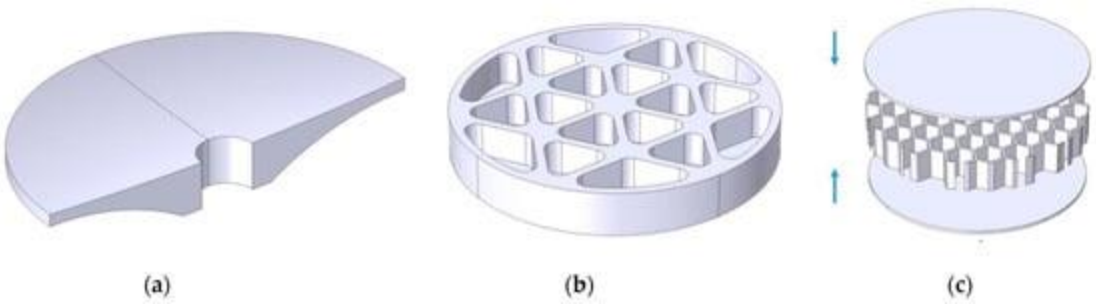


FIGURE 1.1. (a) arched mirror; (b) open-back mirror; (c) sandwich mirror [43]

Metal powders such Aluminum, beryllium and titanium are easily printed through stereolithography (SLA or DLP), direct ink writing (DIW), fused deposition modeling (FDM), selective laser sintering (SLS), selective laser melting (SLM) and laser powder bed fusion (LPBF). However, metals are still less considered for mirror applications as they are thermally unstable and not resistant to atomic oxygen. Hence SiC ceramics and composites are 3D printed mostly using SLA, DLP and binder jetting (BJ) techniques. Printing that requires laser and high power such as SLS, SLM, FDM cannot be used for SiC as they have a high melting point of 2730 ºC and requires high power for laser to melt SiC. FDM, DIW, and Stereolithography techniques use polymer or resin medium to enable the printing of complex geometry. However, the amount of ceramic used in these techniques is small and the sintering process is non-homogenous [29]. Hence, additive manufacturing through binder jetting technique is found suitable for printing SiC ceramics and composites, as it doesn't require wires, fibers, or slurries like other techniques. Binder jetting also allows colors to be applied to the parts and a mixture of ceramic powders (different ceramics and particle sizes) can be used. This eliminates many post-processing steps and reduces manufacturing costs [46].

## 1.7. Problem Statement

This dissertation focused on additive manufacturing of SiC using powder bed binder jetting technique without the use of polymer or chemical binders. Also, to realize a SiC composite with excellent thermo-mechanical properties that can be additively manufactured for space mirror applications without the need of controlled atmospheres, high pressures, and temperatures. To obtain this end, we developed two methodologies:

**Aim 1: Develop a post-processing protocol for the powder bed binder jet printed SiC.**

To successfully 3D print SiC through powder bed binder jet using water binder, we adopted 3 routes: i) to surface activate the coarse particle size (~40 µm) to form the silica gel layer (Si-OH) and mixed with finer particle sizes such as 2 µm and 600 nm such that the finer particle sizes would mechanically fill the pores at the interspace between the particles and layers. Also, the $OH^-$ ions helps preventing agglomeration of particles as it creates a zeta potential that repels the particles from contact ensuring even spreading of the powders, ii) the printed SiC parts were heat treated at 650 °C to create siloxane bonding that enables good handling strength to the parts such that the excess from the parts can be cleaned without affecting the structural integrity, iii) surface activate the part by impregnating it in NaOH to create more silica gel, this technique was named as secondary surface activation. These post-processing steps enabled formation of Si-O nucleation droplets which formed silica nanowires upon sintering at 1000 °C that bridge the pores and interspace enabling strength to the printed part.

**Aim 2: Develop a SiC composite with mineral binders to obtain maximum strength and densification.**

To enhance the density and strength of the SiC composites, we synthesized cordierite (magnesium aluminum silicate) and spodumene (lithium aluminum silicate) mineral binders from scratch. Cordierite and spodumene are rock-forming minerals characterized by low thermal expansion coefficient, thermal shock resistance, and good mechanical and thermal stability and are used as mirror materials. The ability of Cordierite and spodumene to serve as binders for surface active SiC was studied. From aim 1, it was understood that the silica gel layer can promote reaction with mineral binders to establish in situ mineralization at the interface between SiC particles. We mixed particles of cordierite and spodumene to surface activated SiC to form SiC-Cordierite and SiC-Spodumene composites. The silica gel promoted an atomic diffusion of Si and Al at the interface of SiC and the mineral binder which created a strong interface between SiC particles. Upon sintering, the liquid phase of the mineral binder, filled the pores mechanically reducing the porosity percentage and the pore size. Hence, the composite was densified and thereby it imparted strength to the composite. The thermo-mechanical properties of these SiC-mineral binder composites were studied in detail to realize its use as space mirror. This composite is developed in such a way that, this mechanism can be extended to additive manufacturing by adding cordierite or spodumene as non-sacrificial ceramic additives.

## 1.8. Dissertation Structure and Outcomes

The densification and strengthening mechanisms developed in this dissertation combines two manufacturing techniques of ceramics or composite preparation: i) additive manufacturing and ii) powder metallurgy. Adoption of two techniques for the same end goal suggests the versatility of

the developed processes. Chapter 2 (Paper 1) presents the studies on the development of the post-processing technique for printing SiC in powder bed and optimization of parameters such as concentration of NaOH for secondary surface activation, sintering temperature, and dwell time. The importance of oxygen environment in the growth of silica nanowires at low temperature (800 °C) was studied. The post processed 3D printed discs were characterized for density, compressive strength, the formation of Si-O and $SiO_2$ as a result of post-processing were analyzed by Fourier transform infrared spectroscopy (FTIR), scanning electron microscopy (SEM), and elemental analysis (EDX). Chapter 3 (Paper 2) presents the studies on densification of SiC using mineral binders such as cordierite and spodumene. The ability of Cordierite and spodumene to serve as binders for surface active SiC was studied. The mechanism of the failure, interface and the strength were studied. Finally, Chapter 4 (Paper 3) presents studies to realize the mechanical and thermal properties of the SiC-mineral binder composites measured as a function of processing parameters and polishing ability of the composites was established to serve as a future space mirror material and for high temperature applications. In addition to the three mentioned journal papers, three other papers are published in this Ph.D. research which are:

1. Chandrasekaran, S., El-Ghannam, A., Monroe, J. A., & Xu, C. (2022, October). Thermo-Mechanical Properties of SiC-Mineral Binder Composites for Space Applications. In *ASME International Mechanical Engineering Congress and Exposition* (Vol. 86656, p. V003T04A004). American Society of Mechanical Engineers.
2. El-Ghannam, A., Chandrasekaran, S., & Sultana, F. (2021). Synthesis and characterization of a novel silica nanowire reinforced SiC thermal material. *Journal of Solid-State Chemistry*, *297*, 122055.

3. El-Ghannam, A., Chandrasekaran, S., & Sultana, F. (2021). Mechanism of epitaxial growth of silica nanowires reinforcing agent in porous SiC scaffold. *Procedia Manufacturing*, *53*, 535-560.

The hypothesis of chapter 2 and 3 of the thesis was to expand the mineral binder composite into 3D printing using powder bed binder jetting technique. However, due to the constraint of printing small quantities in projet460Plus is difficult, we were unable to print this composite. To realize the versatility of this composite, 3D printing of SiC-mineral binder composite was tried in a Bison1000 Digital light printing (DLP) with different loading ratios (in Appendix). The depth curing tests were successful however, the printing was not. More experiments need to be conducted to successfully print this composite in DLP.

# REFERENCES


1. Lawn, B. R., Padture, N. P., Cait, H., & Guiberteau, F. (1994). Making ceramics" ductile". *Science*, *263*(5150), 1114-1116.

2. Balog, M., Šajgalík, P., Hnatko, M., Lenčéš, Z., Monteverde, F., Kečkéš, J., & Huang, J. L. (2005). Nano-versus macro-hardness of liquid phase sintered SiC. *Journal of the European Ceramic Society*, *25*(4), 529-534.

3. Rodríguez-Rojas, F., Ortiz, A. L., Guiberteau, F., & Nygren, M. (2011). Anomalous oxidation behaviour of pressureless liquid-phase-sintered SiC. *Journal of the European Ceramic Society*, *31*(13), 2393-2400.

4. Herrmann, M., Sempf, K., Schneider, M., Sydow, U., Kremmer, K., & Michaelis, A. (2014). Electrochemical corrosion of silicon carbide ceramics in H2SO4. *Journal of the European Ceramic Society*, *34*(2), 229-235.

5. Kaur, S., Riedel, R., & Ionescu, E. (2014). Pressureless fabrication of dense monolithic SiC ceramics from a polycarbosilane. *Journal of the European Ceramic Society*, *34*(15), 3571-3578.

6. Kim, Y. W., Lim, K. Y., & Seo, W. S. (2014). Microstructure and thermal conductivity of silicon carbide with yttria and scandia. *Journal of the American Ceramic Society*, *97*(3), 923-928.

7. Terrani, K. A., Kiggans, J. O., Silva, C. M., Shih, C., Katoh, Y., & Snead, L. L. (2015). Progress on matrix SiC processing and properties for fully ceramic microencapsulated fuel form. *Journal of Nuclear Materials*, *457*, 9-17.

8. Kim, Y. W., Jang, S. H., Nishimura, T., Choi, S. Y., & Kim, S. D. (2017). Microstructure and high-temperature strength of silicon carbide with 2000 ppm yttria. *Journal of the European Ceramic Society*, *37*(15), 4449-4455.

9. Oguntuyi, S. D., Shongwe, M. B., Tshabalala, L., Johnson, O. T., & Malatji, N. (2023). Effects of SiC on the microstructure, densification, hardness and wear performance of TiB2 ceramic matrix composite consolidated via spark plasma sintering. *Arabian Journal for Science and Engineering*, *48*(3), 2889-2903.

10. Benfdila, A., & Zekentes, K. (2010). On silicon carbide thermal oxidation. *The African Review of Physics*, *4*.

11. Roy, J., Chandra, S., Das, S., & Maitra, S. (2014). Oxidation behaviour of silicon carbide-a review. *Rev. Adv. Mater. Sci*, *38*(1), 29-39.

12. Zhao, C., Tu, Z., & Mao, J. (2023). Thermal-oxidation coupled analysis method for unidirectional fiber-reinforced C/SiC composites in air oxidizing environments below 1000° C. *International Communications in Heat and Mass Transfer*, *143*, 106678.

13. Dey, A., Kayal, N., Molla, A. R., & Chakrabarti, O. (2014). Investigation of thermal oxidation of Al2O3-coated SiC powder. *Thermochimica Acta*, *583*, 25-31.

14. Omori, M., & Takei, H. (1982). Pressureless sintering of SiC. *Journal of the American Ceramic Society*, *65*(6), c92-c92.

15. Gomez, E., Echeberria, J., Iturriza, I., & Castro, F. (2004). Liquid phase sintering of SiC with additions of Y2O3, Al2O3 and SiO2. *Journal of the European Ceramic Society*, *24*(9), 2895-2903.

16. Zhu, M., & Wang, Y. (2009). Pressureless sintering ZrB2–SiC ceramics at low temperatures. *Materials Letters*, *63*(23), 2035-2037.

17. Gustafsson, S., Falk, L. K., Lidén, E., & Carlström, E. (2008). Pressureless sintered Al2O3–SiC nanocomposites. *Ceramics International*, *34*(7), 1609-1615.

18. Liang, H., Yao, X., Zhang, J., Liu, X., & Huang, Z. (2014). Low temperature pressureless sintering of α-SiC with Al2O3 and CeO2 as additives. *Journal of the European Ceramic Society*, *34*(3), 831-835.

19. Raju, K., & Yoon, D. H. (2016). Sintering additives for SiC based on the reactivity: a review. *Ceramics International*, *42*(16), 17947-17962.

20. She, J. H., & Ueno, K. (1999). Effect of additive content on liquid-phase sintering on silicon carbide ceramics. *Materials Research Bulletin*, *34*(10-11), 1629-1636.

21. Noviyanto, A., & Yoon, D. H. (2013). Metal oxide additives for the sintering of silicon carbide: reactivity and densification. *Current Applied Physics*, *13*(1), 287-292.

22. Saadi, M. A. S. R., Maguire, A., Pottackal, N. T., Thakur, M. S. H., Ikram, M. M., Hart, A. J., ... & Rahman, M. M. (2022). Direct ink writing: a 3D printing technology for diverse materials. *Advanced Materials*, *34*(28), 2108855.

23. Xu, M., Girish, Y. R., Rakesh, K. P., Wu, P., Manukumar, H. M., Byrappa, S. M., & Byrappa, K. (2021). Recent advances and challenges in silicon carbide (SiC) ceramic nanoarchitectures and their applications. *Materials Today Communications*, *28*, 102533.

24. Dadkhah, M., Mosallanejad, M. H., Iuliano, L., & Saboori, A. (2021). A comprehensive overview on the latest progress in the additive manufacturing of metal matrix composites: potential, challenges, and feasible solutions. *Acta Metallurgica Sinica (English Letters)*, *34*, 1173-1200.

25. Travitzky, N., Bonet, A., Dermeik, B., Fey, T., Filbert-Demut, I., Schlier, L., ... & Greil, P. (2014). Additive manufacturing of ceramic-based materials. *Advanced engineering materials*, *16*(6), 729-754.

26. Sun, J., Ye, D., Zou, J., Chen, X., Wang, Y., Yuan, J., ... & Bai, J. (2022). A review on additive manufacturing of ceramic matrix composites. *Journal of Materials Science & Technology*.

27. Lakhdar, Y., Tuck, C., Binner, J., Terry, A., & Goodridge, R. (2021). Additive manufacturing of advanced ceramic materials. *Progress in Materials Science*, *116*, 100736.

28. Katz-Demyanetz, A., Popov, V. V., Kovalevsky, A., Safranchik, D., & Koptyug, A. (2019). Powder-bed additive manufacturing for aerospace application: Techniques, metallic and metal/ceramic composite materials and trends. *Manufacturing review*, *6*, 5.

29. He, R., Zhou, N., Zhang, K., Zhang, X., Zhang, L., Wang, W., & Fang, D. (2021). Progress and challenges towards additive manufacturing of SiC ceramic. *Journal of Advanced Ceramics*, *10*, 637-674.

30. Logut, D., Breysse, J., Toulemont, Y., & Bougoin, M. (2005, October). Light weight monolithic silicon carbide telescope for space application. In Optical Design and Engineering II (Vol. 5962, pp. 521-532). SPIE.

31. Anapol, M. I., & Glasheen, R. R. (1994, September). Silicon carbide lightweight telescopes for advanced space applications. In Space Optics 1994: Space Instrumentation and Spacecraft Optics (Vol. 2210, pp. 373-382). SPIE.

32. Zhou, H., Zhang, C. R., Cao, Y. B., & Zhou, X. G. (2006, May). Lightweight C/SiC mirrors for space application. In 2nd International Symposium on Advanced Optical Manufacturing and Testing Technologies: Large Mirrors and Telescopes (Vol. 6148, pp. 169-174). SPIE.

33. Breysse, J., Castel, D., Laviron, B., Logut, D., & Bougoin, M. (2019, August). All-SiC telescope technology: recent progress and achievements. In International Conference on Space Optics—ICSO 2004 (Vol. 10568, pp. 808-821). SPIE.

34. Yui, Y. Y., Kimura, T., & Tange, Y. (2017, November). Development of reaction-sintered SiC mirror for space-borne optics. In International Conference on Space Optics—ICSO 2004 (Vol. 10568, pp. 357-364). SPIE.

35. Zhang, Y., Zhang, J., Han, J., He, X., & Yao, W. (2004). Large-scale fabrication of lightweight Si/SiC ceramic composite optical mirror. Materials Letters, 58(7-8), 1204-1208.

36. Zhang, X., Hu, H., Wang, X., Luo, X., Zhang, G., Zhao, W., ... & Zhang, F. (2022). Challenges and strategies in high-accuracy manufacturing of the world's largest SiC aspheric mirror. Light: Science & Applications, 11(1), 310.

37. Yan, C., Lifeng, W., & Jianyue, R. (2008). Multi-functional SiC/Al composites for aerospace applications. Chinese Journal of Aeronautics, 21(6), 578-584.

38. Krödel, M. R., & Ozaki, T. (2007, September). HB-Cesic composite for space optics and structures. In Optical Materials and Structures Technologies III (Vol. 6666, pp. 115-124). SPIE.

39. Zhang, K., Qu, H., Guan, H., Zhang, J., Zhang, X., Xie, X., ... & Wang, C. (2021). Design and fabrication technology of metal mirrors based on additive manufacturing: A review. Applied Sciences, 11(22), 10630.

40. Ahmad, A. (Ed.). (2017). Handbook of optomechanical engineering. CRC Press.

41. Woodard, K. S., & Myrick, B. H. (2017, May). Progress on high-performance rapid prototype aluminum mirrors. In Advanced Optics for Defense Applications: UV through LWIR II (Vol. 10181, pp. 177-182). SPIE.

42. Atkins, C., Feldman, C., Brooks, D., Watson, S., Cochrane, W., Roulet, M., ... & Perrin, F. (2018, July). Topological design of lightweight additively manufactured mirrors for space. In Advances in Optical and Mechanical Technologies for Telescopes and Instrumentation III (Vol. 10706, pp. 123-139). SPIE.

43. Atkins, C.; van de Vorst, B. OPTICON A2IM Cookbook: An introduction to additive manufacture for astronomy (Final). Zenodo 2021, 3, 18.

44. Sweeney, M., Acreman, M., Vettese, T., Myatt, R., & Thompson, M. (2015, September). Application and testing of additive manufacturing for mirrors and precision structures. In Material technologies and applications to optics, structures, components, and sub-systems II (Vol. 9574, pp. 47-59). SPIE.

45. Wang, Y., Wu, X., Xu, L., Ding, J., Ma, Z., & Xie, Y. (2018). Fabrication of a lightweight Al alloy mirror through 3D printing and replication methods. Applied Optics, 57(27), 8096-8101.

46. Lv, X., Ye, F., Cheng, L., Fan, S., & Liu, Y. (2019). Binder jetting of ceramics: Powders, binders, printing parameters, equipment, and post-treatment. Ceramics International, 45(10), 12609-12624.

47. Du, W., Ren, X., Pei, Z., & Ma, C. (2020). Ceramic binder jetting additive manufacturing: a literature review on density. Journal of Manufacturing Science and Engineering, 142(4), 040801.

48. Barsoum, M. (2019). Fundamentals of ceramics. CRC press.

49. Kang, S. J. L. (2004). Sintering: densification, grain growth and microstructure. Elsevier.

50. Du, W., Ren, X., Chen, Y., Ma, C., Radovic, M., & Pei, Z. (2018, June). Model guided mixing of ceramic powders with graded particle sizes in binder jetting additive manufacturing. In International Manufacturing Science and Engineering Conference (Vol. 51357, p. V001T01A014). American Society of Mechanical Engineers.

51. Zocca, A., Lima, P., & Günster, J. (2017). LSD-based 3D printing of alumina ceramics. Journal of ceramic science and technology, 8(1), 141-148.

52. Yao, D., Gomes, C. M., Zeng, Y. P., Jiang, D., Günster, J., & Heinrich, J. G. (2015). Near zero shrinkage porous Al2O3 prepared via 3D-printing and reaction bonding. Materials letters, 147, 116-118.

53. Solis, D. M., Silva, A. V., Volpato, N., & Berti, L. F. (2019). Reaction-bonding of aluminum oxide processed by binder jetting. Journal of Manufacturing Processes, 41, 267-272.

54. Rabinskiy, L., Ripetsky, A., Sitnikov, S., Solyaev, Y., & Kahramanov, R. (2016, July). Fabrication of porous silicon nitride ceramics using binder jetting technology. In IOP Conference Series: Materials Science and Engineering (Vol. 140, No. 1, p. 012023). IOP Publishing.

55. Myers, K., Juhasz, M., Cortes, P., & Conner, B. (2015). Mechanical modeling based on numerical homogenization of an Al2O3/Al composite manufactured via binder jet printing. Computational Materials Science, 108, 128-135.

56. Zocca, A., Elsayed, H., Bernardo, E., Gomes, C. M., Lopez-Heredia, M. A., Knabe, C., ... & Günster, J. (2015). 3D-printed silicate porous bioceramics using a non-sacrificial preceramic polymer binder. Biofabrication, 7(2), 025008.

57. Zocca, A., Gomes, C. M., Staude, A., Bernardo, E., Günster, J., & Colombo, P. (2013). SiOC ceramics with ordered porosity by 3D-printing of a preceramic polymer. Journal of Materials Research, 28(17), 2243-2252

58. Moon, J., Caballero, A. C., Hozer, L., Chiang, Y. M., & Cima, M. J. (2001). Fabrication of functionally graded reaction infiltrated SiC–Si composite by three-dimensional printing (3DP™) process. Materials Science and Engineering: A, 298(1-2), 110-119.

59. Fu, Z., Schlier, L., Travitzky, N., & Greil, P. (2013). Three-dimensional printing of SiSiC lattice truss structures. Materials Science and Engineering: A, 560, 851-856.

60. Maleksaeedi, S., Eng, H., Wiria, F. E., Ha, T. M. H., & He, Z. (2014). Property enhancement of 3D-printed alumina ceramics using vacuum infiltration. Journal of Materials Processing Technology, 214(7), 1301-1306.

61. Rahaman, M. N. (2003). Special Topics in Sintering. Ceramic Processing and Sintering, Marcel Dekker Inc, New York, ABD, 688-845.

62. Vermeiren, E. (2002). The advantages of all-round pressure. Metal Powder Report, 57(2), 18-21.

63. Koizumi, M., & Nishihara, M. (Eds.). (1991). Isostatic pressing: technology and applications. Springer Science & Business Media.

64. Sun, W., Dcosta, D. J., Lin, F., & El-Raghy, T. (2002). Freeform fabrication of Ti3SiC2 powder-based structures: Part I—Integrated fabrication process. Journal of Materials Processing Technology, 127(3), 343-351.

65. Lior, N. (2013). Mirrors in the sky: Status, sustainability, and some supporting materials experiments. Renewable and Sustainable Energy Reviews, 18, 401-415.

66. Garoli, D., Rodriguez De Marcos, L. V., Larruquert, J. I., Corso, A. J., Proietti Zaccaria, R., & Pelizzo, M. G. (2020). Mirrors for space telescopes: Degradation issues. Applied Sciences, 10(21), 7538.

67. Santi, G., Corso, A. J., & Pelizzo, M. G. (2021). Mirrors for space telescopes: degradation issues. EUV and X-ray Optics, Sources, and Instrumentation, 11776, 9-19.

68. Sandin, C. R., Allen, L. N., Amatucci, E. G., Arenberg, J. W., Carter, R. C., Corsetti, J. A., ... & Steeves, J. B. (2021). Materials evaluation for the origins space telescope. Journal of Astronomical Telescopes, Instruments, and Systems, 7(1), 011011-011011.

69. Luz, P. L., & Rice, T. (1998). Mirror material properties compiled for preliminary design of the next generation space telescope (30 to 294 kelvin) (No. NAS 1.15: 208181).

70. Kamiya, T., & Mizutani, T. (2017, September). Comparison of material properties between ultra low thermal expansion ceramics and conventional low thermal expansion glass. In Material Technologies and Applications to Optics, Structures, Components, and Sub-Systems III (Vol. 10372, pp. 52-62). SPIE.

71. Kamiya, T., Sugawara, J., Mizutani, T., Yasuda, S., & Kitamoto, K. (2017, September). Early study on the application of NEXCERA ultra low thermal expansion ceramic to space telescopes. In International Conference on Space Optics—ICSO 2016 (Vol. 10562, pp. 1338-1346). SPIE.

72. Bouquet, F. L., Helms, R. G., Maag, C. R., & Heggen, P. M. (1987). Recent advances in long-lived mirrors for terrestrial and space applications. Solar energy materials, 16(5), 423-433.

73. Roulet, M., Atkins, C., Hugot, E., Lemared, S., Lombardo, S., & Ferrari, M. (2018, May). 3D printing for astronomical mirrors. In 3D Printed Optics and Additive Photonic Manufacturing (Vol. 10675, p. 1067504). SPIE.

74. Hilpert, E., Hartung, J., Risse, S., Eberhardt, R., & Tünnermann, A. (2018). Precision manufacturing of a lightweight mirror body made by selective laser melting. Precision Engineering, 53, 310-317.

75. Herzog, H., Segal, J., Smith, J., Bates, R., Calis, J., De La Torre, A., ... & Wicker, R. (2015, September). Optical fabrication of lightweighted 3D printed mirrors. In Optomechanical Engineering 2015 (Vol. 9573, pp. 53-67). SPIE.

76. Mici, J., Rothenberg, B., Brisson, E., Wicks, S., & Stubbs, D. M. (2015, September). Optomechanical performance of 3D-printed mirrors with embedded cooling channels and substructures. In Optomechanical Engineering 2015 (Vol. 9573, pp. 30-43). SPIE.

77. Kranz, J., Herzog, D., & Emmelmann, C. (2014). Laser additive manufacturing of lightweight structures in TiAl6V4: a design for manufacturing approach. In ESA Workshop Additive Manuf. Space Appl.

78. Hilpert, E., Hartung, J., von Lukowicz, H., Herffurth, T., & Heidler, N. (2019). Design, additive manufacturing, processing, and characterization of metal mirror made of aluminum silicon alloy for space applications. Optical Engineering, 58(9), 092613-092613.

# CHAPTER 2: (PAPER 1) NOVEL STRENGTHENING AND DENSIFICATION TECHNIQUES OF POWDER BED BINDER JET PRINTED SiC COMPOSITES

Authors

Sujithra Chandrasekaran, Prithiviraj Shanmugam, Konstantinos Falaggis, Ahmed El-Ghannam

## 2.1. Introduction

Advanced ceramics are used recently as a replacement for metals in a wide range of applications, such as automobile industries as (automotive sensors, heatshield, brakes, shock absorbers, and engines), aerospace industries as (seals, thermocouples, gas turbine engine components, and ion propulsion systems), defense industries as (armors and missile domes), electronic industries as (circuit breakers, heat sinks, inductor and resistor cores, sensors, substrates to hold high temperature components), and biomedical engineering as (knee and hip components, orthodontic devices, dental implants, tissue scaffolds, drug delivery devices, medical pumps and valves). The excellent properties such as high mechanical strength and hardness, good thermal and chemical stability, and viable thermal, optical, electrical, and magnetic performance make them such versatile materials [1,2].

Silicon carbide (SiC) ceramic and composites are known for their excellent thermo-mechanical properties such as high strength and stiffness, high thermal conductivity, low thermal expansion, and low density. SiC is versatile in many applications ranging from aerospace [3-6], semiconductors [7,8], power devices [9,10], nuclear reactors [11-13], and biomedical devices [14,15]. However, the strong covalent bond between Si and C possess extreme difficulties in manufacturing complex structures that are required for such applications. The complex

geometries are usually processed through the powder metallurgy technique where the ceramic powders are sintered at high temperatures and pressures and then machined, or they are molded to the desired shape before sintering (slip, tape, and gel castings) [16-18]. In the former technique, machining of SiC is difficult and expensive and would require a tool that is harder than SiC like BN or diamond [18]. The latter technique involves resin that needs debinding and sintering which could largely affect the final geometry of the ceramic due to expansion or shrinkage caused during sintering. Hence, the 3D printing technique is most preferred for the manufacturing of SiC ceramics and composites with complex structures. Also, 3D printing would be cost-effective as it requires less material consumption and manpower.

Research has been made to produce highly dense and complex geometries of 3D printed SiC using various additive manufacturing techniques such as binder jetting, stereolithography (SLA or DLP), direct ink writing (DIW), fused deposition modeling (FDM), selective laser sintering (SLS), selective laser melting (SLM) and laser powder bed fusion (LPBF). Of all these techniques, laser sintering techniques such as SLS, SLM, and LPBF require high laser power as SiC has a melting point of 2730 ºC. FDM, DIW, and Stereolithography techniques use polymer or resin medium to enable the printing of complex geometry. However, the amount of ceramic used in these techniques is small and the sintering process is non-homogenous [19]. Hence, binder jetting is found suitable for printing SiC ceramics and composites, as it doesn't require wires, fibers, or slurries like other techniques. Binder jetting allows colors to be applied to the parts and a mixture of ceramic powders can be used. This eliminates many post-processing steps and reduces manufacturing costs [20]. In the binder jetting technique, the ceramic powders are spread layer by layer and every layer and particle are bonded together through a liquid binder. Even though the printing of SiC is possible through binder jetting, the printed parts are mostly

porous. The porosity of the printed part is attributed to the printing parameters, the particle size of the powders, the shape of the powders, and the binder material. Flowability, wettability, and reactivity are affected by the above-said parameters. To improve the flowability, SiC particles were plasma sprayed to make them spherical however spherical shapes are found to produce porous parts compared to irregular particles. Irregularly shaped particles with coarse particle sizes were also found to increase the wettability of the ceramic. Powder-to-binder reactivity is also important in creating dense parts upon printing. Fine particle size with a large surface area produces better reactivity with the binder [21-25]. Even with careful considerations of particle size, shape, and printing parameters, oftentimes the printed parts from binder jetting are porous and would require a post-densification step like phenolic resin impregnation and pyrolysis, and pressureless, reactive melt infiltration of Silicon. The printed part was impregnated in multiple cycles in phenolic formaldehyde to create carbon residue, debinded, and sintered for each cycle at 190 °C and 850 °C for 30 min each. To this part, Si melt was infiltrated through capillary forces at 1670 °C to form SiC [26,27]. However, polymer resin impregnation pyrolysis can induce shrinkage, and it can form undesirable phases depending on the atmosphere in which the pyrolysis is carried out. On the other hand, molten Si can induce cracks in the printed part due to thermal shock and the formation of weak secondary phases. In some cases, ceramic powders like $Al_2O_3$, $SiO_2$, or Poly Vinyl Alcohol (PVA) are added to the feedstock to increase the packing density by reducing the voids between particles. However, the removal of the additives is difficult, and it affects the amount of base material that needs to be printed [28,29].

In this paper, we report a successful printing of SiC composite through powder bed binder jetting technique by, i) surface activation of the coarse particles (~40 μm) to create a silica gel layer, ii) mixing the coarse particles with finer particles of average sizes 2 μm and 600 nm to fill the voids

between layers and interspace, iii) heat treatment at 650 °C to create siloxane bonding to improve the handling strength of the printed part, iv) secondary surface activation of the printed part to produce more silica nucleation, v) growth of silica nanowires to bridge the pores and fuse the SiC particles by sintering at relatively low temperature in the range of 800 °C – 1000 °C without any external pressure or controlled atmosphere. Studies on optimizing the concentration of silica gel, sintering temperature, and dwell time were carried out. The strength of the composites was improved by 100% for the 3D printed discs that were treated at 650 °C, secondary surface activated in 10% and 20% NaOH and heat treated at 1000 °C. The advantage of this technique is that no polymer or ceramic additives are required such that the debinding and shrinkage can be eliminated. This novel innovation produces SiC composites with crystalline silica nanowires that produce dimensionally stable SiC printed discs which can potentially eliminate the expansion and the crack formation of the composite caused by Si melt infiltration.

## 2.2. Materials and Methods

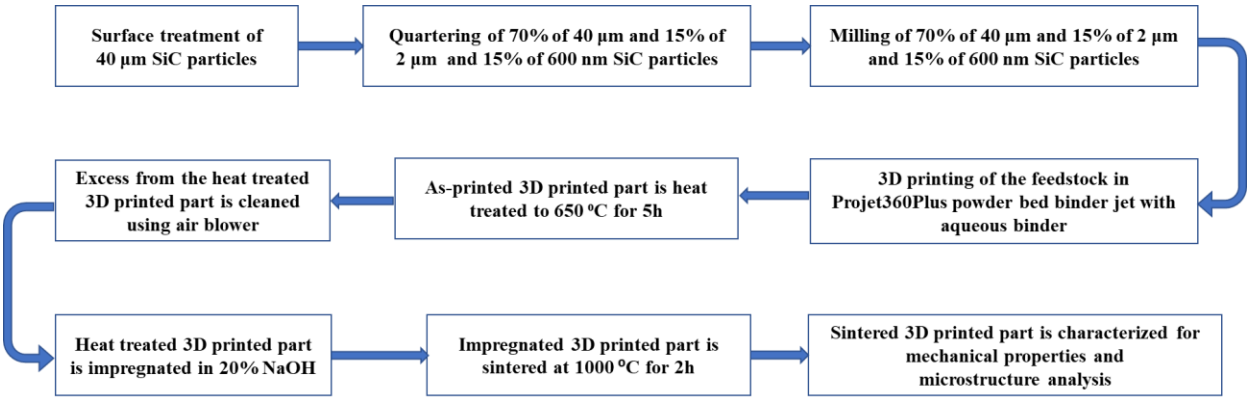


FIGURE 2.1: Steps involving 3D printing of SiC in powder bed and the post-processing for strengthening

2.2.1. Pretreatment of the Silicon Carbide Particles in Sodium Hydroxide

2.2.1.1. Preparation of NaOH solution

Silicon Carbide (US Nano research, Houston, TX, USA) with an average particle size of 40 μm weighed out into 1 kg increments. Dry sodium hydroxide pellets (Sigma Aldrich, St. Louis, MO, USA) were weighed out on a balance to 200 g increments to make a 20% sodium hydroxide mass by volume solution in nano pure water. Each 200 g increment of sodium hydroxide was put into a 500 mL beaker with a stir bar on a magnetic stirrer. 250 mL of nanopure water was added to the beaker and the stir bar was turn on to the low setting (250 rpm). The dissolution of NaOH pellets is an exothermic reaction which makes the container warm. The contents were poured into a 1 L graduated cylinder and nanopure water was added until the solution was exactly 1 L.

2.2.1.2. Immersion treatment of SiC in the NaOH solution:

After the solution had cooled, the SiC powder (~1 Kg) was poured into a plastic 5-gallon bucket in such a way that 75% of gallon was filled and 25% was left empty to enable milling. The 1 L of the 20% sodium hydroxide solution was added to the 5-gallon bucket (contains 1.75 Kg) and a commercial power drill with a paint mixer with 1-3/4" spiral blade, was used to mix until homogenous slurry is formed in approximately 30 mins (each cycle). The ratio of sodium hydroxide to silicon carbide is 1L of 20% sodium hydroxide to 1 kg of silicon carbide powder. The bucket was covered with a lid to prevent any evaporation and left for 24 h.

2.2.1.3. Washing and drying procedures of the SiC particles:

The solution was decanted, where the particles were washed by adding 1 L of nanopure water per kg of silicon carbide and the particles were resuspended using power driven paint mixer for 10 min continuously. Then the solution was left to settle for 24 h. The silicon carbide solution was decanted, and washing was repeated three times until the pH of the SiC suspension lies between 10 and 11. To measure the pH, (6 gm) of the washed (wet) SiC particles was taken and resuspended in 30 ml of fresh nano pure water and the pH was measured with a pH probe (until it stabilizes). 8 oz (236 mL) of 70% isopropyl alcohol per kg of silicon carbide was added to the wet silicon carbide. This was not stirred and left to dry overnight in the chemical fume hood to facilitate removal of the moisture left over in the wet silicon carbide powder.

The semi-dry particles were taken from the 5-gallon bucket and placed in a large plastic tray to dry in the chemical fume hood which helps increase the surface area exposed to air overnight. After drying, the Silicon Carbide forms a crust like layer, which is hard on the surface and loose inside. To disaggregate the particles, the material was transferred to a closed plastic container and milled using 100 g alumina beads of diameter 13 mm for 4 hours in a roller mixer. After the powder is taken out of the mill, it was sifted to remove the alumina beads and then sifted again using a 200 μm sieve. The powder was taken and put in plastic trays and placed in a drying oven heated to 100 °C for 12h. The SiC powder was taken out, allowed to cool to room temperature and re-milled in the roller mixer to break the clumps using the same process above. The powder was then used for 3D printing according to the protocol below.

2.2.2. Nano-Micro SiC mixture preparation

The surface-activated powder prepared in section 2.2.1. was mixed with 15 weight % 2 microns and 15 weight % of 600 nm SiC particles. The submicron particles were added to fill the interspace between the large particles during printing. Quartering is a process to blend the powders of different particle sizes to obtain a homogenous mix and was done in 2 batches. For every batch, 70% of pre-treated SiC 40 μm powder was mixed with 15 weight % 2 microns and 15 weight % of 600 nm SiC particles. The blended SiC powders from the two batches were combined and fed into the plastic jar with 13 mm diameter alumina balls in a roller mixer for 1 h to ensure complete mixing of both batches. The milled powders were then sieved using a mesh with an opening of 425 μm. The sieved mixture of nano-micro particles was fed into the feeder with the help of vacuum suction. The 3DProjet460Plus comes with an auger roller inside the feeder which also enabled a thorough mixing of the powders before printing. After mixing of the coarse and fine particles, the particle size of the SiC particles were measured by randomly spraying the particles onto the double-sided copper tape using a brush. Then, the copper tape with the particles were stuck to the sample holder and 20 SEM images of each sample were captured. Using these SEM images, the particle size was then measured using ImageJ software. The average and the standard deviation of these samples were obtained which measured 16.23 ± 3.00 μm, 19.30 ± 6.84 μm and 13.81 ± 4.64 μm for SiC not surface activated, SiC pre-treated with 20% NaOH and 3D print powder of SiC (40 μm + 2 μm + 600nm). The large standard deviation and the average did not seem convincing. Other techniques such as conventional solvent evaporation method and DLS were tried for particle size measurement. However, they were not successful either as in the former, the fine particle sizes flew out as the solvent (ethanol) reduces the adhesion between the copper tape and the particles and in the later, due to the

absence of the Brownian movement in SiC, the coarse SiC particles settled at the bottom of the quartz vial which made it difficult to obtain any measurement.

2.2.2.1. Measurements of Particle size

After mixing the coarse and fine particles, the particle size of the SiC particles were measured by randomly spraying the particles onto the double-sided copper tape using a brush. Then, the copper tape with the particles were stuck to the sample holder and 20 SEM images of each sample were captured. Using these SEM images, the particle size was then measured using ImageJ software. The average and the standard deviation of these samples were obtained which measured 16.23 ± 3.00 μm, 19.30 ± 6.84 μm and 13.81 ± 4.64 μm for SiC not surface activated, SiC pre-treated with 20% NaOH and 3D print powder of SiC (40 μm + 2 μm + 600nm). The large standard deviation and the average did not seem convincing. Hence, other techniques such as conventional solvent evaporation method and DLS were tried for particle size measurement. However, they were not successful either, as in the former, the fine particles flew out from the copper tape as the solvent (ethanol) reduces the adhesion between the copper tape and the particles, and in the later, due to the absence of the brownian movement in SiC, the coarse SiC particles settled at the bottom of the quartz vial which made it difficult to obtain any measurement. Hence particle size measurements are not reported in this paper.

2.2.3. 3D printing with Pro-jet

The digital image of the disc of diameter 10 mm and a length of 7 mm was designed using Creo Parametric 3D modeling software. The digital image was then converted to a 3D part by converting it to an STL file (Figure 2.2).

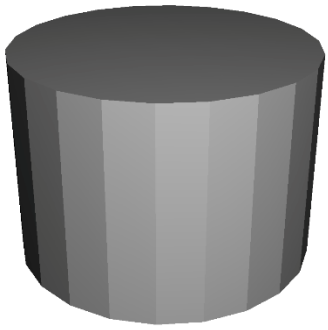

FIGURE 2.2: Isometric view of 3D printed SiC modeled samples using Creo Parametric

The surface activated 40 μm SiC particles prepared according to the protocol described in section 2.2.1 were mixed with 15 weight % SiC particles of an average size 2 μm and 15 weight % SiC of an average particle size 600 nm. The actual weight of these three SiC particle size ranges were 13.6 Kg (40 μm) 2.7 Kg (2 μm) and 2.7 Kg (600 nm) used in this printer. SiC discs of diameter 10 mm and a height of 7 mm were 3D printed using the powder bed binder jetting technique in a Projet460Plus printer from 3D systems. Prior to printing, the service station was vacuumed and cleaned, and the debris collector was cleaned 2-3 times in order to remove any blocks caused by the fine particles. Before every printing, the particles in the feeder were fluidized using an Auger mixer that is available inside the feeder. This ensures that the mixture is homogenously combined before spreading onto the build bed. For every printing, the powder was fetched from the feeder by the carriage rails and spread out evenly by a roller. The build bed was raised to 8” and the build bed was filled with a thick base of SiC particles. The build bed was designed in such a way that it can lower or raise by itself with respect to the dimension of the part specified. After the build chamber was filled, the machine clears out the debris from the

overflow, rear flow, and debris collector. The machine starts printing after this step. The STL file was sent to the printer using the 3DPrint software. About 72 layers were printed for each disc with a layer thickness of 102 μm. For every layer, the aqueous binder (with anaerobic bacteria) by 3D systems was sprayed by the printer to adhere to the layers. After printing, the parts rested inside the build bed for 24 hours.

2.2.3.1. Effect of particle size on porosity 3D printed SiC discs

In order to understand the effect of mixing different particle sizes on the packing of the 3D printed sample, a batch of the 3D printed discs of dimensions 5 mm x 7 mm of pre-treated 40 μm from section 2.2.1 were printed the same way as mentioned in section 2.2.3 but with a Z-Corp printer (3D systems, Rock hill, SC). The printed samples were then heat treated to 900 ºC for 2 h. A batch of samples from section 2.2.3 was also heat treated at 900 ºC for 2h without any further impregnation in NaOH. Scanning electron microscope (SEM) images were compared. To measure the porosity percentage the pre-treated 40 μm powders and nano-micro mixture prepared in section 2.2.1 were hand pressed without any external compact pressure to mimic 3D printed samples. The surface images were captured using SEM and analyzed using ImageJ software.

2.2.3.2 Effect of NaOH treatment on the 3D printed SiC discs

The green parts from powder bed binder jet were heat treated to 650 ºC for 5h at a rate of 10 ºC/min and impregnated in various concentrations of NaOH (1%, 5%, 10% and 20%) for 10 mins and dried on a kim wipe to remove the excess from the outer surface of the printed discs.

These discs were sintered at 800 ºC for 2h (to understand the growth of nanowires), 1000 ºC for 2h (to obtain the maximum density at all concentrations). The width of the bonding zone between SiC particles with respect to different concentrations of NaOH (1%, 10% and 20%) were studied at room temperature and after heat treatment at 650 ºC for 5h (see section 2.4.5).

2.2.3.4 Thermal treatment protocol

The green discs were heat treated to 650 ºC for 5h at a rate of 10 ºC/min to obtain sufficient handling strength. The handling strength is believed to be obtained by the conversion of the silica gel (in the pre-treated SiC 40 μm powder) to amorphous $SiO_2$ at this temperature. The excess particles around the printed part were removed using air pressure. The discs (n=10) were then impregnated (immersed) in (10 mL) 20% NaOH solution for 10 minutes and removed from the solution, excess solution was drained by paper tissue then dried in air. The impregnated parts were then sintered at different temperatures, dwelling times, and environments.

2.2.3.3.1. Effect of temperature

To study the effect of temperature on the 3D printed discs, the discs were sintered at various temperatures 800 ºC/2h, 900 ºC/2h, and 1000 ºC/2h in a Thermolyne™ (Thermo Scientific, Vernon Hills, IL) muffle furnace.

2.2.3.3.2. Effect of oxygen environment

The effect of oxygen in the densification and strengthening of the 3D-printed SiC discs was studied. 3D printed SiC discs were heat treated at 650 ºC for 5h for obtaining structural integrity prior to secondary surface activation in 20% NaOH solution for 10 min. The

impregnated discs were then heat treated again to 650 ºC for 5h to obtain amorphous silica formation. These discs were then sintered at 800 ºC for 2h in a tube furnace under vacuum. During sintering, 50 sccm of $O_2$ was supplied to create an oxygen environment to obtain an efficient conversion of SiO to $SiO_2$ as stated in Eq. (2.1) below.

$$2SiO(g) + O_2(g) \rightarrow 2SiO_2(s) \quad (2.1)$$

2.2.4. Characterization Procedures

2.2.4.1. Morphology analysis SEM-EDS

The growth of nanowires and the porosity characteristics (18 images each) of the thermally treated 3D printed discs, were analyzed by JEOL 6480 Scanning Electron Microscope (SEM, JEOL USA, Waterford, VA), and the elemental composition was determined using Energy Dispersive Spectroscopy (EDS). The sintered discs were sputter coated (Denton vacuum, Moorestown, NJ, USA) with gold (10 nm thickness) and scanned in a secondary electron mode at 20 kV with a working distance of 10 mm. The elemental composition of the nucleation sites and nanowires were analyzed by EDX and presented as atomic percentages.

2.2.4.2. Mechanical test

The compressive strength of the 3D printed discs was calculated from the stress-strain curve obtained by compressing thermally treated discs (n=7) uniaxially using an Instron machine (Instron 5582, Norwood, MA) at a rate of 0.02 in /min until failure.

2.2.4.3. Density

The density of the sintered discs was measured using the Archimedes principle and the mercury porosimetry technique. For the Archimedes method, the dry weight of the sample and the weight of the sample in the auxiliary liquid (deionized water) of all samples were measured at ambient atmospheres. The density was calculated using the Eq. (2.2):

$$\rho = \frac{A}{A-B}(\rho_0 - \rho_L) + \rho_L \quad (2.2)$$

where,

ρ = density of the sample,

A = weight of the sample in air,

B = weight of the sample in the auxiliary liquid,

$\rho_0$ = density of the auxiliary liquid,

$\rho_L$= density of the air (0.0012 g/cm$^3$).

2.2.4.4. Porosity analysis

The width and length of the pores and the nanowires were measured using the SEM software (JEOL instrument software) installed with the JEOL 6480 Scanning Electron Microscope. The porosity percentages were calculated from 17 SEM images of magnifications ranging from x200 – x500 and analyzed using ImageJ software developed by the National Institute of health sciences (LOCI, University of Wisconsin).

2.2.4.5. Effect of NaOH concentration on the thickness of the bonding zone

SiC particles from the 3D print feedstock (prepared in section 2.2.2.) were pre-treated with 1%, 10% and 20% NaOH and hand pressed without any compact pressure to mimic 3D

printing. The width of the silica gel layer of these samples are labeled as room temperature samples. After the width measurements, the samples are then heat treated at 650 ºC for 5h and the width of these samples are labeled at heat treated samples. The width measurements using coherence scanning interferometer are as follows: The widths of the bonding zone comprised of the silica layer between silicon carbide particles were estimated from areal surface measurements taken using Zygo Nexview coherence scanning interferometer (CSI). CSI is an interferometric technique that estimates height maps by evaluating the changes in interference signal strength in relation to its optical coherence while scanning in the vertical direction. The instrument used was a Zygo Nexview with a 50x Mirau objective. Since the surfaces of silicon carbide were too rough, the measurements were made with CSI rough and oversampling settings. The CSI rough setting narrows the bandwidth of the light used, thus increasing the coherence length, to improve the quality of the data when measuring rough surfaces but at the cost of vertical resolution. Oversampling increases the measurement time enabling the instrument to capture weak signals which further increases the quality of the measured surface by reducing data dropouts. Surface measurements were acquired at different areas of the part surfaces. By comparing the height map with the intensity map, locations of silica gel were identified in each surface measurement. The width of silica gel was measured using 1D profile traces between the silicon carbide particles. 20 profiles were randomly chosen, and the mean and standard deviations were evaluated to characterize the width of silica gel layers between silicon carbide particles.

### 2.2.5. Statistical Analysis

All mechanical tests and density measurements were completed using n=7 and the results are presented as mean +/- the standard deviation. One-way analysis of variance (ANOVA) was done

followed by student t-test for multiple comparisons and $P < 0.05$ was considered statistically significant.

## 2.3. Results

### 2.3.1. Effect of particle size on the porosity of 3D printed SiC discs

Figure 2.3 is a digital micrograph of the discs printed using the nano-micro SiC mixture in ProJet460Plus. Figures 2.4 (a and b) show the SEM surface morphology of the fractured surface of 3D printed discs using pre-treated 40 μm SiC particles (Figure 2.4a) and a combination of pre-treated 40 μm particles along with the 600 nm and 2 μm particle sizes of SiC (Figure 2.4b). The discs from this nano-micro SiC mixture showed better structural integrity, smooth surface and less porosity due to the filling of the interspace between coarse particles be the fine SiC particles during printing. A batch of discs was hand pressed at minimal pressure to replicate the 3D-printed discs. Image J analysis of the SEM Figures 2.5a and 2.5b show that the inclusion of fine particles with the 40 μm SiC particles reduced the porosity from $10.54 \pm 1.66$ % to $5.91 \pm 1.29$ %.

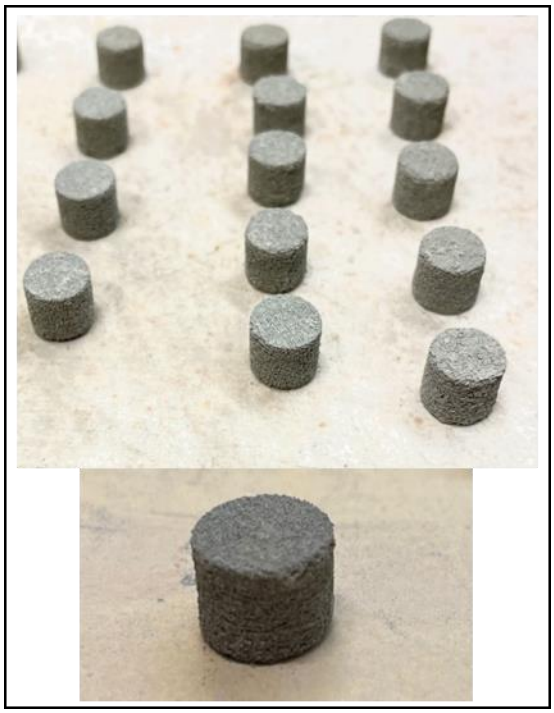

FIGURE 2.3: Digital images of 3D printed discs with the nano-micro combination of particles printed in Projet460Plus. The inset shows the magnified image of the printed samples

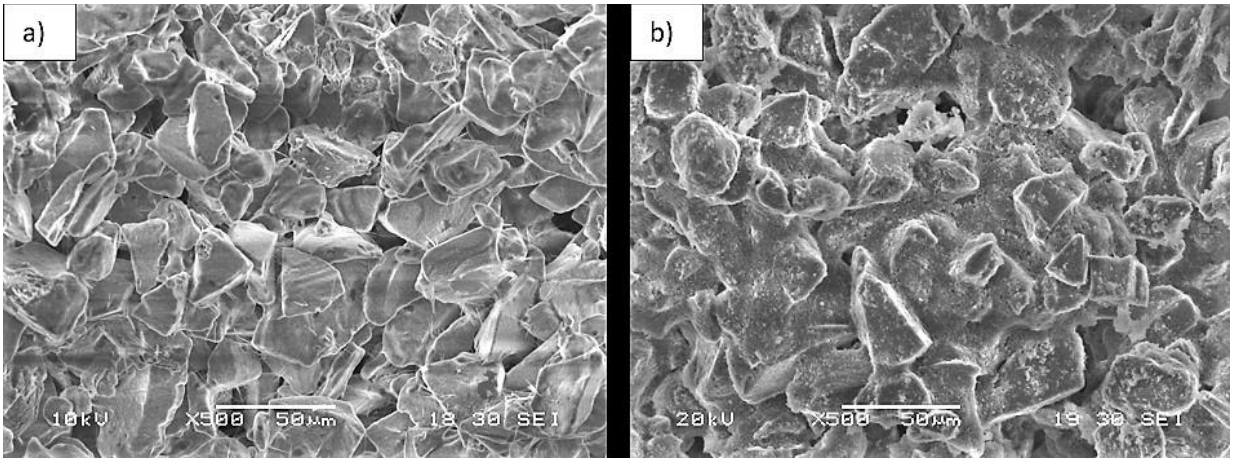


FIGURE 2.4: SEM image of thermally treated 3D printed disc containing a) only surface activated 40 µm SiC particles b) 70% of surface activated 40 µm SiC particles with 15% of 2 µm and 15% of 600 nm particles

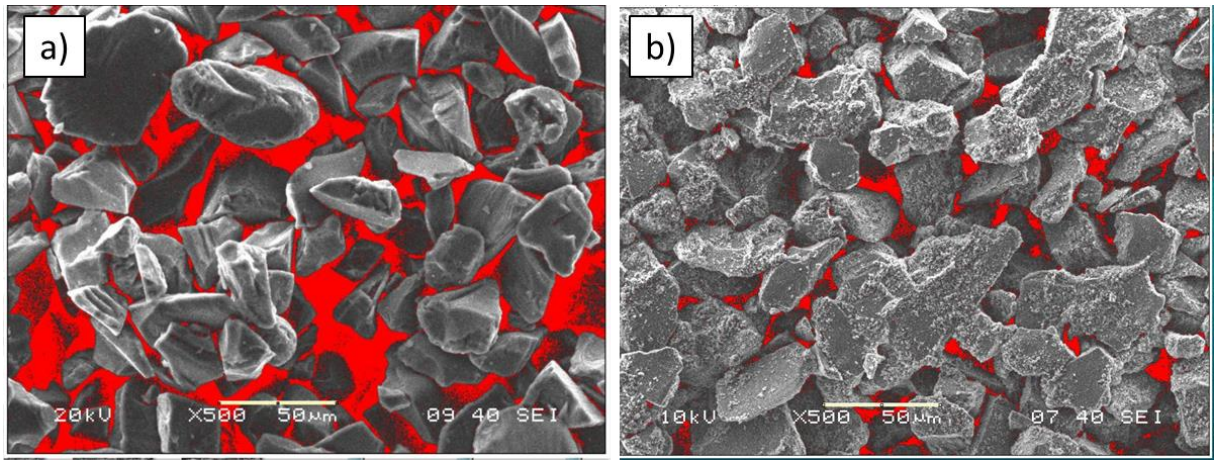


FIGURE 2.5: Porosity analysis in ImageJ using SEM micrographs of hand-pressed discs at room temperature using a) pre-treated SiC 40µm powders and b) nano-micro SiC mixture.

2.3.2. Effect of NaOH concentration on the structure and properties of the 3D-printed SiC discs

Immersing thermally treated SiC discs in NaOH then subjecting the samples to a second heat treatment at 800-1000 °C resulted in the formation silica droplets which served as nucleation sites for the growth of silica nanowires (Figure 2.6). As the NaOH concentration increased the number of the nanowires that bridged the wall of the pores increased (Figure. 2.6).

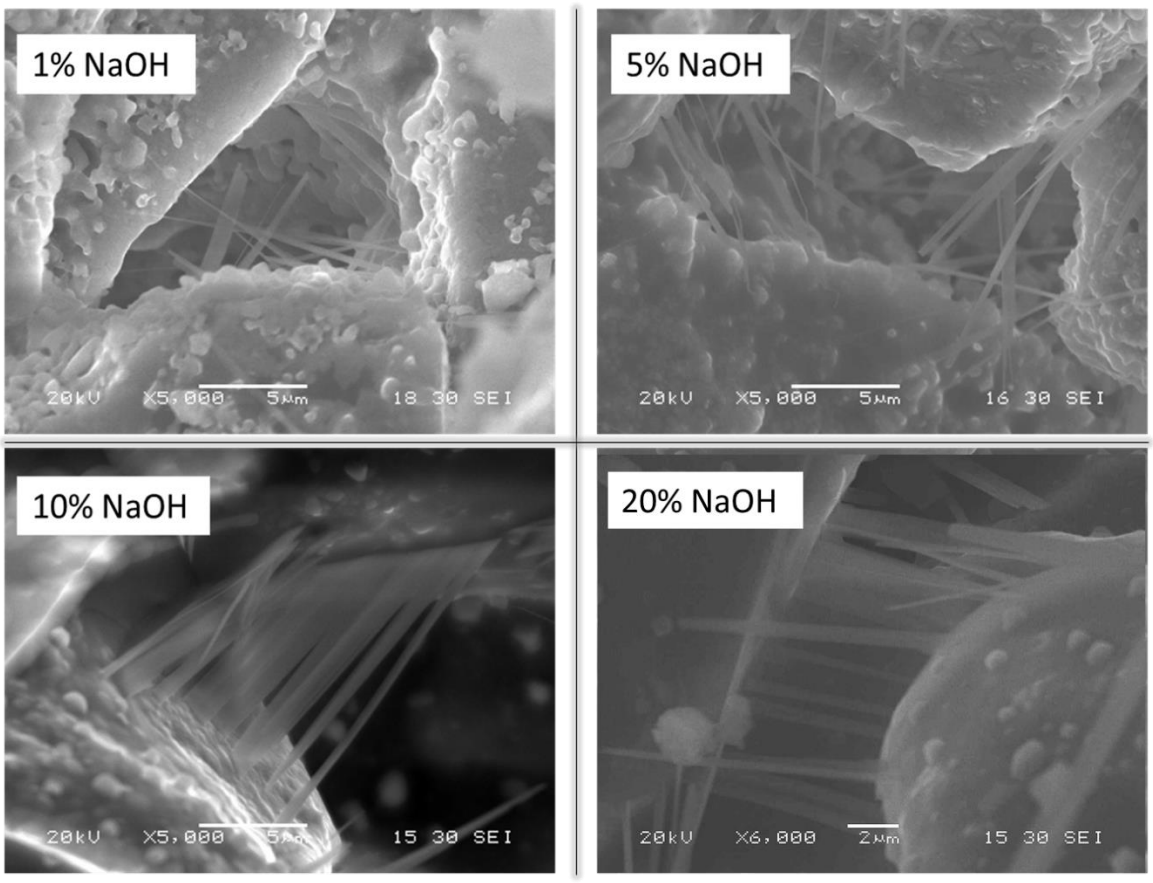


FIGURE 2.6: SEM images of the fracture surface of the 3D printed discs from nano-micro powder mixture showing nucleation and growth of silica nanowires in the 3D printed samples heat treated at 800 °C for 2h

2.3.2.1. Density of 3D printed samples treated with various concentrations of NaOH

Statistical analysis showed that the density of the samples heated at 800 ºC/2h + 10% NaOH/10 min + 800 ºC/2h is significantly higher ($p < 0.002$) than that treated with 20% NaOH (Figure 2.7) with the same heat treatment protocol. Comparable densities were observed for samples treated with 5% and 10% NaOH. Samples treated with 1% NaOH did not keep its mechanical integrity during density measurements therefore it was excluded from further analysis.

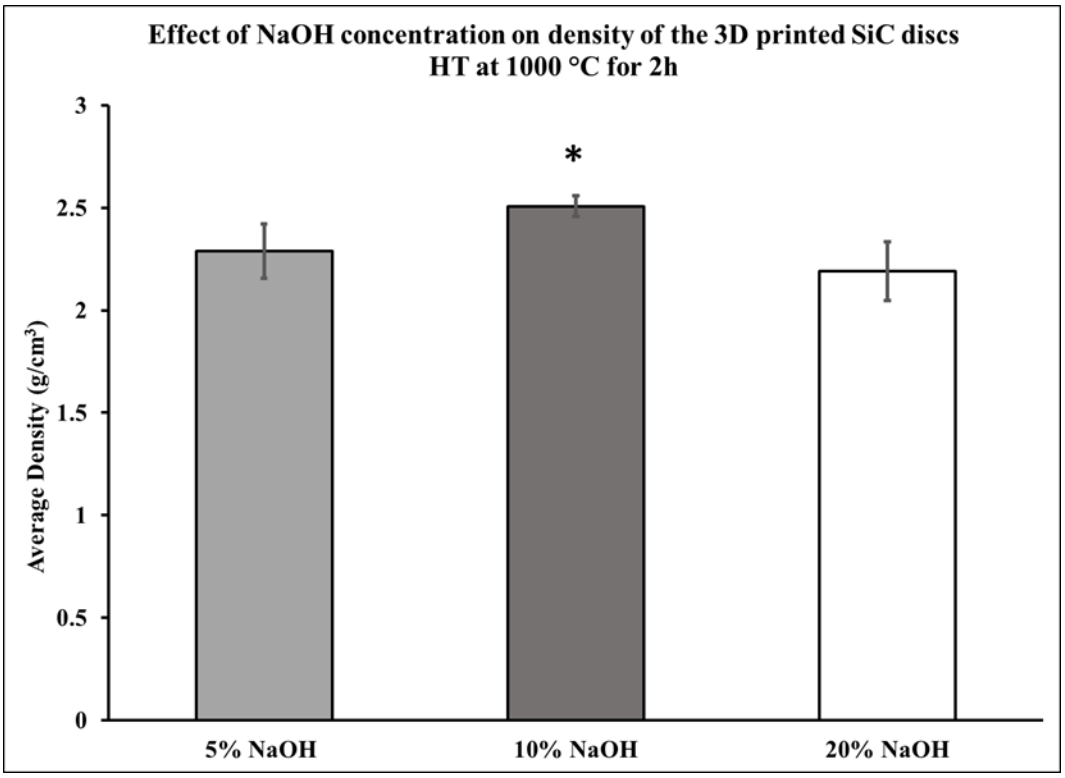


FIGURE 2.7: Density data of the 3D printed discs from nano-micro powder mixture, impregnated at varying concentrations of NaOH and heat treated at 1000 ºC for 2h, (* indicates $p<0.05$)

2.3.3. Effect of post-processing temperature prior to impregnation on the structure

2.3.3.1. FTIR analysis

The 3D-printed discs from the nano-micro powder mixture were separated into two batches. The first batch was heat treated to 900 ºC for 2 h and impregnated in 20% NaOH/10 min and dried at 100 ºC for 24 h in the drying oven. The second batch was heat treated to 650 ºC for 5 h and the excess loose particles on the 3D printed discs were removed using a slight air pressure connected to the Projet460Plus. These discs were then impregnated in 20% NaOH/10 min and dried at 100 ºC for 24 h in the drying oven. The samples were heat treated at 650 ºC/5 h + 20% NaOH/10 min showed more pronounced bands for (Si-O-Si, Si=O, Si-O, Si-Si, Si≡O and silicate rings [30-33]) (Fig. 2.8).

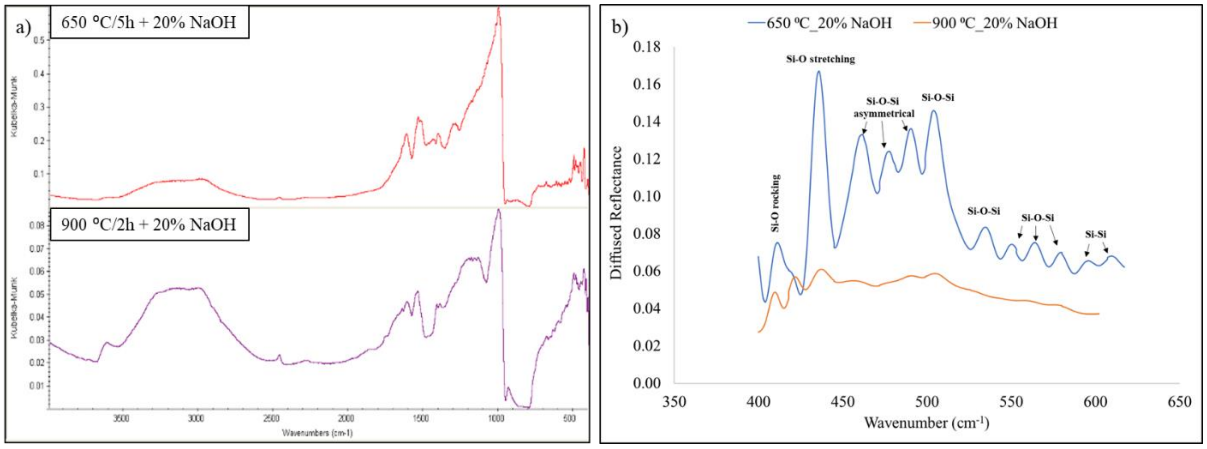


FIGURE 2.8: FTIR graph showing the domination of the surface with Silica layer after dual treatemnt at 650 °C/5h + 20% NaOH/10 min on the fracture surface of 3D printed discs using 70:30 nano-micro mixture SiC powders. The identifications of the silicate bands was refernced in the literature [30-33]. The 3D printed discs heated at 900 °C/2h + 20% NaOH/10 min showed low intesity silicate bands indicating low concetrations of silica on the material surface.

2.3.3.2. Effect of thermal treatment on the thickness of the bonding zone

Figure 2.9a shows the average width of the bonding zone between SiC particles in discs prepared manually by pressing SiC particles pretreated with 1%, 10%, or 20% NaOH and then treating them at 650 °C/5 h. There average bonding zone for particles treated with 1% NaOH was 2.07 ± 0.79 μm and after heat treatment, the thickness was 2.09 ± 0.73 μm. Statistical analysis showed no significant difference in the width of the bonding zone before and after treatment at 650 °C. On the other hand, the bonding zone between particles pretreated with 10 % or 20% NaOH were 5.08 ± 2.49 μm and 5.40 ± 1.86 μm, respectively which were significantly higher ($p < 3.06E-09$ and $p < 8.46E-06$, respectively) than that between particles pre-treated with 1% NaOH at room temperature. After thermal treatment the thickness of the silica bonding zone for SiC particles pretreated with 10% NaOH or 20% NaOH were significantly lower than that

prior to heat treatment (Table 2.1). Figure (2.9b) and Table 2.1 demonstrates the differences in the thickness of the silica bonding zone before and after thermal treatment for the three groups.

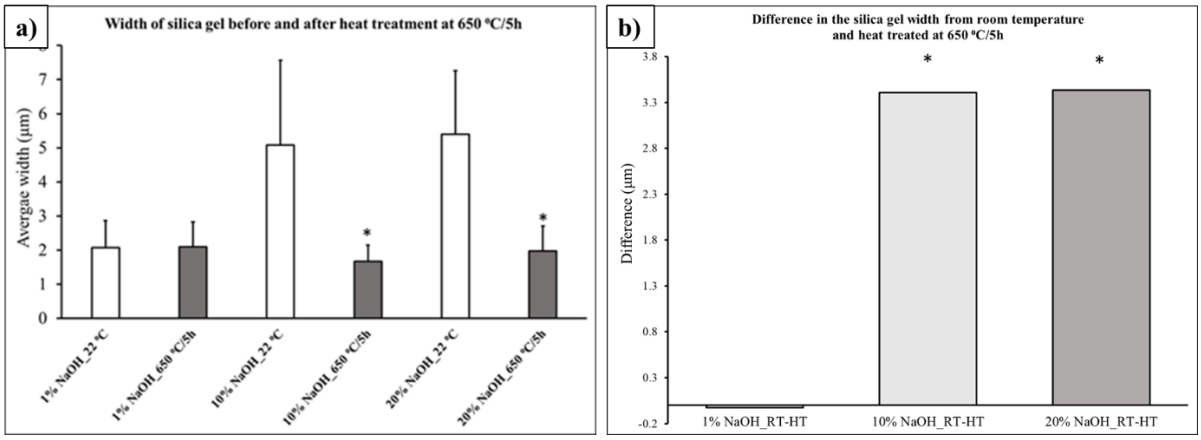


FIGURE 2.9: Average width of the silica gel layer between SiC particles in discs before and after heat treatment at 650 °C/5h. The particles used to prepare the discs were pretreated with 1, 10 and 20% NaOH.

TABLE 2.1: Average width of the silica gel bonding zone before heat treatment of 3D printed SiC discs in comparison with the width of the silica bonding zone after heat treatment at 650 ºC/5h. RT =Room temperature, HT = Heat treated

| Sample type | Average | SD | Difference | p-value |
|---|---|---|---|---|
| 1% NaOH_RT | 2.07 | 0.79 | | |
| 1% NaOH_HT | 2.09 | 0.73 | -0.03 | 0.91 |
| 10% NaOH_RT | 5.08 | 2.49 | | |
| 10% NaOH_HT | 1.67 | 0.46 | 3.41 | 1.02E-07 |
| 20% NaOH_RT | 5.40 | 1.86 | | |
| 20% NaOH_HT | 1.97 | 0.73 | 3.43 | 1.70E-09 |

2.3.3.2.1 Effect of dual heat treatment and second NaOH treatment on mechanical properties of the 3D printed SiC discs

Compressive strength measurements showed a significant ($P < 0.001$) increase in the mechanical strength for 3D printed SiC samples (n=7) subjected to dual thermal treatment at 900 ºC/2h before and after impregnation with 20%NaOH/10 min (Figure. 2.10) in comparison with control samples subjected to one step thermal treatment at 900 ºC/2h without NaOH impregnation.

Moreover, the compressive strength of samples subjected to 650 ºC/5h + 20%NaOH/10 min + 800 ºC/2h was significantly higher ($P < 0.008$) than that of samples subjected to dual thermal treatment at 900 ºC/2h before and after impregnation with 20%NaOH/10 min or samples subjected one step treatment at 900 ºC/2h ($P < 1.67$ E -06).

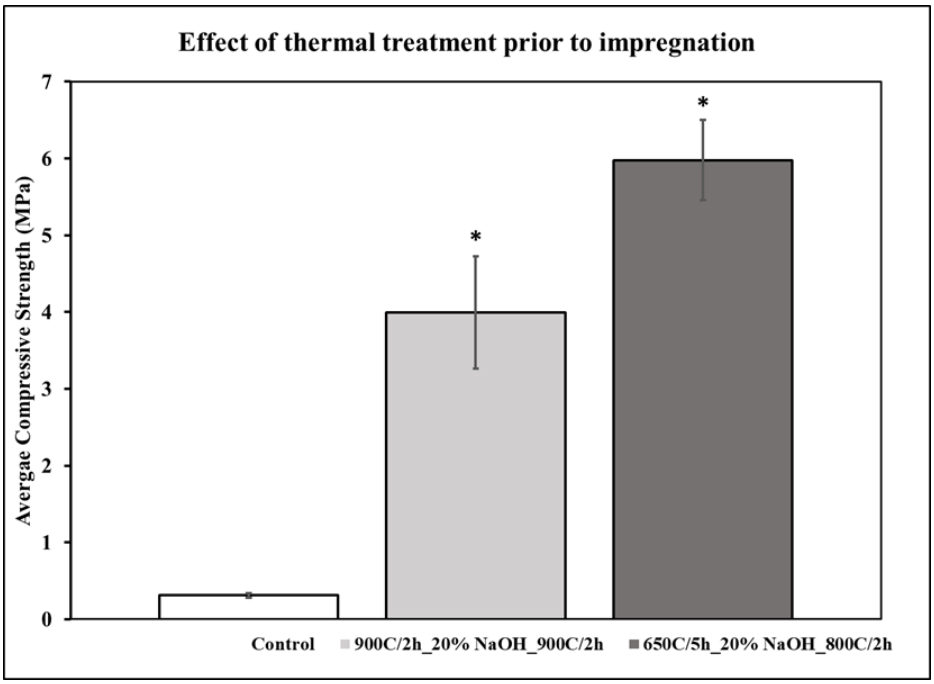


FIGURE 2.10: Comparison of the average compressive strength of 3D printed discs prepared with nano-micro SiC powder mixture and subjected to: single step heat treatemtn at 900 °C/2h, dual thermal treatment at 900 ºC/2h before and after impregnation with 20%NaOH/10 min and dual thermal treatment at 650 ºC/5h + 20%NaOH/10 min + 800 ºC/2h

As Fig 2.10 showed that the 3D printed discs from the nano-micro SiC mixture showed superior mechanical strength when subjected to dual thermal treatment at 650 ºC/5h + 20%NaOH/10 min + 800 ºC/2h. We decided to study the effect of increasing the temperature of the scond heat treatment step on the compressive strength. Statistical analysis showed no significant difference in compressive strength between samples treated at 650 ºC/5h + 20% NaOH/10 min + 800 ºC/2h and 650 ºC/5h + 20% NaOH/10 min + 1000 ºC/2h (Figure 2.11). The importance of the NaOH treatment after the first heat treatment is evident by the comparison between samples thermal treated without second NaOH immersion. The compressive strength of samples subjected to dual heat treatment at 650 ºC/5h + 800 ºC/2h was significantly lower ($P < 1.39E-06$) than that treated at 650 ºC/5h + 20% NaOH/10 min + 800 ºC/2h. Moreover, the compressive strength of samples subjected to dual heat treatment at 650 ºC/5h + 1000 ºC/2h was significantly lower ($P < 0.0003$) than that treated at 650 ºC/5h + 20% NaOH/10 min + 1000 ºC/2h (Figure 2.11). The strength of 3D printed samples treated at 650 ºC/5h + 1000 ºC/2h was significantly higher than that treated at 650 ºC/5h + 800 ºC/2h.

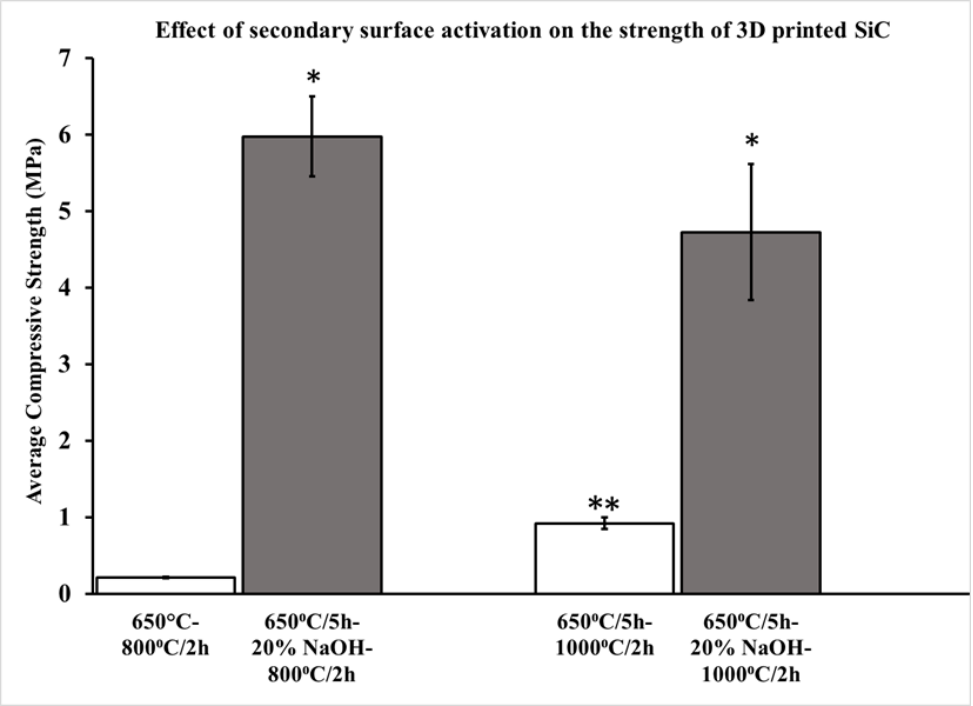


FIGURE 2.11: Average compressive strength of 3D printed discs from nano-micro powder mixture before and after impregnation prior to heat treatment. * - p value between samples with and without impregnation. ** - p value between the samples without impregnation.

The measurements on the size of the droplets and growth of silica nanowires corresponding to the size of the nucleation droplet on the fractured surface of 3D printed SiC discs heat treated at 650 ºC/5h + 20% NaOH + 1000 °C for 2h were observed using SEM (Figure 2.12). The figure shows various sizes and shapes of silica droplets or crystallites with widths ranging from 179 nm to 1.5 μm. Silica nanowires of width ranging from 160 nm to 1.2 μm were observed. These observations suggest that the growth of nanowires was directly related to the size of the silica droplets (Figure 2.12 b). Figure 2.13 shows thin to thick nanowires are grown at the at the surface of the pores.

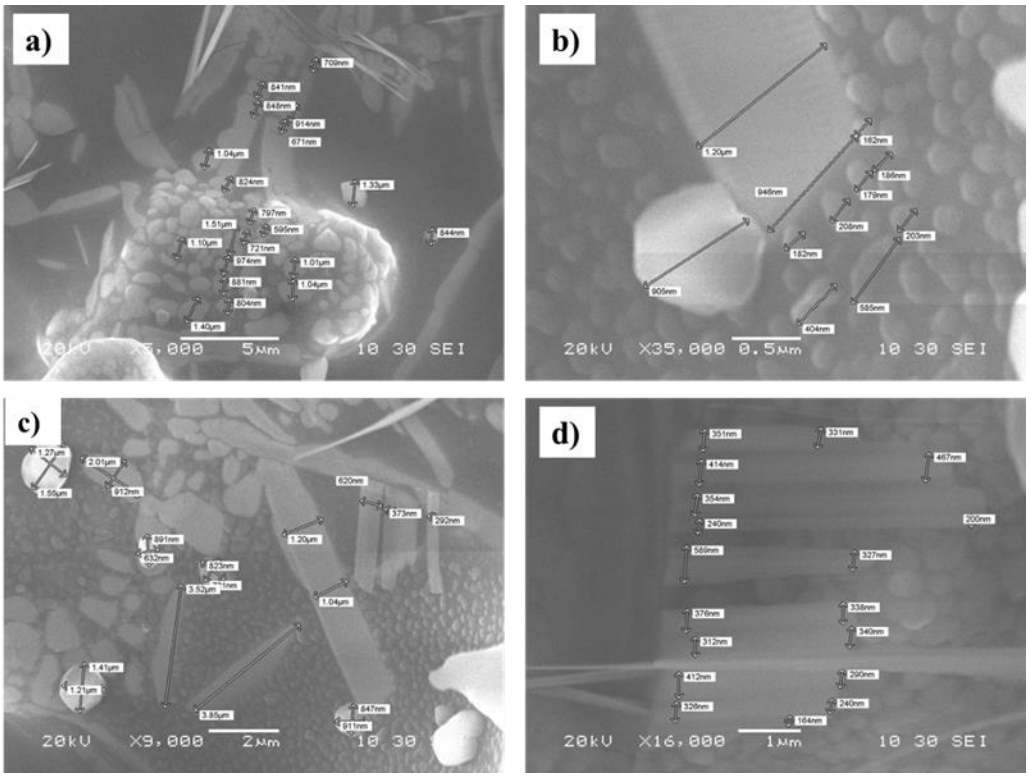


FIGURE 2.12: SEM image showing measurements on the size of the droplets and growth of silica nanowires corresponding to the size of the nucleation droplet on the fractured surface of 3D printed SiC discs heat treated at 650 ºC/5h + 20% NaOH + 1000 °C for 2h.

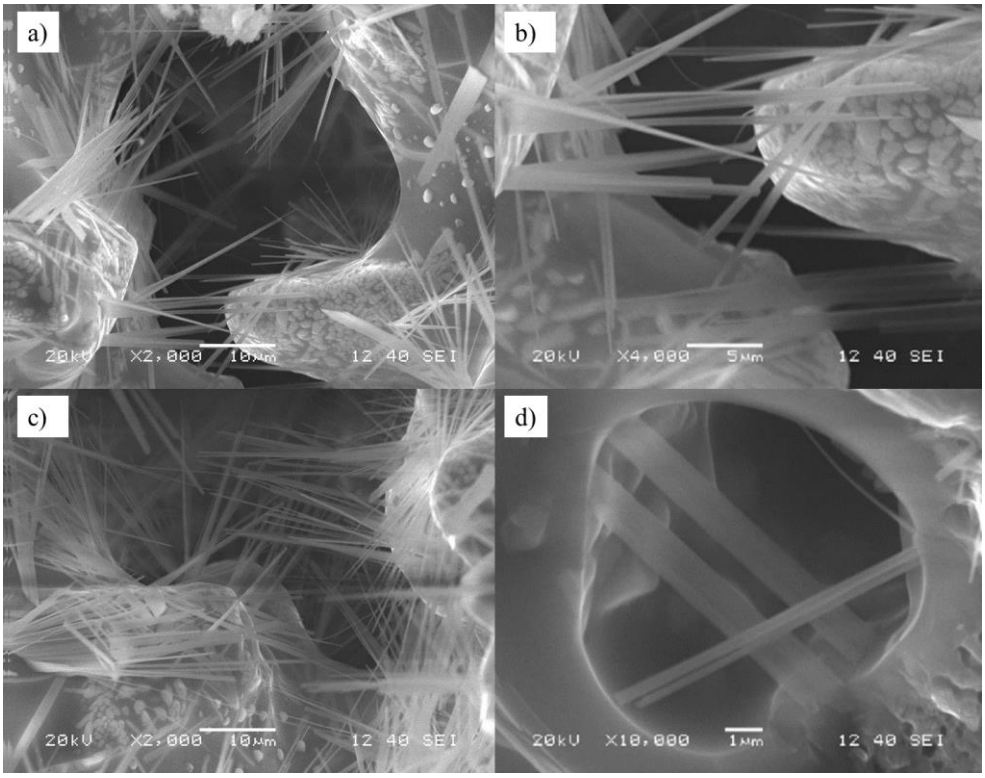


FIGURE 2.13: SEM micrographs of the fractured surface showing the growth of nanowires of 3D printed SiC discs impregnated in 20% NaOH and heat treated at 1000 °C for 2h

2.3.4. Effect of oxygen environment during sintering and strengthening of the 3D printed SiC discs

The 3D printed discs printed from nano-micro powder mixture were sintered at 650 ºC/5h + 20% NaOH/10min + 650 ºC/5h + 800 ºC/2h in air and in an oxygen environment to understand the effect of oxygen in the growth of nanowires. This is a multistep heat treatment process and the growth of nanowires in this experiment should not be compared to Figure 2.6. Figure 2.14a shows the formation of large nucleation droplets at the same temperature without oxygen and on the other hand, Figure 2.14b shows the growth of thin nanowires of an average size of 200 nm at 800 °C for 2 h in an oxygen environment. Figure 2.15 shows SEM images of the $SiO_2$ droplets after heat treatment at 650 ºC/5h + 20% NaOH/10min + 650 ºC/5h + 800

ºC/2h in air and in an oxygen environment. Upon heat treatment, the water molecules evaporate from the silica gel and the material matures into $SiO_2$ droplets (Figure 2.15b). On the other hand, due to the adequate availability of oxygen, matured silica crystals were formed (Figure 2.15d). Even though the density of the silica crystals was comparable with and without oxygen environment, the density of nanowires for the samples heat treated in an oxygen atmosphere was prominent. The EDX in Figure 2.15 shows the elemental composition of the nucleation droplets formed at 800 °C/2h in an oxygen environment having an atomic ratio of 1: 2.4 for Si and O showing adequate availability of oxygen to form $SiO_2$ nanowires.

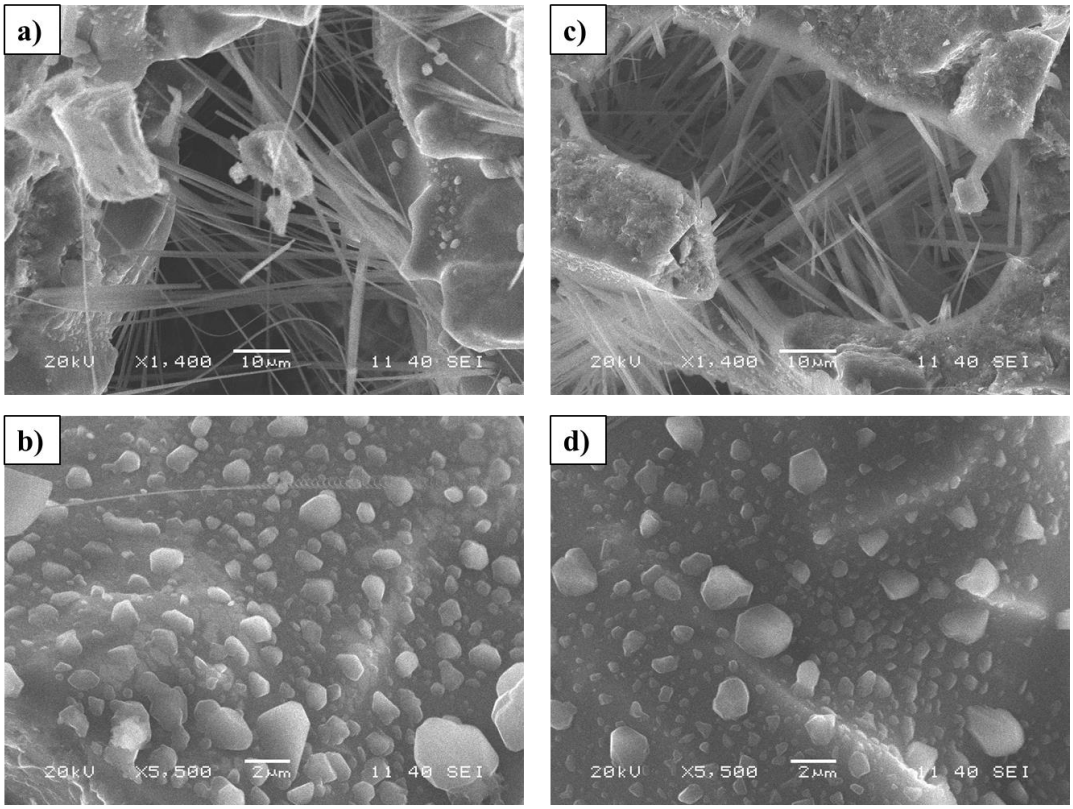


FIGURE 2.14: SEM Micrographs of 3D printed discs heat treated at 650 ºC/5h + 20% NaOH/10mins + 650 ºC/5h + 800 ºC/2h showing nanowires and silica crystallites a) and b) in air, and c) and d) in an oxygen environment

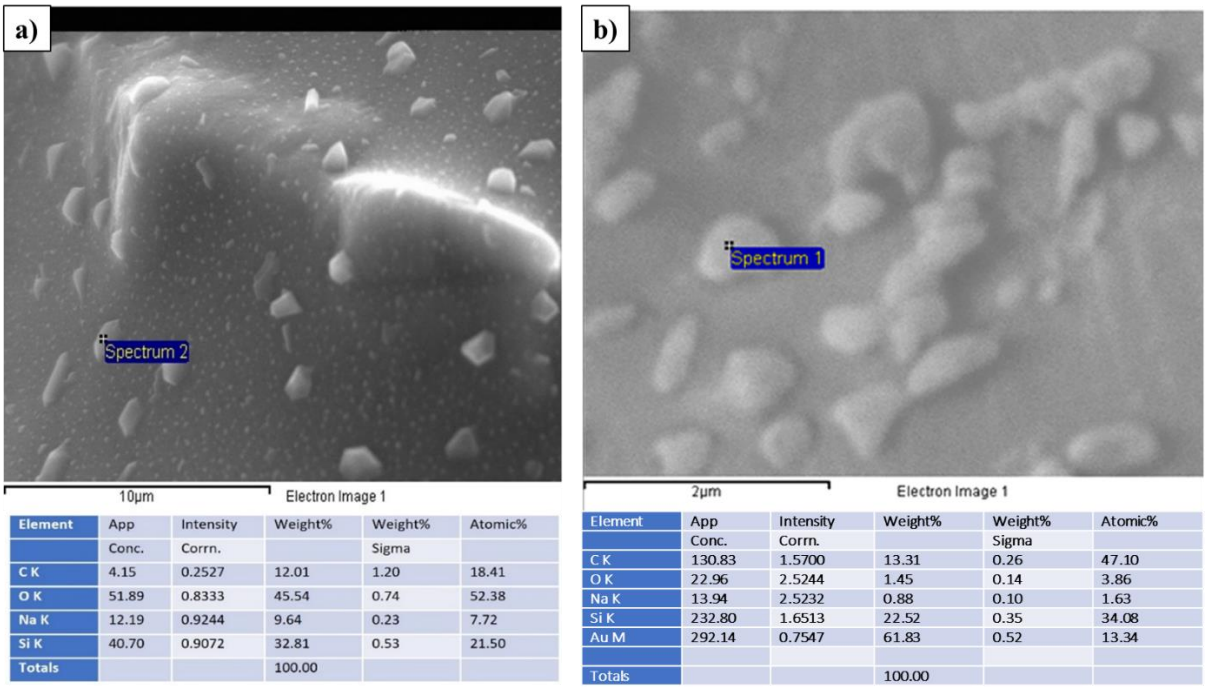


| Element | App Conc. | Intensity Corrn. | Weight% | Weight% Sigma | Atomic% |
|---|---|---|---|---|---|
| C K | 4.15 | 0.2527 | 12.01 | 1.20 | 18.41 |
| O K | 51.89 | 0.8333 | 45.54 | 0.74 | 52.38 |
| Na K | 12.19 | 0.9244 | 9.64 | 0.23 | 7.72 |
| Si K | 40.70 | 0.9072 | 32.81 | 0.53 | 21.50 |
| Totals | | | 100.00 | | |

| Element | App Conc. | Intensity Corrn. | Weight% | Weight% Sigma | Atomic% |
|---|---|---|---|---|---|
| C K | 130.83 | 1.5700 | 13.31 | 0.26 | 47.10 |
| O K | 22.96 | 2.5244 | 1.45 | 0.14 | 3.86 |
| Na K | 13.94 | 2.5232 | 0.88 | 0.10 | 1.63 |
| Si K | 232.80 | 1.6513 | 22.52 | 0.35 | 34.08 |
| Au M | 292.14 | 0.7547 | 61.83 | 0.52 | 13.34 |
| | | | | | |
| Totals | | | 100.00 | | |

FIGURE 2.15: EDX analysis of the nucleation droplets on the 3D printed discs a) heat treated in oxygen atmosphere after impregnation in 20% NaOH and heat treated at 650 ºC/5h + 20% NaOH/10mins + 650 ºC/5h + 800 ºC/2h, b) Loose SiC particles pre-treated with 20% NaOH at room temperature and dried in the oven for 100 ºC for 24 h.

## 2.4. Discussions

Porosity is a challenge to eliminate in the powder bed binder jetting technique. Coarser particle sizes are generally preferred for powder beds as they are easy to spread in the build bed. However, using coarse particles compensates highly for the packing density of the printed part due to the creation of pores at the interspace between SiC particles. Hence, the parts printed using the powder bed are usually porous due to the poor packing density of the powder upon printing [39,40,41]. In this study, the 3D printed discs that were printed only using surface-activated 40 µm SiC showed high percent porosity and large pore size (Figure. 2.5a). On the other hand, mixing of coarser particles of SiC with the finer particles of size 600 nm and 2 µm reduced the porosity by 50%. This showed that the inclusion of finer particles mechanically

filled the interspace between the pores that were created while printing. It was reported that by using bimodal powder mixtures, the powder packing density, flowability, and sintering density were tremendously improved. This was also found to reduce the shrinkage of the sintered part [39].

To densify and strengthen the 3D printed SiC green parts, post-processing techniques like silicone polymer impregnation, phenolic resin impregnation, pyrolysis, chemical vapor in-filtration, or reactive melt infiltration were performed [41,42,43]. In some cases, an additional carbonization technique is required before the infiltration of silicon to reduce the residual silicone content. The residual silicon content is not desirable for high-temperature applications and for the production of complex geometries due to the poor dimensional stability upon sintering [44]. In this study, we report a secondary surface activation on the 3D-printed discs to produce a silica gel layer. Moreover, a pre-sintering heat treatment at 650 ºC before the secondary surface activation facilitated the formation of Si-O bands (Figure 2.8) which imparted handling strength and stability to the green part. Secondary surface activation at various concentrations of NaOH showed the formation of thick and dense silica nanowires at 10% and 20% NaOH concentrations (Figure 2.6). The objective was to select an optimal NaOH concentration that enhances densification and mechanical properties based on the rationale that the NaOH attacks the network bonding of SiC and forms a silica gel layer. The Silica gel layer upon dehydration and heat treatment would facilitate the crystal growth of $SiO_2$. However, the densities of discs treated at 5%, and 20% were comparable and did not show a significant difference between the groups. A significant increase in the density was observed for the samples treated with 10% NaOH concentration (Figure. 2.7). The reduction of the density of the SiC-Silica composite prepared using SiC particles pretreated with 20% NaOH can be attributed

to the formation of more silica gel and the presence of a large number of -OH groups [36]. The density of pure phases of SiC and $SiO_2$ are 3.2 g/cc and 2.65 g/cc. From the rule of mixtures, the composite density was measured from the volume percent of the phases present. Previous publications from our lab showed that the 20% NaOH increased the density and strength by creating more silica gel and nanowires [34-38]. So, the 3D printed discs were impregnated in 20% NaOH and then heat treated at various temperatures. Figure 2.11 shows that the introduction of secondary surface modification has improved the mechanical strength by more than 70% for all temperatures.

The 3D printed discs that were heat treated to 650 ºC for 5 h before impregnation showed a 100% increase in strength after sintering. At 650 ºC, the hydrogen bonding of the silanol groups was found to condense to form siloxane bonding which reduces the possibility of the adsorption of more -OH groups [45]. The FTIR graph in Figure 2.8 proves this fact. Furthermore, it increases the possibility of the adsorption of oxygen molecules to form $SiO_2$. The width of the silica gel layer that mediates the bonding between SiC particles was significantly reduced after heat treatment at 650 °C for the discs that were treated with 10% and 20% NaOH. The reduction in the width of the silica gel layer was attributed to (i) the shrinkage of the silica layer as it crystallizes and (ii) the dehydration of -OH from Si-OH while forming siloxane bonding and thus fusing the SiC particles together. Due to these reasons, the as-printed part upon heat treatment at 650 °C showed good handling strength. The large standard deviations in the width measurements are because the silica gel formation is non-homogenous within the sample due to using the pre-sintering step before impregnation also allowing for the reduction of the sintering temperature and yet obtaining a better mechanical strength. The mechanical strength was attributed to the growth of silica nanowires along the interface and within the pores. Hence, the inclusion of the

pre-sintering step before secondary surface activation greatly improved the strength of the 3D-printed part upon sintering at relatively lower temperatures.

The compression strength of the 3D printed samples that are pre-sintered at 650 °C then treated at sintering temperatures 800 °C, 900 °C, 1000 °C showed a significant increase in the strength at 1000 °C. Temperature facilitates the growth of nanowires which grow within the pores and the grain boundaries that densify the material. At 800 °C, the formation of many $SiO_2$ droplets with an average height of 0.58 ± 0.12 µm was observed. Whereas, at 1000 °C, the droplet height doubled to 1.19 ± 0.18 µm along with the enormous growth of nanowires. It is evident that the increase in temperature allowed for the growth of the droplets to nanowires. At 1000 ºC, the 3D-printed discs that were pre-sintered and secondary modified with 20% NaOH showed a significant increase in strength from 0.9 MPa (for control) to 5 MPa. Sintering and dwelling are crucial parameters for diffusion and crystal growth. Niu et.al. demonstrated an in-situ measurement technique of the solid-state sintering process of SiC. It was reported that the sintering of irregularly shaped (polyhedron) SiC particles needed more time to sinter as the surface diffusion between particles was increased due to a large specific surface area [46]. Hence the samples treated at 1000 °C for 24 h after secondary surface modification showed a tremendous increase in strength to 11 MPa from 5 MPa (1000 °C/2 h). Two factors that are responsible for this increase are, i) the formation of silica gel that helps in enhancing surface diffusion as it softens the edges of the SiC particles, and ii) the complete transformation of the silica droplets to nanowires. It was interesting to see that the direction of growth is either perpendicular or radial to the surface of the droplet and this could be explained by the condensation of the SiO (g) either on the top of the droplet or to its sidewalls. The ability of the $SiO_2$ droplet to grow silica nanowires depends on many factors including the size and the

orientation of the crystals as well as the silicon-to-oxygen ratio within the droplet itself. The silica nanowire growth mechanism in this study is similar to the Vapor-solid mechanism. The mechanism in this paper is believed to be a self-catalytic growth vapor solid mechanism [47,48]. In the surface activation method, the dehydrated Si-OH forms $SiO_2$ droplets which on heat treatment release SiO (g) which further reacts with $O_2$ to form $SiO_2$ (s) which is adsorbed to the nucleation sites created by the droplets to form silica nanowires (Figure 2.14b and d).

The formation of $SiO_2$ nanowires requires diffusion and deposition of oxygen onto oxygen-deprived SiO nucleation droplets (Figure 2.15.). Hence the introduction of an oxygen environment promoted the growth of nanowires even at temperatures as low as 800 °C. The 3D-printed discs that were pre-sintered at 650 ºC/5h and secondary modified with 20% NaOH/10 min were sintered at 800 °C in an oxygen atmosphere. The SEM micrographs (Figure. 2.14.b) showed many bright droplets for those samples sintered in oxygen, clearly showing condensation of $SiO_2$ and many thin nanowires of atomic ratio 1: 2.4 for Si and O showing adequate availability of oxygen to form $SiO_2$ nanowires.

On the other hand, the samples treated at 650 ºC/5h + 20%NaOH/10min+ 650 ºC/5h+ 800 °C/2h in the air also showed nucleation droplets at their initial stage of crystal growth and few nanowire growths due to less availability of oxygen. Hence, introducing an oxygen atmosphere during sintering would enhance the growth of silica nanowires at a relatively low temperature of 800 °C, which are essential in the densification and strengthening of the 3D printed SiC parts.

## 2.5. Conclusion

SiC composite disc was successfully printed using powder bed binder jetting technique with water binder. The surface-activated coarse SiC particles (40 μm) along with sub-micro (2 μm) and nanoparticles (600 nm) enabled good spreading of the powders and mechanically filled the voids between particles. Further, the handling strength was improved by heat treating the as-printed green parts at 650 °C. The dehydroxylation and the formation of siloxane bonding helped in the binding of the particles together. The mechanical strength of the printed discs was improved by introducing a secondary surface activation to the printed part which created more Si-O droplets for the formation of silica nanowires at 800 °C to 1000 °C. The effect of the concentration of NaOH, and at different temperatures were studied. The optimal concentration of NaOH, temperature, and dwell time was found to be 10%, 1000 °C, and 2 h. At these parameters, the structural integrity of the sample was not affected, meaning, the sample held its dimensions without any deformation. The effect of oxygen atmosphere in the growth of silica nanowires was studied in comparison to the samples heat treated in air. The fracture surface morphology (SEM) and the elemental analysis (EDS) suggested that the oxygen environment can trigger the growth of silica nanowires at a relatively low temperature of 800 ºC. Overall, the use of nano-micro powder mixture, formation of silica gel on the printed discs, and multi-step thermal treatments improved the strength of the 3D-printed SiC composite printed using the powder bed binder jetting technique.

# REFERENCES


1. Bengisu M (2013) Engineering ceramics. Springer Science & Business Media.

2. Wang, J. C., Dommati, H., & Hsieh, S. J. (2019). Review of additive manufacturing methods for high-performance ceramic materials. *The International Journal of Advanced Manufacturing Technology*, *103*, 2627-2647.

3. Johnson, J. S., Grobsky, K. D., & Bray, D. (2002, September). Rapid fabrication of lightweight silicon-carbide mirrors. In *Optomechanical Design and Engineering 2002* (Vol. 4771, pp. 243-253). SPIE.

4. Yan, C., Lifeng, W., & Jianyue, R. (2008). Multi-functional SiC/Al composites for aerospace applications. Chinese Journal of Aeronautics, 21(6), 578-584.

5. Robichaud, J., Guregian, J. J., & Schwalm, M. (2003, November). SiC optics for Earth observing applications. In Earth Observing Systems VIII (Vol. 5151, pp. 53-62). International Society for Optics and Photonics.

6. Tobin, E., Magida, M. B., Kishner, S. J., & Krim, M. H. (1995, October). Design, fabrication, and test of a meter-class reaction bonded SiC mirror blank. In Silicon Carbide Materials for Optics and Precision Structures (Vol. 2543, pp. 12-21). International Society for Optics and Photonics.

7. Casady, J. B., & Johnson, R. W. (1996). Status of silicon carbide (SiC) as a wide-bandgap semiconductor for high-temperature applications: A review. *Solid-State Electronics*, *39*(10), 1409-1422.

8. Han, L., Liang, L., Kang, Y., & Qiu, Y. (2020). A review of SiC IGBT: models, fabrications, characteristics, and applications. *IEEE Transactions on Power Electronics*, *36*(2), 2080-2093.

9. Yuan, X. (2017, October). Application of silicon carbide (SiC) power devices: Opportunities, challenges and potential solutions. In *IECON 2017-43rd annual conference of the IEEE industrial electronics society* (pp. 893-900). IEEE.

10. She, X., Huang, A. Q., Lucia, O., & Ozpineci, B. (2017). Review of silicon carbide power devices and their applications. *IEEE Transactions on Industrial Electronics*, *64*(10), 8193-8205.

11. Katoh, Y., Snead, L. L., Henager Jr, C. H., Nozawa, T., Hinoki, T., Iveković, A., ... & De Vicente, S. G. (2014). Current status and recent research achievements in SiC/SiC composites. *Journal of Nuclear Materials*, *455*(1-3), 387-397.

12. Katoh, Y., Snead, L. L., Szlufarska, I., & Weber, W. J. (2012). Radiation effects in SiC for nuclear structural applications. *Current Opinion in Solid State and Materials Science*, *16*(3), 143-152.

13. Koyanagi, T., Terrani, K., Harrison, S., Liu, J., & Katoh, Y. (2021). Additive manufacturing of silicon carbide for nuclear applications. *Journal of Nuclear Materials*, *543*, 152577.

14. Saddow, S. E., Frewin, C. L., Araujo Cespedes, F., Gazziro, M., Bernadin, E., & Thomas, S. (2016, June). SiC for biomedical applications. In *Materials Science Forum* (Vol. 858, pp. 1010-1014). Trans Tech Publications Ltd.

15. Frewin, C. L., Coletti, C., Register, J. J., Nezafati, M., Thomas, S., & Saddow, S. E. (2015). Silicon carbide materials for biomedical applications. *Carbon for Sensing Devices*, 153-207.

16. Alhosseini, S. H. N., & Mousavi, S. R. (2019). The effect of oxide, carbide, nitride and boride additives on properties of pressureless sintered SiC: A review. *Journal of the European Ceramic Society*, *39*(7), 2215-2231.

17. Lewis, J. A. (2000). Colloidal processing of ceramics. *Journal of the American Ceramic Society*, *83*(10), 2341-2359.

18. Wu, C., Pang, J., Li, B., & Liang, S. Y. (2019). High-speed grinding of HIP-SiC ceramics on transformation of microscopic features. *The International Journal of Advanced Manufacturing Technology*, *102*, 1913-1921.

19. He, R., Zhou, N., Zhang, K., Zhang, X., Zhang, L., Wang, W., & Fang, D. (2021). Progress and challenges towards additive manufacturing of SiC ceramic. *Journal of Advanced Ceramics*, *10*, 637-674.

20. Lv, X., Ye, F., Cheng, L., Fan, S., & Liu, Y. (2019). Binder jetting of ceramics: Powders, binders, printing parameters, equipment, and post-treatment. *Ceramics International*, *45*(10), 12609-12624.

21. Suwanprateeb, J., Sanngam, R., & Panyathanmaporn, T. (2010). Influence of raw powder preparation routes on properties of hydroxyapatite fabricated by 3D printing technique. *Materials Science and Engineering: C*, *30*(4), 610-617.

22. Williams, C. B., Cochran, J. K., & Rosen, D. W. (2011). Additive manufacturing of metallic cellular materials via three-dimensional printing. *The International Journal of Advanced Manufacturing Technology*, *53*, 231-239.

23. Yeong, W. Y., Chua, C. K., Leong, K. F., & Chandrasekaran, M. (2004). Rapid prototyping in tissue engineering: challenges and potential. *TRENDS in Biotechnology*, *22*(12), 643-652.

24. Zhou, Z., Buchanan, F., Mitchell, C., & Dunne, N. (2014). Printability of calcium phosphate: calcium sulfate powders for the application of tissue engineered bone scaffolds using the 3D printing technique. *Materials Science and Engineering: C*, *38*, 1-10.

25. Butscher, A., Bohner, M., Roth, C., Ernstberger, A., Heuberger, R., Doebelin, N., ... & Müller, R. (2013). Printability of calcium phosphate powders for 3D printing of tissue engineering scaffolds. *Powder based three-dimensional printing of calcium phosphate structures for scaffold engineering*, *8*, 47.

26. Wilhelm, M., Kornfeld, M., & Wruss, W. (1999). Development of SiC–Si composites with fine-grained SiC microstructures. Journal of the European Ceramic Society, 19(12), 2155-2163.

27. Amirthan, G., & Balasubramanian, M. (2011). Thermal conductivity studies on Si/SiC ceramic composites. Ceramics International, 37(1), 423-426.

28. Bredt, J. F., Anderson, T. C., & Russell, D. B. (2002). *U.S. Patent No. 6,416,850*. Washington, DC: U.S. Patent and Trademark Office.

29. Feenstra, F. K. (2005). *U.S. Patent No. 6,921,500*. Washington, DC: U.S. Patent and Trademark Office.

30. Oh, T., & Choi, C. K. (2010). Comparison between SiOC thin films fabricated by using plasma enhance chemical vapor deposition and SiO2 thin films by using fourier transform infrared spectroscopy. J. Korean Phys. Soc, 56(4), 1150-1155.

31. Widjonarko, D. M., Jumina, J., Kartini, I., & Nuryono, N. (2014). Phosphonate Modified Silica for Adsorption of Co (II), Ni (II), Cu (II), and Zn (II). Indonesian Journal of Chemistry, 14(2), 143-151.

32. Nibou, D., Amokrane, S., Mekatel, H., & Lebaili, N. J. P. P. (2009). Elaboration and characterization of solid materials of types zeolite NaA and faujasite NaY exchanged by zinc metallic ions Zn2+. Physics Procedia, 2(3), 1433-1440.

33. Ivashchenko, L., Vasin, A., Ivashchenko, V., Ushakov, M., & Rusavsky, A. (2006). Blue light emission from PECVD deposited nanostructured SiC. MRS Online Proceedings Library (OPL), 910.

34. El-Ghannam, T. Schmitz, Advanced 3D Printing of Silicon Carbide Based Optics through Amazon Crystal Growth, Application Number 62447641, Jan (2017).

35. El-Ghannam, M. Greenier, M. Johnson, I. Marriott, Synthesis and characterization of porous bioactive SiC tissue engineering scaffold, J. Biomed. Mater. Res. (2020), 10.1002/jbm.a.36973.

36. D. Beasock, T.M. Stokes, A. El-Ghannam, T. Schmitz, Effect of processing parameters on the microstructure and mechanical behavior of a silicon carbide-silica composite, Procedia Manufacturing, 34 (2019), pp. 747-753, 10.1016/j.promfg.2019.06.211.

37. Ahmed El-Ghannam, Sujithra Chandrasekaran, Farjana Sultana, Synthesis and characterization of a novel silica nanowire-reinforced SiC thermal material, Journal of Solid-State Chemistry, Volume 297, 2021, 122055, ISSN 0022-4596, https://doi.org/10.1016/j.jssc.2021.122055.

38. Chandrasekaran, S., El-Ghannam, A., Monroe, J. A., & Xu, C. (2022, October). Thermo-Mechanical Properties of SiC-Mineral Binder Composites for Space Applications. In *ASME International Mechanical Engineering Congress and Exposition* (Vol. 86656, p. V003T04A004). American Society of Mechanical Engineers.

39. Bai, Y., Wagner, G., & Williams, C. B. (2017). Effect of particle size distribution on powder packing and sintering in binder jetting additive manufacturing of metals. *Journal of Manufacturing Science and Engineering*, *139*(8), 081019.

40. Du, W., Singh, M., & Singh, D. (2020). Binder jetting additive manufacturing of silicon carbide ceramics: Development of bimodal powder feedstocks by modeling and experimental methods. *Ceramics International*, *46*(12), 19701-19707.

41. Cramer, C. L., Armstrong, H., Flores-Betancourt, A., Han, L., Elliott, A. M., Lara-Curzio, E., ... & Nawaz, K. (2020). Processing and properties of SiC composites made via binder jet 3D printing and infiltration and pyrolysis of preceramic polymer. *International Journal of Ceramic Engineering & Science*, *2*(6), 320-331.

42. Singh, M., Halbig, M. C., & Grady, J. E. (2015, December). Additive manufacturing of light weight ceramic matrix composites for gas turbine engine applications. In *Advanced Processing and Manufacturing Technologies for Nanostructured and Multifunctional Materials II: A Collection of Papers Presented at the 39th International Conference on Advanced Ceramics and Composites* (pp. 145-150). Hoboken, NJ, USA: John Wiley & Sons, Inc.

43. Polozov, I., Razumov, N., Masaylo, D., Silin, A., Lebedeva, Y., & Popovich, A. (2020). Fabrication of silicon carbide fiber-reinforced silicon carbide matrix composites using binder jetting additive manufacturing from irregularly-shaped and spherical powders. Materials, 13(7), 1766.

44. Fleisher, A., Zolotaryov, D., Kovalevsky, A., Muller-Kamskii, G., Eshed, E., Kazakin, M., & Popov Jr, V. V. (2019). Reaction bonding of silicon carbides by Binder Jet 3D-Printing, phenolic resin binder impregnation and capillary liquid silicon infiltration. *Ceramics International*, *45*(14), 18023-18029.

45. Christy, A. A. (2012). Effect of heat on the adsorption properties of silica gel.

46. Niu, Y., Xu, F., Hu, X., Zhao, J., Miao, H., Wu, X., & Zhang, Z. (2011). In situ investigation of the silicon carbide particles sintering. *Journal of Nanomaterials*, *2011*, 1-6.

47. Kim, M. H., Park, Y. H., Kim, I., Park, T. E., Sung, Y. M., & Choi, H. J. (2010). Self-catalytic growth of silicon nanowires on stainless steel. Materials Letters, 64(21), 2306-2309.

48. Kolasinski, K. W. (2006). Catalytic growth of nanowires: vapor–liquid–solid, vapor–solid–solid, solution–liquid–solid and solid–liquid–solid growth. Current Opinion in Solid State and Materials Science, 10(3-4), 182-191.

# CHAPTER 3: (PAPER 2) STRENGTHENING OF SIC COMPOSITES USING CORDIERITE AND SPODUMENE AS BINDERS: CHARACTERIZATION OF MECHANICAL PROPERTIES, THERMAL SHOCK RESISTANCE, AND DIMENSIONAL STABILITY

Authors

Sujithra Chandrasekaran, Prithiviraj Shanmugam, Konstantinos Falaggis, Ahmed El-Ghannam

## 3.1. Introduction

The difficult processing of pure SiC has prompted the search for the design of a SiC-composite that preserves the excellent mechanical and thermal properties of SiC including high thermal shock resistance, high thermal conductivity, and low thermal expansion. These properties are essential for many aerospace applications including mirrors for telescopes [1-7]. A successful composite design would have components that can form a strong interfacial bond and have comparable thermal and mechanical behavior. Efforts to design SiC composites for optical applications included the use of Si as a filler for porous SiC. This approach successfully was used to make mirrors for satellites and telescopes. However, limitations for the SiC-Si composite include limited mechanical strength and thermal conductivity due to undesirable interfacial events including (i) abnormal growth of SiC particles at the interface between Si and SiC, (ii) inefficient interfacial bond due to the release of CO and SiO gases during infiltration (iii) the aggregation of SiC particles[8], and (iv) the formation of a glassy carbon layer between Si and the SiC [9]. Moreover, the relatively low melting point of silicon restricts the use of SiC-Si for high-temperature applications. Other trials to enhance the densification and mechanical properties of SiC include the addition of sintering aids like MgO, $Al_2O_3$, $Y_2O_3$, and CaO-

produced porous structures due to weight loss during processing [10-14]. Taken altogether, the above studies relied on producing porous SiC and filling in the pores with molten metal or adding sintering aids.

Several other studies have used SiC fibers to reinforce the SiC matrix [15-17] with variable degrees of success. The rationale for using fibers is that the SiC fibers deflect the cracks and thus improve the mechanical properties after processing at high temperatures. However multiple processing steps are needed including, hot pressing at high temperatures in a controlled atmosphere with or without sintering additives. The strength of the composite depends on the amount of oxidative agents added to facilitate the bonding between the SiC fiber and the SiC matrix. The addition of 12-14 wt% oxidative agents resulted in fiber degradation and the formation of weak carbide phases that lead to debonding and pull out of the fibers which resulted in a reduction in the tensile strength of the composites. Lowering the oxidative content to < 1 wt % resulted in a high tensile strength of 2 GPa after sintering at 1500 °C or higher [18]. Other efforts to minimize the SiC fiber degradation employed Al metal powder as a sintering additive to facilitate densification at 1700 ºC. However, the addition of Al to the SiC-SiC fiber composite created a weak interfacial layer made of $Al_4C_3$ and $Al_4SiC_4$. The weak interfacial bond is responsible for the debonding and pullout of the fibers during the mechanical test. Moreover, the $Al_4SiC_4$ interfacial bond has been associated with a significant increase in the strain to failure without affecting the fracture strength. The increase in the strain under mechanical loading is not desirable for optoelectronic applications that require dimensional stability. Thermal shock resistance was studied by quenching the sample in water from 700 ºC. The study did not measure the dimensional stability and reported an increase in the flexural strength after quenching due to

the thermal stress that was created due to the differences in the thermal expansion coefficients between the fibers and the matrix [19].

Cordierite and spodumene are rock-forming minerals characterized by low thermal expansion coefficient, thermal shock resistance, and good mechanical and thermal stability. However, manufacturing pure cordierite bodies is challenged by the need to add sintering aid to get fully dense material. The sintering aid lowers the thermomechanical strength and fracture toughness. Baitalik et.al., used SiC with different particle sizes prepared porous SiC, and infiltrated the material with cordierite sol. The porosity characteristics and mechanical strength of Cordierite-SiC composites were studied after sintering at 1300–1400 °C in air. The flexural strength and modulus of elasticity increased from ~13 – 38 MPa and ~14 – 23 GPa with the increase in the sintering temperature and the decrease in the particle size. The high contact surface area between the small-size SiC particles enhanced the formation of $SiO_2$ in the composite which led to the formation of a glassy phase. The crystallization of the glassy phase at high temperatures resulted in volume shrinkage of the oxide phases which in turn led to an increase in the pore size [20]. The percentage porosity measured was 30–36 vol% with an average pore diameter of ~4–22 μm. Data in the literature reported variations in the flexural strength of porous samples due to variations in the interfacial bond between phases in the composite rather than the porosity characteristics [20-22].

The effect of spodumene liquid phase sintering on the porosity and density of SiC composite was studied [23]. Lu Yuan-Yuan et.al. prepared SiC composites with 25-40 weight percent spodumene and reported an increase in density as the spodumene concentration increased upto 35 % due to pore filling with molten spodumene. A subsequent reduction in density was observed at higher concentrations of spodumene due to poor dispersion of the later component

which lead to pore formation. A similar explanation for the decrease in the density of Spodumene composites with mullite [24] and aluminum titanate [25] was also reported.
In a previous publication, we activated the surface of SiC particles by creating a thin silica gel layer that enhanced densification and strength at relatively low temperatures [26]. This mechanism of densification and strengthening of the porous SiC takes place through the growth of cristobalite nanowires inside the pores [26-28]. In the present study, we examined the ability of Cordierite and spodumene to serve as binders for surface active SiC. The silica gel layer mediated a strong bond between SiC and each mineral binder which resulted in high thermal shock resistance, dimensional stability, and mechanical properties.

## 3.2. Materials & Methods

### 3.2.1. Preparation of cordierite and Spodumene

Appropriate amounts of $MgCO_3$, $Al_2O_3$, and $SiO_2$ (Quartz) were weighed as per stoichiometric ratios to make 40 grams of Indialite (α-cordierite). The weighed ingredients were mixed in a planetary ball mill with alumina balls of diameter 5 mm in a powder/ball ratio of 1:10. Ethanol was used as the solvent medium and its ratio was 20-25% of the mill volume. About 25% of the milling jar was left empty after charging all the materials to ensure proper milling. The milling was done at 180 rpm for 2 hours. After milling, the milled components were transferred to an alumina crucible and dried for 24 hours in a drying oven at 100 ºC. After drying, the powders were sifted to separate the powder from the alumina balls. The powder was heated at 750 ºC/1h at a heating rate of 10 ºC/min to remove volatile compounds and then the temperature was raised at a rate of 1 ºC/min till 1400 ºC and kept for 2 hours dwelling time to create Indialite. Spodumene was prepared following similar preparation procedures. Briefly,

appropriate ratios of $Li_2CO_3$ 11wt%, $Al_2O_3$ 22wt%, and $SiO_2$ 33wt% (Quartz) were milled together in a planetary ball mill for 4hrs. After milling, the powder was dried, sifted, and calcined at 600 ºC/1h at a heating rate of 10 ºC/min to remove the volatile compounds, and the temperature was raised at a rate of 1 ºC/ min to 1000 ºC/2h to form Spodumene.

The prepared cordierite and spodumene compounds were crushed manually into small pieces (approximately 10-15 mm) and further crushed into fine particles in the planetary ball mill for 4h at 200 rpm with ethanol as the medium. The milled powders were then dried in the drying oven at 100ºC for 24 hours. The balls and the powders were then separated by sifting in the mesh of sizes 60, 120, and 200. The final powders that were used to make SiC composites were less than 75 μm.

3.2.2. Preparation of the SiC-mineral composites

The SiC powder of mean size 40 μm (US research nanomaterials, Houston, TX USA) was moistened with 60 μL of 1% NaOH in a mortar and mixed thoroughly with a spatula to ensure complete wetting of the particles. Previous studies from our lab showed the formation of a silica gel layer on the SiC particles after mixing with NaOH at room temperature [26-29]. The cordierite particles (<75 μm) (20 weight %) were added to the NaOH-moistened SiC (80 weight %) and thoroughly mixed using the flat side of the spatula, then blended and ground using a pestle, until the powder looked homogenous. The homogeneity of the powder was ensured by the evenness of the color of the powder mixture. The mixture (1 gm) was pressed uniaxially in a 10 mm diameter die using a hydraulic press at a compact pressure of 250 MPa and dwelled for 2 minutes. Discs 10 mm diameter x 6 mm height were prepared and labeled SiC-Cord. A similar protocol was used to prepare SiC-Spod. Control SiC discs prepared by pressing SiC particle

pretreated with NaOH without any binder were labeled SiC-Cris due to the formation of a cristobalite phase that bonded the SiC particles. All discs were dried for 3 hours at 100 ºC to remove moisture and then subjected to heat treatment in ambient in Thermolyne$^{TM}$ (Thermo Scientific, Vernon Hills, IL) muffle furnace at 600 ºC/3h followed by treatment at 1200 ºC/8 h at a rate of 5 ºC/min.

3.2.2.1. X-Ray Diffraction Analysis of phase composition

X-Ray Diffraction analysis (XRD) was used to determine the crystalline structure of each composite. A PANalytical X'Pert Pro/MRD was used for all scans. The discs were ground to a powder and adhered to a silicon zero background disk with double-sided tape. The scanning X-ray beam was Ni-filtered Cu K alpha radiation with a wavelength of 1.54 Å. Radiation was produced at 45 kV and 40 mA. Incident beam optics included a 0.76 mm divergence slit and a 0.1 mm receiving slit. Scan time per step was 0.5 sec and the 2θ range was from 5° to 100°. Indialite to Cordierite phase transformation was distinguished by the diffraction peaks at 2θ between 29º and 30º. Indialite has a plain single peak with a distortion index of Δ=0, whereas cordierite has multiple peaks with Δ>0. The calculation of the distortion index Δ was done using the Eq. (3.1) as mentioned in the literature[31]:

$$\Delta = 2\theta_D - (2\theta_A + 2\theta_B/2) \quad (3.1)$$

where,

$2\theta_A$, $2\theta_B$, and $2\theta_D$ are the deviation of distortion angles in degrees, of the peaks A, B, and D, respectively.

3.2.2.2. Density Measurements

The density of the sintered discs was measured using the Archimedes principle and by the mercury porosimetry technique. For the Archimedes method, the dry weight of the sample and the weight of the sample in the auxiliary liquid (deionized water) of all samples were measured at ambient atmospheres. The density was calculated using Eq (3.2)

$$\rho = \frac{A}{A-B}(\rho_0 - \rho_L) + \rho_L \quad (3.2)$$

where,

ρ = density of the sample,

A = weight of the sample in air,

B = weight of the sample in the auxiliary liquid,

$\rho_0$ = density of the auxiliary liquid,

$\rho_L$= density of the air (0.0012 g/cm$^3$).

The theoretical density of each composite was calculated using the rule of the mixture and the actual density of each pure phase: SiC (3.2 g/cc), cordierite 3.11 g/cc and spodumene 2.8 g/cc. For the mercury porosimetry method, the bulk and the apparent skeletal densities were computed by the Autopore V 9600 mercury porosimetry instrument. Relative to mercury porosimetry, bulk density is defined as the unit weight per unit volume of material after subtracting the pores larger than 180 μm. Skeletal density is usually computed after excluding the volume of all pores larger than 0.005 μm.

3.2.2.3. Porosity measurements

The porosity percent, pore-size distributions bulk, and apparent densities for all samples were measured by mercury porosimeter (Model Autopore V 9600, Micrometrics, Norcross,

Georgia). Moreover, the width and length of the pores on the SEM images of the fractured surface of the ceramic discs were measured using the SEM software installed in the JEOL 6480 Scanning Electron Microscope. The average pore size was determined from the analysis of six images, each with 10 pore size measurements.

3.2.2.4. Mechanical Properties

Composite discs (n=7) were compressed uniaxially using an Instron machine (Instron 5582, Norwood, MA) at a rate of 0.02 in /min until failure. The compressive strength of the thermally treated discs was calculated from the stress-strain curve.

A nano-indentator from Agilent G200, USA was used to measure the Modulus of elasticity of the SiC-mineral binder. This method uses a Berkovich diamond indenter tip with the geometry of a three-sided pyramid at a maximum load of 50 gf (490 mN) with a hold time of 10s. The mechanical properties were derived using the Oliver-Parr technique in which the hardness was measured using Eq (3.3),

$$H = \frac{P_{max}}{A_c} \tag{3.3}$$

where, H is the hardness, $P_{max}$ is the maximum load and $A_c$ represents the projected area of indentation.

The elastic modulus was calculated using Eq (3.4)

$$\frac{1}{E_m} = \frac{(1-\nu^2_s)}{E_s} + \frac{(1-\nu^2_i)}{E_i} \tag{3.4}$$

were,

$\nu_s$ = Poisson ratio of the sample

$\nu_i$ = Poisson ratio of the indenter

$E_s$= elastic modulus of the sample

$E_i$= elastic modulus of the indenter

$E_{m=}$ elastic modulus of the material

The modulus of elasticity was calculated using the extrapolation technique according to the method reported in the literature [31]. The modulus vs displacement was distinguished into three parts: i) Initial rising ii) Plateau and iii) falling off. A straight line was drawn to extrapolate the plateau region to the y-axis where the displacement equals to 0 which points to the young's modulus of the composite.

### 3.2.3. Thermal Shock Resistance and Dimensional Stability

The sintered discs were re-heated at 1200 ºC for 30 mins in Carbolite Gero (Verder Scientific, Hope Valley, England) furnace and quenched in water at room temperature following the ASTM standard for quenching (ASTM:C1525-18). The samples were dried, and dimensional stability was evaluated by measuring the change in the diameter and the height of the discs using Mitutoyo Digimatic Micrometer (Model: MDC-1" SX, 293-831-30). Moreover, the effect of the thermal shock on the crack formation was evaluated by SEM and EDX analysis. The mechanical properties were measured as described above.

#### 3.2.3.1. SEM Morphological Studies

To analyze the microstructure and the fracture surface morphology, the samples were sputter coated with gold (10 nm thickness) and analyzed by JEOL 6480 Scanning Electron Microscope-Energy Dispersive X-Ray Analysis (SEM-EDX) in a secondary electron mode at 20 kV with a working distance of 10 mm. The elemental composition of the phases and binding zones between particles was analyzed by EDX and presented as an atomic percentage.

3.2.3.2. Width of the bonding zone measurements

The widths of the bonding zone comprised of the silica layer and the mineral binder between silicon carbide particles were estimated from areal surface measurements taken using Zygo Nexview coherence scanning interferometer (CSI). CSI is an interferometric technique that estimates height maps by evaluating the changes in interference signal strength in relation to its optical coherence while scanning in the vertical direction. The instrument used was a Zygo Nexview with a 50x Mirau objective. Since the surfaces of silicon carbide were too rough, the measurements were made with CSI rough and oversampling settings. The CSI rough setting narrows the bandwidth of the light used, thus increasing the coherence length, to improve the quality of the data when measuring rough surfaces but at the cost of vertical resolution. Oversampling increases the measurement time enabling the instrument to capture weak signals which further increases the quality of the measured surface by reducing data dropouts. Surface measurements were acquired at different areas of the part surfaces. By comparing the height map with the intensity map, locations of silica gel were identified in each surface measurement. The width of silica gel was measured using 1D profile traces between the silicon carbide particles. 20 profiles were randomly chosen, and the mean and standard deviations were evaluated to characterize the width of silica gel layers between silicon carbide particles. According to the above-mentioned procedure, the width of the bonding zone for the control SiC-Cris treated with 1% NaOH was measured at both room temperature and at 1200 °C.

3.2.3.3. Statistical Analysis

All mechanical tests and density measurements were completed using n = 7 and the results are presented as mean +/- the standard deviation. One-way analysis of variance (ANOVA) was done followed by Tukey's HSD test for multiple comparisons using the statistical software SigmaPlot13 and $P < 0.05$ was considered statistically significant.

3.3. Results

3.3.1. Phase Analysis

(Figure 3.1a) demonstrates the XRD pattern for indialite used for in situ synthesis of cordierite during thermal treatment of the SiC-cordierite composite. The X-ray peaks of indialite match perfectly with PDF: 00-012-0235 and 01-082-1540. Maud rietveld analysis of the XRD spectrum of SiC-Cordierite composite showed the phase composition α-SiC (78.61 ± 0.00 %), β-cordierite (16.23 ± 0.90 %), and α-Cristobalite (5.15 ± 0.34 %). The XRD peaks in the diffraction angle range 2θ of 29º to 30º for indialite initially added to the SiC and cordierite present in the SiC-Cord composite are shown in (Figure 3.1b). Figure 3.2 shows the XRD peaks of Spodumene and the SiC-Spodumene composite. Maud rietveld analysis of the XRD shows the phase composition: α-SiC (67.56 ± 1.82 %), β-Spodumene (25.35 ± 0.0 %), and α-Cristobalite (7.08 ± 0.29 %). The phase composition of control SiC-Cris is 89.87 ± 3.11 % of α-SiC and 10.12 ± 0.27 % of α-Cristobalite. In all SiC composites, we observed the transformation of beta SiC to alpha SiC as indicated by the peaks at d spacing 2.63, 2.52, and 2.36 nm (PDF-01-075-8314) (Figure 3.3). In addition, the initial silica gel layer on SiC particles were transformed into alpha cristobalite with characteristic peaks at d spacing 0.4062 nm (PDF- 04-008-7639). The

characteristic peaks for Cordierite, Spodumene, and Cristobalite in the SiC composites showed a slight shift in the d spacing indicating a solid solution. For the SiC-Cord composite, the d-spacing for the (110) plane of cordierite was shifted from 0.847 nm (PDF- 01-076-6035) to 0.8505 nm. On the other hand, the d-spacing for the (111) plane of spodumene in the SiC-Spod composite was shifted to a lower value from 0.46 nm (PDF- 00-035-0797) to 0.45 nm. The main peak for alpha cristobalite did not show any measurable shifts.

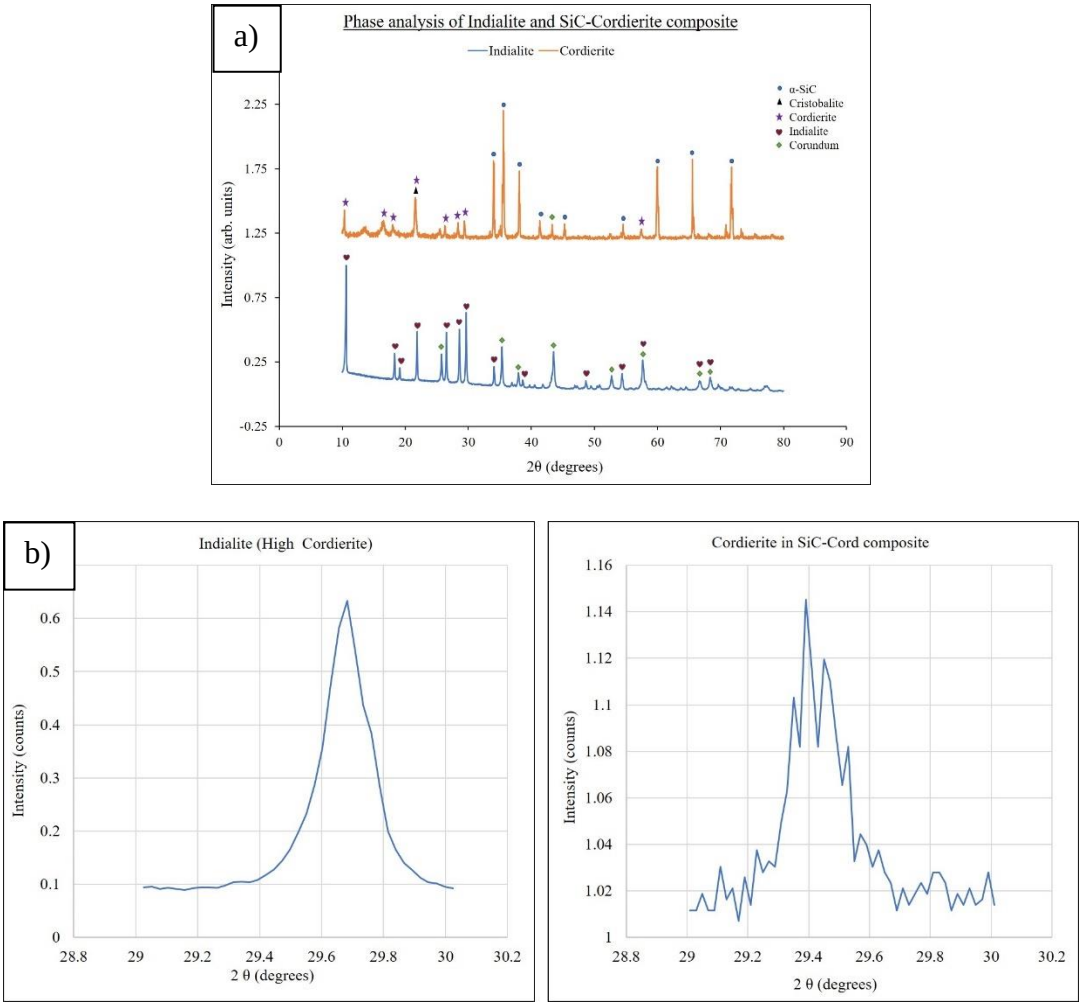


FIGURE 3.1: (a) XRD phase analysis of Cordierite starting material showing Indialite phase and Cordierite in SiC-Cord composite. (b) Peak differences between 29º and 30º of 2θ from XRD analysis, for Indialite obtained from cordierite starting material (left), Cordierite formed in SiC/Cordierite composite (right).

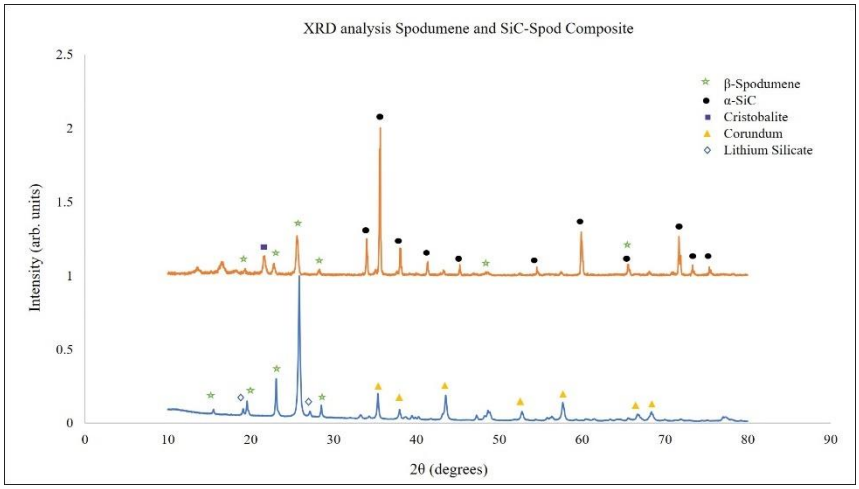


FIGURE 3.2: XRD phase analysis of Spodumene starting material SiC-Spod composite showing phases of β-Spodumene, corundum, Lithium silicate, and α-SiC.

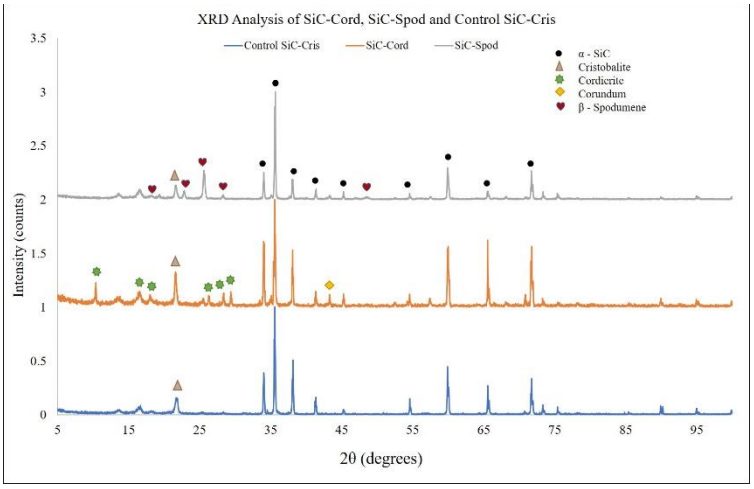


FIGURE 3.3: XRD phase analysis of SiC sample treated with Cordierite binders, spodumene binders, and control SiC (w/o binders). The phase analysis shows the presence of α-SiC, β-Spodumene, cordierite, and cristobalite phases.

### 3.3.2. Porosity measurements

Mercury porosimetry showed the porosity percent increases in the order control SiC-Cris (35.66%) > SiC-Cord (26.92%) > SiC-Spod (25.41 %). The average pore diameter of control SiC-Cris, SiC-Cord, and SiC-Spod are 2.6, 1.01 and 0.30 µm, respectively. SEM porosity analyses (Figure 3.4) showed a significant drop in the percent of large pores (15-20 µm and 10-

15 µm) and a significant increase in the percent of small pores (1-5 µm) after the addition of Cordierite or Spodumene. control SiC-Cris discs showed 62% of the pores fall in the range of 10-20 µm while the percentage dropped to 33% and 13% for the same pore size range for SiC-Cord and SiC-Spod, respectively. Moreover, the percentages of pores in the size range 1-5 µm were 8%, 29%, and 57 % for control SiC-Cris, SiC-Cord, and SiC-Spod, respectively.

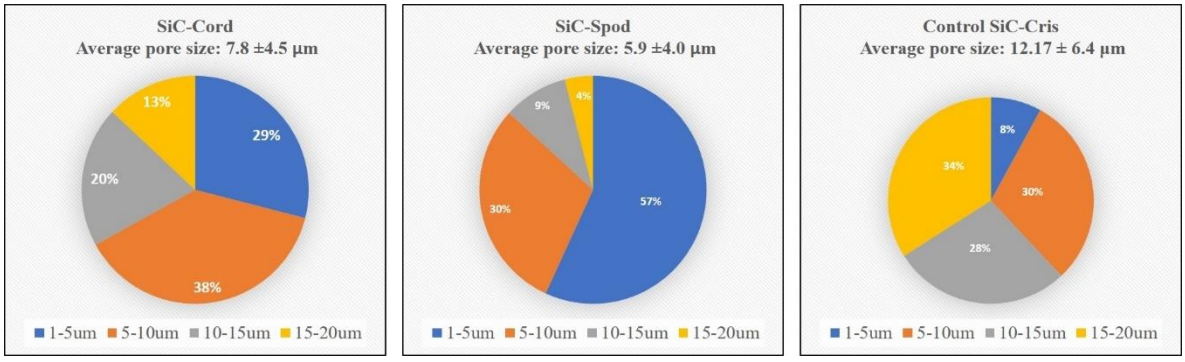


FIGURE 3.4: Modal distribution of pore sizes ranging from 1 µm to 20 µm: (from left to right) SiC-Cord composite, SiC-Spod composite, and control SiC-Cris without binders.

3.3.3. Density

TABLE 3.1: Theoretical and Experimental density data comparison of the composites

| Composite type | Theoretical Composite density calculated using the rule of mixtures (g/cc) | Experimental apparent density measurements using Archimedes (g/cc) |
|---|---|---|
| SiC-Cord | 3.18 | 2.74 ± 0.05 |
| SiC-Spod | 3.12 | 2.61 ± 0.11 |
| Control SiC-Cris | 3.2 | 2.74 ± 0.08 |

Table 3.1 lists the density of SiC composites measured using the Archimedes principle in comparison to the theoretical calculations based on the role of mixtures. The apparent density for

SiC-Cord, SiC-Spod, and control SiC-Cris was 86.2%, 83.5%, and 85.6% of the theoretical density. Statistical analysis showed no significant difference in the density between the groups SiC-Cord and control SiC-Cris and SiC-Spod and control SiC-Cris. On the other hand, the density of the SiC-Spod was significantly lower than that of SiC-Cord ($P < 0.03$).

### 3.3.4. Mechanical Properties

The average compressive strength significantly increased in the order SiC-Cord > SiC-Spod > control SiC-Cris (Figure 3.5). The average compressive strength of SiC-Cord was three times higher than control SiC-Cris ($p < 9.7 \times 10^{-7}$) and two times higher than that of SiC-Spod ($p < 0.003$). Moreover, the average compressive strength of the SiC-Spod was significantly higher than that of control SiC-Cris ($p < 9.8 \times 10^{-7}$). The elastic modulus obtained from the nano-indentation data measured 449.42 ± 29.52 GPa and 105.03 ± 16.08 GPa for SiC and Cordierite components; respectively in the SiC-Cordierite composite. For the SiC-Spodumene composite the modulus of elasticity for the SiC component measured 404.74 ± 68.98 GPa and that of spodumene measured 86.25 ± 33.29 GPa. Calculation of the moduli of elasticity of the composites based on the elasticity of the components using the rule of mixtures showed 380.54 ± 9.12 GPa for SiC-Cord and 341.04 ± 61.84 GPa for SiC-Spod.

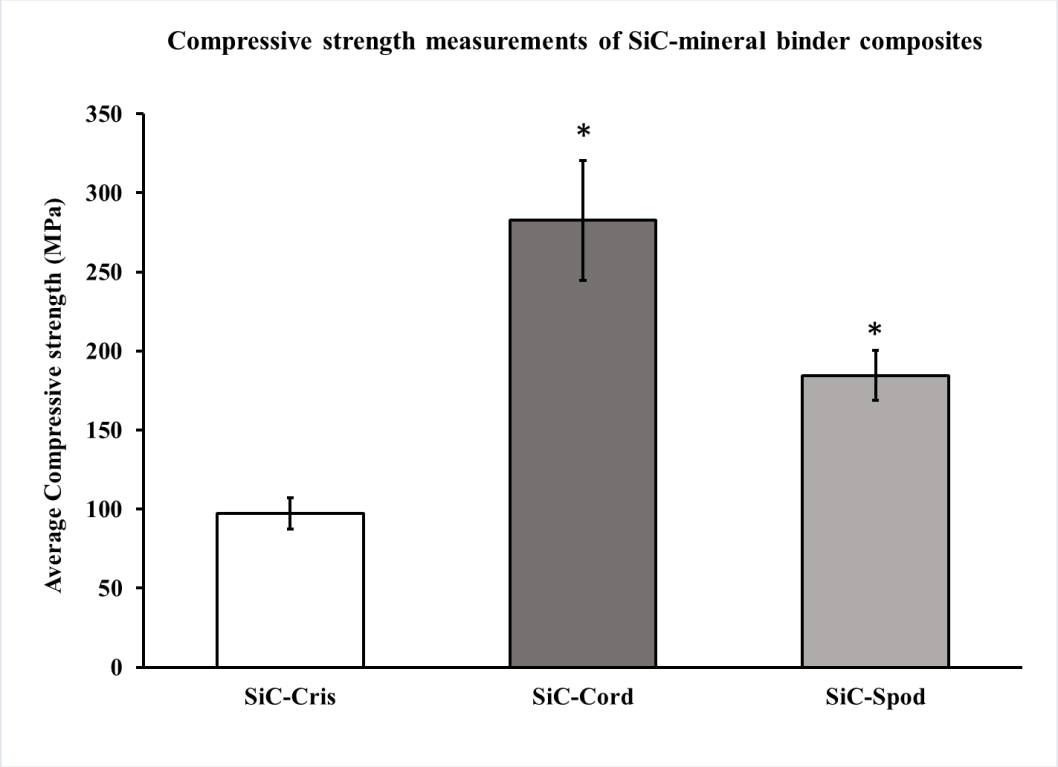


FIGURE 3.5: Average compressive strength of SiC-Cord, SiC-Spod, and control SiC-Cris discs after thermal treatment at 1200 ºC. The mechanical strength increased in the order SiC-Cord > SiC-Spod > Control SiC-Cris.

3.3.5. SEM Fracture Surface Analysis

SEM analyses of the fracture surface of control SiC demonstrated that failure occurs by trans-granular as well as intergranular mechanisms (Figures 3.6a and 3.6b). Figure 3.6a shows a 15-micron-long crack propagating from the surface through the thickness of the SiC particle. The arrows in Figure 3.6b point at cracks within the cristobalite bonding zone between SiC particles. EDX analysis of the fractured surface showed the composition of the silica bonding zone to be oxygen deficient with a Si/O atomic ratio of 1/1.8. Minimal cleavage marks were seen on the SiC fracture surface.

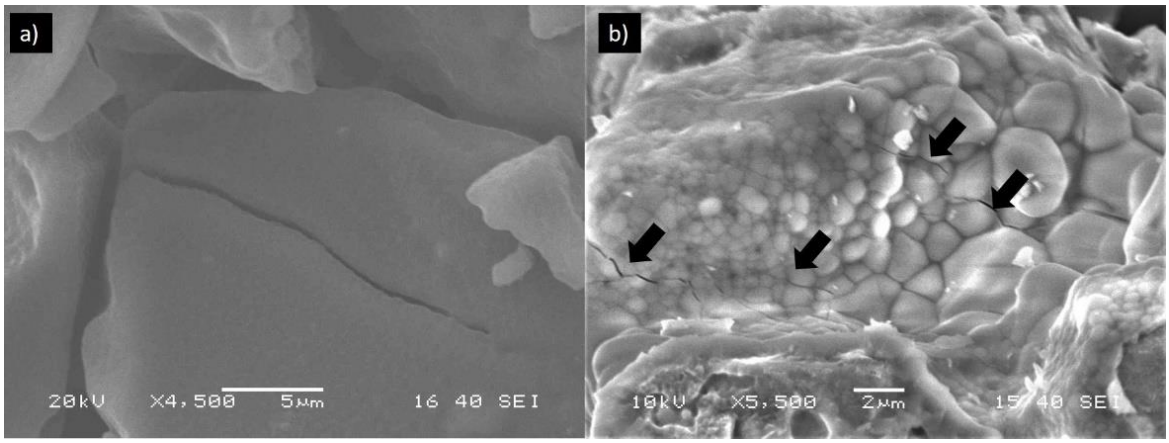


FIGURE 3.6: a) and b) shows trans-granular and intergranular fractures that occurred after compression, c) shows the silicon oxide layer on the surface of SiC with multiple cracks in the control SiC-Cris sample.

Analysis of the fracture surface of SiC-Cord and SiC-Spod showed a trans-granular failure mechanism through the SiC phase. Figures 3.7a and 3.7b demonstrate complete fracture of SiC particles in the SiC-Cord and SiC-Spod, respectively. It is noteworthy that the Cord and Spod bonding zones had an intact interface with the SiC particles and were crack-free (Figures 3.7c and 3.7d). It is important to note that extensive cleavage marks were present on the fracture surface of SiC particles in SiC-Cord and SiC-Spod compared to that of SiC-Cris. Moreover, the Cord or Spod components in the composites did not show cleavage marks.

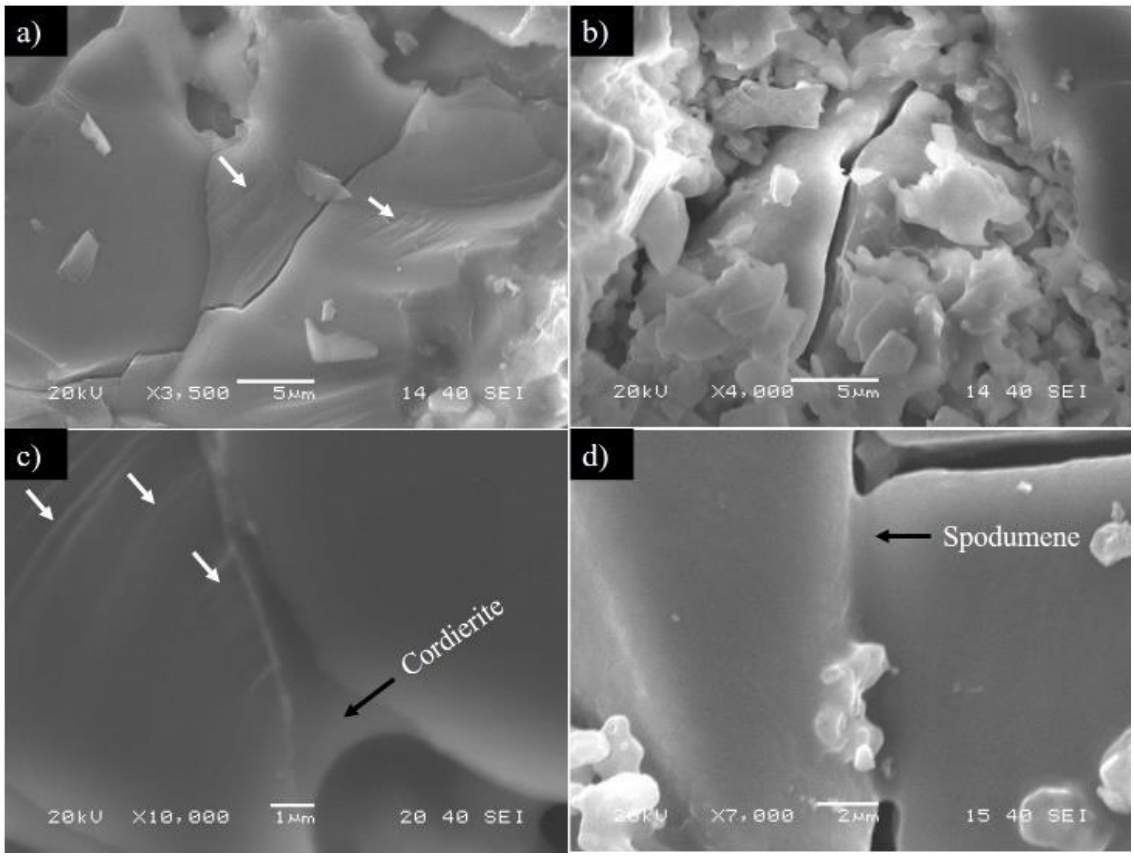


FIGURE 3.7: The white arrows in a) and c) shows the cleavage marks and the complete fracture of SiC-Cord, b) shows a huge trans-granular crack after fracturing in SiC-Spod, c) SEM image of the fractured SiC-Cord, d) SEM image of the fractured SiC-Spod.

EDX analysis of the bonding zone in Figure 3.7c showed the composition in an atomic percent: 3.28 % Mg, 7.17 % Al, 29.76 % Si, 50.78% O, and 8.83 % C, indicating $Mg_2Al_4Si_5O_{18}$. Since the EDX beam is larger than the size of the SiC particle, a small amount of SiC can also be seen in the background. The composition percent of each element is less than the actual percentage of $Mg_2Al_4Si_5O_{18}$ which is caused by the replacement of $Al^{3+}$ by $Si^{4+}$ which was reported to improve the thermal shock resistance[32]. EDX of the bonding zone in Figure 3.7d shows the presence of O, Si, and Al in atomic percentages 63.46 %, 26.49 %, and 10.05 %, respectively indicating $LiAlSi_2O_6$ and $SiO_2$. Since lithium has a very low atomic weight, its presence cannot be captured using EDX. EDX analysis of the bonding zone of SiC-Cord in Figure 3.12 is shown in table 2

below. A compositional change in the atomic percent of Al can be observed when moving from the bonding zone to the edge of the SiC particle and at the SiC particle. This serves as evidence for the migration of Al ions into the silica gel layer.

TABLE 3.2: EDX atomic percent of Al diffused from Cord into the $SiO_2$ layer after heat treatment at 1200 °C/8hrs

| Composite | Compound | Element | Positions | Distance (μm) | Atomic percentage (%) |
|---|---|---|---|---|---|
| SiC-Cord | $Mg_2Al_4Si_5O_{18}$ | Al | 1 | 0.00 | 5.5 |
| | | | 2 | 3.29 | 1.5 |
| | | | 3 | 3.67 | 0.27 |
| | | | 4 | 5.86 | 0.16 |

3.3.6. Bonding zone width measurements

The box-whisker plot of the average width of the bonding zone between the components of the control SiC-Cris, SiC-Cord, and SiC-Spod is shown in Figure 3.8. The average width of the bonding zone of control SiC-Cris > SiC-Cord and SiC-Spod. Statistical analysis shows that the width of the bonding zone of control SiC is significantly higher than that of SiC-Spod ($p < 0.04$) and SiC-Cord ($p < 0.03$), respectively. A comparable value of the average bonding zone was observed for SiC-Cord and SiC-Spod. The bonding zone width measurements for control SiC-Cris at room temperature measured 2.07 ± 0.79 μm while at 1200 °C it measured 3.07 ± 1.24 μm.

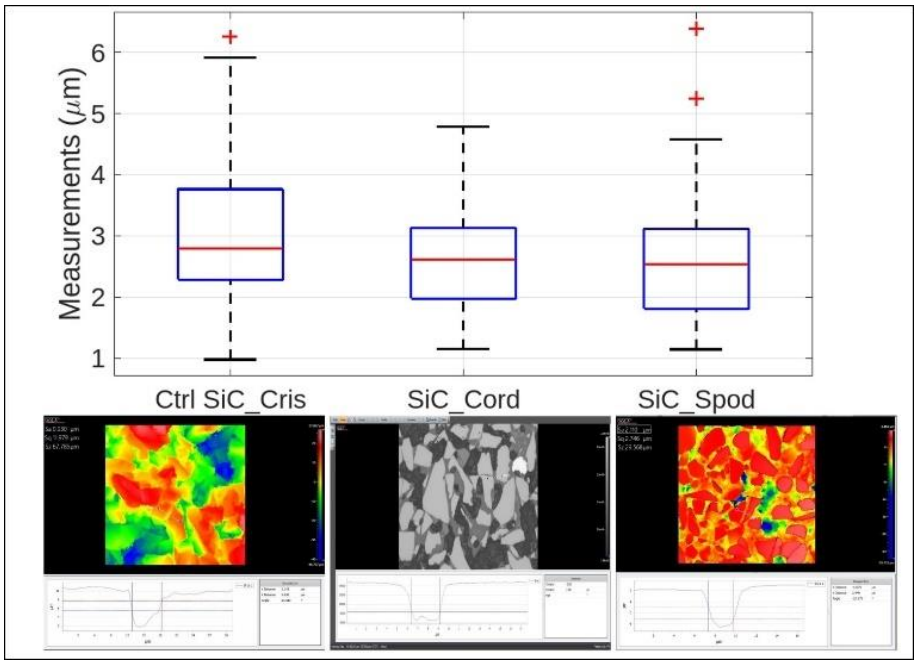


FIGURE 3.8: The box-whisker plot of the average width of the bonding zone between the components of the control SiC-Cris, SiC-Cord, and SiC-Spod.

3.3.7. Thermal shock studies

Figures 3.9 to 3.11 shows the average compression strength, and strain to failure of the samples after quenching from 1200 ºC to 25 ºC in water. Statistical analysis showed the difference in strength was not significant among all samples before and after thermal shock.

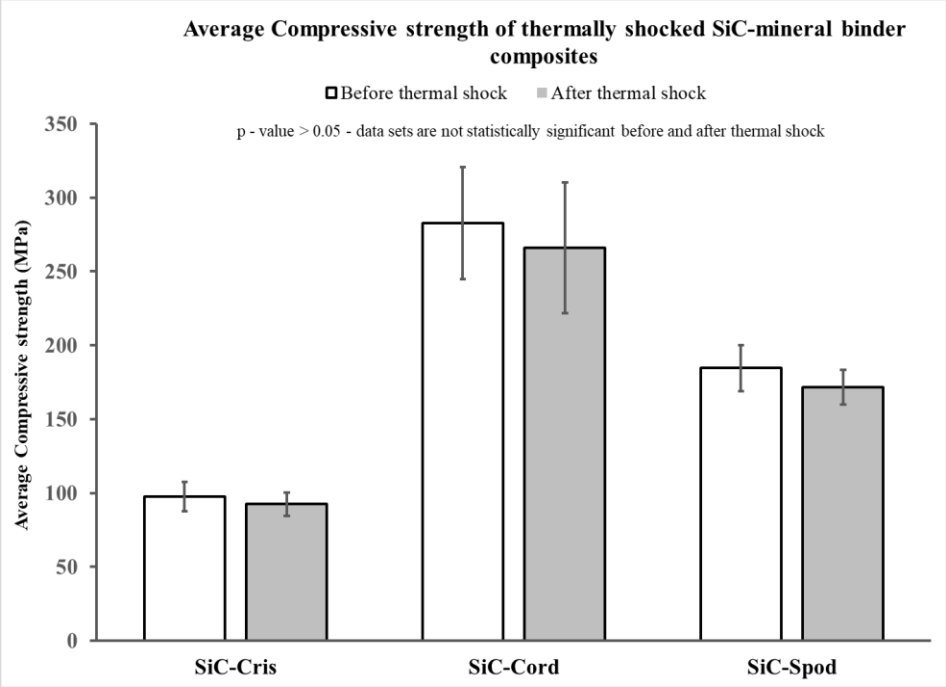


FIGURE 3.9: shows the average compressive strength and its standard deviation for samples before and after quenching of samples from 1200 ºC.

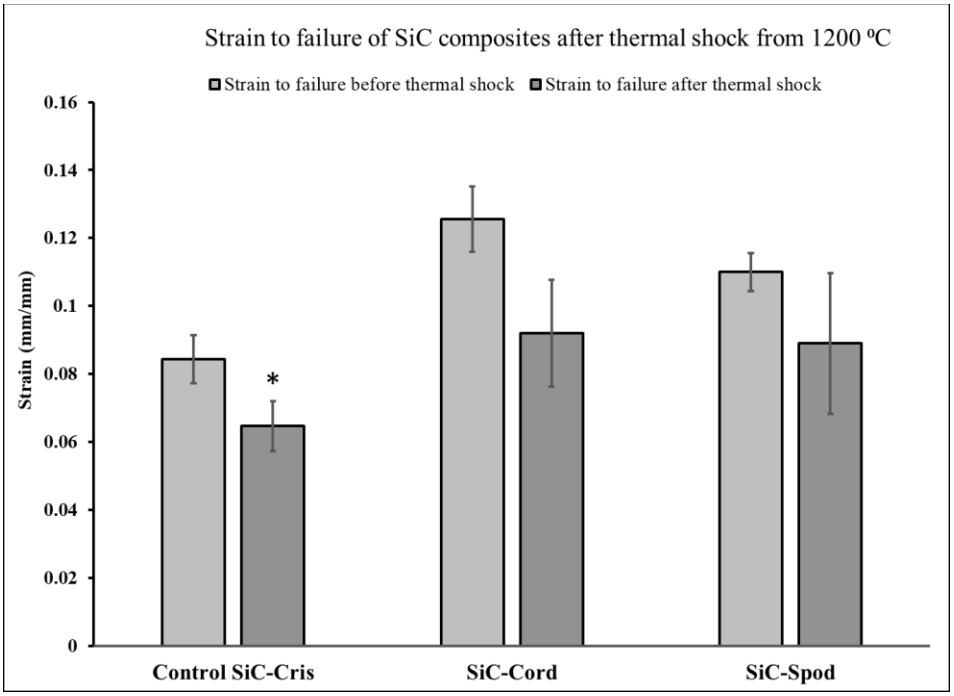


FIGURE 3.10: Strain to failure measured from the stress-strain curve obtained from SiC-Cord, SiC-Spod, and Control SiC-Cris samples after quenching of samples from 1200 ºC.

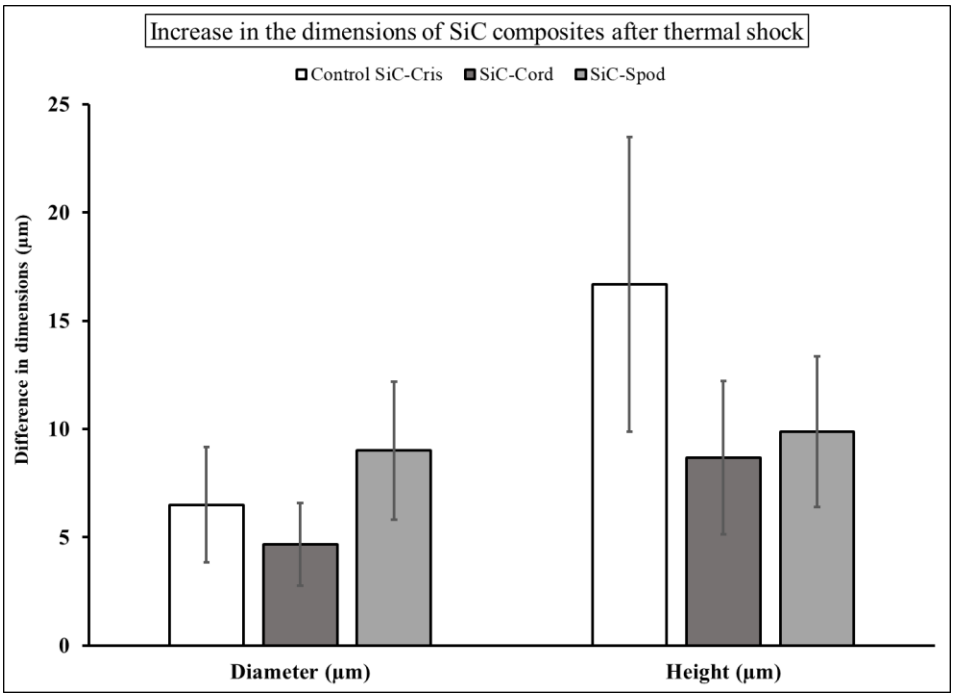


FIGURE 3.11: Dimension stability of SiC composite samples before and after thermal shock.

Although all discs were prepared using 1000 mg of powder and pressed and heated under the same conditions, we observed a lower height (0.5 mm) of the SiC-Cord and SiC-Spod composites compared to SiC-Cris which indicates more dense composite samples than the control. The increased density could be attributed to the lower porosity percent and small pore size in the composite samples.

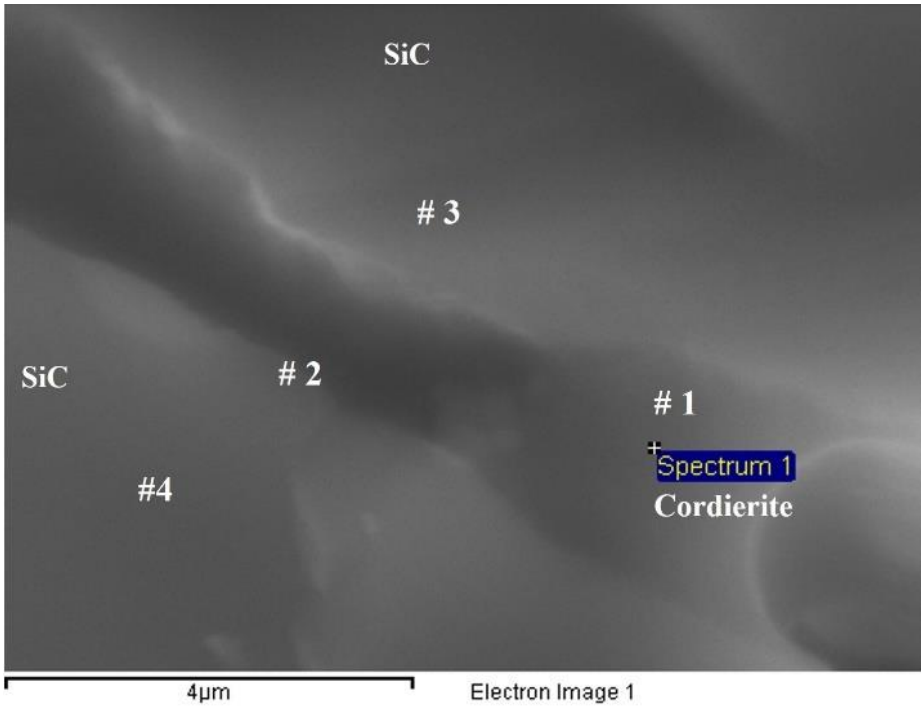


FIGURE 3.12: SEM-EDX micrograph showing variation in Al content due to the ionic migration of $Al^{3+}$ and $Si^{4+}$ between SiC and the interface.

3.4. Discussion

The results of our studies demonstrated that alumino-silicate minerals are superior binders for SiC when compared to silicon oxide binders that form by thermal oxidation. The creation of a thin active silica gel layer by chemical treatment of SiC mediated a strong interfacial bond with cordierite and spodumene. The compression strength for SiC-Cord and SiC-Spod were 282.57 ± 37.94 and 184.58 ± 15.64 MPa respectively which were higher than the 97.45 ± 9.86 MPa measured for control SiC-cristobalite. The high mechanical strength of SiC-Cord and SiC-Spod is attributed to (i) reduced porosity and pore size due to the filling of the interspace between SiC particles with the mineral binders, (ii) the strong SiC/mineral interfacial bond, (iii) the extensive ionic diffusion that created gradient compositional change at the grain boundaries and (iv) the formation of a solid solution of binder phases. On the other hand, the low

mechanical strength for control SiC-Cris is related to the large pore size, high porosity percent, and the limited contact area between the particles through the thin silica phase. Fracture surface analysis showed while control SiC-Crist fails by mainly intergranular mechanism, SiC-Cord, and SiC-Spod failed by trans-granular mechanism. In association with the strong bonding between particles, high thermal shock resistance was observed as indicated by the dimensional and mechanical stabilities of the SiC-mineral composites upon quenching from 1200 ºC to 25 ºC. The high thermomechanical and dimensional stabilities of the SiC-Cord and SiC-Spod can be attributed to the near-zero thermal expansion of the binder phases and the strong interfacial bond. Thus, the in-situ reaction between the silica layer on the SiC particles and the mineral binders created a bonding zone with transitional ionic concentration and structure that facilitated the transfer of the mechanical and thermal energies.

SEM-EDX analyses showed that the cord and Spod bonding regions were crack free which speaks for the strength of the interfacial bond between the silica layer on the SiC and Cord or Spod binders. The strength of the interfacial bond is further enhanced through the extensive ionic substitution that takes place at the interface between the surface silica and the Cord or Spod binders. The ionic traffic at the interface between the indialite and the silica layer on SiC played an important role in phase transformation and strengthening the interfacial bond. X-ray peaks of (Figure 3.1) showed the transformation of Indialite to cordierite in the SiC-Cord composite material. Data in the literature showed that indialite transforms into cordierite at 1400 °C. In our study, the indialite transformation to cordierite took place at 1200 °C, most probably due to ionic diffusion of cations (Na, Mg) and anions ($Al^{3+}$) during sintering. Data in the literature showed that $Na^{+}$ ions can be incorporated into the central channels of the oxygen rings of cordierite structures [33]. The incorporation of Na ions introduces an extra positive charge to the cordierite

crystal. One way to balance the charge is by the diffusion of $Al^{3+}$ ions into the silica layer on SiC for every three $Na^{+}$ ions incorporated in cordierite. The Al diffusion to the silica layer is further enhanced by the relatively random distribution of Al and Si ions within the indialite crystal [34]. The presence of mobile Na ions and their diffusion into cordierite and spodumene during heat treatment is also responsible for the shifts in the d-spacing of the (110) of cordierite and the (111) plane of spodumene.

The higher mechanical strength of SiC-Cord compared to SiC-Spod could be attributed to differences in (i) porosity characteristics, (ii) the extent of liquid phase sintering (iii) the inherent mechanical strength of each pure phase, and (iv) the strain energy created during thermal treatment due to differences in the thermal expansion of the components. Porosity measurements showed a significant difference in the pore size distribution between SiC-Cord and SiC-Spod (Figure 3.4). The low porosity percent and small pore size in SiC-Spod is attributed to the enhanced liquid phase formation of spodumene as indicated by SEM analysis. Other studies in the literature have reported that the addition of 20% β-spodumene facilitated the densification of mullite ceramic through a liquid phase sintering mechanism at 1423 ºC [24]. The mechanical strength and fracture energy of pure cordierite is (250 MPa and 17.2 $J/m^2$, respectively which are greater than that of β-spodumene (150 MPa and 3.7 $J/m^2$, respectively) [35]. Therefore, although SiC-Spod has a smaller pore size and lower porosity percent compared to SiC-Cord the mechanical strength of the latter composite was higher indicating the dominating role of the inherent strength. The residual stresses and strain energy due to the mismatch of the expansion coefficient as well as due to the ionic diffusion synergistically contributed to the high mechanical strength of the SiC-Cord compared to SiC-Spod or control SiC-Cris. Control SiC-Cris discs acquired large pores and higher porosity percent (Figure 3.4). In a previous study we reported on

the growth of silica nanowires at 800 - 1000 ºC in porous SiC pretreated with 20% NaOH [26]. The silica nanowires bridged the pore walls, densified, and strengthened the material. In the present study, we did not observe the formation of the nanowires due to the lower concentration of NaOH (1 weight %) which resulted in a limited formation of a silica gel layer of the SiC particles. The limited interfacial bond and absence of nanowires enhanced the fracture of control SiC-Crist via the intergranular mechanism. For the same reasons, the fractured samples of the control SiC fall apart as loose particles after the mechanical test. SEM analysis suggested that the crack initiation starts at the silica layer and propagates to the SiC (Figure 3.6b).

The high modulus of SiC-Cord is explained by (i) the high inherent toughness of cordierite (ii) the strong interfacial bond at the interface between Cord and Silica layer, $Al^{3+}$ diffuses into the Silica layer to take a vacancy of $Si^{4+}$ ion as indicated by the concentration gradient detect by SEM_EDX (Figure 3.12). On the cordierite side, three oxygen vacancies may be created for every two $Al^{3+}$ ions moving out. Mg ions on the other hand are not motivated to diffuse from cordierite to silica due to oxygen deficiency in the silica layer.

From the width measurements of the bonding zone (Figure 3.8), it can be observed that the average width of the bonding zone in control SiC-Cris is larger than that of SiC-Cord and SiC-Spod. The reduced width of the bonding zone in SiC-mineral composites is attributed to the ionic diffusion from the mineral to the cristobalite layer on SiC particles.

In SiC-Spod, the strength is enhanced due to the reduction of the thermal expansion coefficient during heat treatment by the solid solution of β-Spodumene [24]. In SiC-Spod samples reported by Wu.et.al., [35] the densification is explained by the low viscosity of liquid phases due to the strong polarizing ability of $Li^{+}$ and $Na^{+}$. It has to be noted that at 15% addition of spodumene

resulted in excessive low viscosity liquid phases that created large pores of a diameter of 50 – 200 μm which reduced the bending strength of the sample significantly.

SEM morphology analysis (Figures 3.7a and 3.7b) shows cleavage marks on the SiC particles which are representative of crack deflection [37]. Crack deflection marks are due to the differences in the coefficient of thermal expansion between SiC and the mineral binders. The low thermal expansion of the Spod and cord will induce strain energy in SiC that results in transgranular fracture and cleavage formations.

XRD analysis of control SiC sintered at 1200 ºC showed the transformation of β-SiC to α-SiC. Previous work has investigated the effect on the β to α SiC transformation temperature of the processing parameters including applied pressure [43-46], starting powder polytype composition [42-44], sintering aids [45-50], and sintering atmosphere [51-55]. Parish et.al. reported the formation of α SiC at 1440 ºC upon exposure of β SiC to neutron irradiation [51]. Hot isostatic pressure transformed β to α at a temperature greater than 2000 ºC [58]. Other studies showed that the β-SiC to α-SiC phase transformation is influenced by the liquid phase sintering of the additives and took place at a temperature (>1900 ºC) [56,57]. In our study, the SiC powder used to make the discs is made of a mixture of 40% of α-SiC, 10% amorphous SiC, and 50% β-SiC. The presence of a high percentage of the α phase in the initial material serves as an enhancer for the complete transformation of the β to α phase [58]. Moreover, the presence of labile Na ions is expected to catalyze the β to α transformation. This is in agreement with previous studies that showed an enhancing effect of boron and carbon on β to α transformation [59].

Indialite and Cordierite are both minerals of the beryl group with the chemical composition of $Mg_2Al_4Si_5O_{18}$. However, Indialite has a hexagonal structure and Cordierite has an orthorhombic structure. Cordierite and Indialite form similar diffraction peaks except at the 2θ between 29º and

30º which is distinct. Indialite has a plain single peak with Δ=0, whereas cordierite has multiple peaks with Δ>0. The difference in these peaks was discussed in detail in the work of Akiho Miyashiro [30]. Figure 3.1b shows the peak differences between 29º and 30º of 2θ for Indialite obtained from cordierite starting material and cordierite formed in SiC/Cordierite composite. Data in the literature indicated that $K_2O$ is required to facilitate the synthesis of dense cordierite. However, the alkali oxides increase the expansion coefficient and lower the mechanical properties [59]. In our study, this challenge has been overcome by creating the Indialite phase and transforming it to cordierite in the preparation of SiC/Cordierite composite.

In addition to that, the sintering technique of the SiC composite was done at a low temperature involving a novel method of creation of a silica gel layer at room temperature which later crystallizes to cristobalite $SiO_2$. This reduces the overall manufacturing cost of this SiC composite which possesses high strength and density along with excellent mechanical and thermal properties. The minimal differences in densities can be attributed to the differences in the porosity characteristics and the phase composition. On the other hand, for control SiC, the NaOH treatment of SiC created a silica gel layer that served as a precursor for cristobalite formation [26-29]. As such, the preexisted silica gel layer rather than the thermal oxidation of SiC is responsible for the formation of cristobalite in all samples at relatively low temperatures. The cristobalite XRD signal was shifted indicating the formation of a solid solution phase. While measurements of the compressive strength showed comparable values for each composite before and after thermal shock, a significant difference in the strain to failure was observed for all samples. This is due to the residual thermal stresses stored in the samples owing to the differences in thermal expansion coefficients among different phases. Owing to the large difference between the thermal expansion coefficient of SiC and Cristobalite the strain to failure

of control SiC-Crist was significantly ($P < 0.02$) lower than that of SiC-Cord and SiC Spod. SEM-EDX analysis (Figure 3.13) of the fracture surface of the quenched samples demonstrated crack sealing most probably due to the capillary action of the liquid mineral phases that flow in the open space created by the cracks.

## 3.5. Conclusion

In this work, a novel sintering technique was introduced by incorporating mineral binders as a bonding material to densify and strengthen SiC particles. Cordierite and Spodumene were carefully chosen as the mineral binders for the SiC mineral binder composites due to their excellent inherent thermo-mechanical properties. SiC-Cord and SiC-Spod composites showed high compressive strength and modulus compared to the control SiC-Cris. Strengthening was seen to increase due to the lattice distortion of the binder phase caused by the mismatch of the thermal coefficient of expansion of the binder phase and the SiC particles. The ionic diffusion of $Al^{3+}$ into the silica layer at the interface with the mineral binder enhanced the adhesion between SiC particles. The liquid phase transformation of the binders facilitated particle fusion and reduced the porosity percentage and the pores size. Strain to failure was significant in all the SiC-mineral binder composites after quenching in water from 1200 ºC due to the crack sealing caused by the liquid mineral phases. Results of the study suggest that the SiC-mineral binder composites can be used as thermal materials, and catalytic converters in automobile exhaust systems, gas filters, and in combustion engines.

# REFERENCES


1. Y. V. Milman, S. I. Chugunova and I. I. Timofeeva, 'The Resistance of Silicon Carbide to Static and Impact Local Loading,' Int. J. Impact Eng., 26 [1-10] 533-542 (2001).

2. Popper, P. "Special ceramics, The Preparation of Dense Self-Bonded Silicon Carbide Bodies." London: Heywood (1960).

3. Magnani G, Brentari A, Burresi E, et al. Pressureless sintered silicon carbide with enhanced mechanical properties obtained by the two-step sintering method. Ceram Int. 2014;40(1):1759–1763.

4. Yan, C., Lifeng, W., & Jianyue, R. (2008). Multi-functional SiC/Al composites for aerospace applications. Chinese Journal of Aeronautics, 21(6), 578-584.

5. Robichaud, J., Guregian, J. J., & Schwalm, M. (2003, November). SiC optics for Earth observing applications. In Earth Observing Systems VIII (Vol. 5151, pp. 53-62). International Society for Optics and Photonics.

6. Tobin, E., Magida, M. B., Kishner, S. J., & Krim, M. H. (1995, October). Design, fabrication, and test of a meter-class reaction bonded SiC mirror blank. In Silicon Carbide Materials for Optics and Precision Structures (Vol. 2543, pp. 12-21). International Society for Optics and Photonics.

7. Johnson, J. S., Grobsky, K. D., & Bray, D. (2002, September). Rapid fabrication of lightweight silicon-carbide mirrors. In Optomechanical Design and Engineering 2002 (Vol. 4771, pp. 243-253). International Society for Optics and Photonics.

8. Wilhelm, M., Kornfeld, M., & Wruss, W. (1999). Development of SiC–Si composites with fine-grained SiC microstructures. Journal of the European Ceramic Society, 19(12), 2155-2163.

9. Amirthan, G., & Balasubramanian, M. (2011). Thermal conductivity studies on Si/SiC ceramic composites. Ceramics International, 37(1), 423-426.

10. Foster, D., & Thompson, D. P. (1999). The use of MgO as a densification aid for α-SiC. Journal of the European Ceramic Society, 19(16), 2823-2831.

11. Sciti, D., & Bellosi, A. (2000). Effects of additives on densification, microstructure, and properties of liquid-phase sintered silicon carbide. Journal of materials science, 35(15), 3849-3855.

12. Liu S, Zeng Y-P, Jiang D (2009) Effects of $CeO_2$ addition on the properties of cordierite-bonded porous SiC ceramics. J Eur Ceram Soc 29:1795–1802.

13. Nagano, T., Gu, H., Kaneko, K., Zhan, G. D., & Mitomo, M., Effect of dynamic microstructural change on deformation behavior in liquid-phase-sintered silicon carbide with $Al_2O_3$-$Y_2O_3$-CaO additions. J. Am. Ceram. Soc., 2001, 84, 2045-2050.

14. Alireza Moradkhani, Hamidreza Baharvandi, Microstructural analysis of fracture surfaces and determination of mechanical properties of $Al_2O_3$–SiC–MgO nanocomposites, International Journal of Refractory Metals and Hard Materials, Volume 67, 2017, Pages 40-55, ISSN 0263-4368, https://doi.org/10.1016/j.ijrmhm.2017.05.004.

15. B. Riccardi, E. Trentini, M. Labanti, M. Leuchs, S. Roccella, E. Visca J. Nucl. Mater., 367–370 (2007), pp. 672-676.

16. Kim, W-J., S. M. Kang, J. Y. Park, and W-S. Ryu. "Effect of a SiC whisker formation on the densification of Tyranno SA/SiC composites fabricated by the CVI process." Fusion Engineering and design 81, no. 8-14 (2006): 931-936.

17. H. Araki, A. Kohyama, T. Noda Annu. Rep. China Inst. At. Energy, 33 (2007), pp. 141-146.

18. Wang, Pengren, Fengqi Liu, Hao Wang, Hao Li, and Yanzi Gou. "A review of third generation SiC fibers and SiCf/SiC composites." Journal of Materials Science & Technology 35, no. 12 (2019): 2743-2750.

19. K. Park, T. Vasilos, Interface and thermal shock resistance of SiC fiber/SiC composites, Scripta Materialia, Volume 39, Issue 11,1998, Pages 1593-1598, ISSN 1359-6462, https://doi.org/10.1016/S1359-6462(98)00356-X.

20. Baitalik S, Kayal N (2017) Processing and properties of cordierite-silica bonded porous SiC ceramics. Ceram Int 43:14683–14692.

21. Zhu S, Ding S, Xi H, Li Q, Wang R (2007) Preparation and characterization of SiC/cordierite composite porous ceramics. Ceram Int 33:115–118.

22. Dey, A., Kayal, N., Molla, A. R., & Chakrabarti, O. (2014). Investigation of thermal oxidation of $Al_2O_3$-coated SiC powder. Thermochimica Acta, 583, 25-31.

23. Lu Yuan-Yuan, Lu Gui-Hua, Zhou Heng-Wei, Huang Yi-Neng. Preparation and properties of spodumene/silicon carbide composite ceramic materials. Acta Physica Sinica, 2020, 69(11): 117701. doi: 10.7498/aps.69.20200232.

24. Low, I.M., Mathews, E., Garrod, T. et al. Processing of spodumene-modified mullite ceramics. Journal of Materials Science 32, 3807–3812 (1997). https://doi.org/10.1023/A:1018679808095.

25. Shi, C. G., and I. M. Low. "Use of spodumene for liquid-phase-sintering of aluminum titanate." Materials Letters 36, no. 1-4 (1998): 118-122.

26. El-Ghannam, T. Schmitz, Advanced 3D Printing of Silicon Carbide Based Optics through Amazon Crystal Growth, Application Number 62447641, Jan (2017).

27. El-Ghannam, M. Greenier, M. Johnson, I. Marriott, Synthesis and characterization of porous bioactive SiC tissue engineering scaffold, J. Biomed. Mater. Res. (2020), 10.1002/jbm.a.36973.

28. D. Beasock, T.M. Stokes, A. El-Ghannam, T. Schmitz, Effect of processing parameters on the microstructure and mechanical behavior of a silicon carbide-silica composite, Procedia Manufacturing, 34 (2019), pp. 747-753, 10.1016/j.promfg.2019.06.211.

29. Ahmed El-Ghannam, Sujithra Chandrasekaran, Farjana Sultana, Synthesis and characterization of a novel silica nanowire-reinforced SiC thermal material, Journal of Solid-State Chemistry, Volume 297, 2021, 122055, ISSN 0022-4596, https://doi.org/10.1016/j.jssc.2021.122055.

30. Akiho Miyashiro, American Journal of Science January 1957, 255 (1) 43-62; DOI: https://doi.org/10.2475/ajs.255.1.43.

31. Fischer-Cripps, Anthony C. "Critical review of analysis and interpretation of nanoindentation test data." Surface and coatings technology 200, no. 14-15 (2006): 4153-4165.

32. Khalil, N. M., & Kenawy, S. H. In-Situ Cordierite–Silicon Carbide Composite. American Ceramic Society Bulletin, 87(7).

33. Armbruster, T. (1986). Role of Na in the structure of low-cordierite; a single-crystal X-ray study. American Mineralogist, 71(5-6), 746-757.

34. D.G. Grossman, Glass-ceramics, Engineered Materials Handbook, Vol. 4 Ceramics and Glasses, ASM International, American Technical Publishers Ltd, Herts, UK (1991), pp. 170-176.

35. Jianfeng Wu, Cheng Hu, Xiaohong Xu, Yinfeng Zhang, Chenglong Lu, Dongbin Wang, Preparation and thermal shock resistance of cordierite-spodumene composite ceramics for solar heat transmission pipeline, Ceramics International, Volume 42, Issue 12, 2016, Pages 13547-13554, ISSN 0272-8842, https://doi.org/10.1016/j.ceramint.2016.05.147.

36. Hinze, J. W., and H. C. Graham. "The active oxidation of Si and SiC in the viscous gas-flow regime." Journal of the Electrochemical Society 123, no. 7 (1976): 1066.

37. Xie, R. J., Mitomo, M., Kim, W., Kim, Y. W., Zhan, G. D., & Akimune, Y., Phase transformation and texture in hot-forged or annealed liquid-phase-sintered silicon carbide ceramics. J. Am. Ceram. Soc., 2002, 85, 459-465.

38. Zhan, G. D., Mitomo, M., Tanaka, H., & Kim, Y. W., Effect of annealing conditions on microstructural development and phase transformation in silicon carbide. J. Am. Ceram. Soc., 2000, 83, 1369-1374.

39. Zhan, G., Xie, R., & Mitomo, M., Effect of β-to-α phase transformation on the microstructural development and mechanical properties of fine-grained silicon carbide ceramics. J. Am. Ceram. Soc., 2001, 84, 945-950.

40. Zhan, G., Ikuhara, Y., Mitomo, M., Xie, R., Sakuma, T., & Mukherjee, A. K., Microstructural analysis of liquid-phase-sintered β-silicon carbide. J. Am. Ceram. Soc., 2002, 85, 430-436.

41. Zhan, G., Mitomo, M., & Kim, Y., Microstructural control for strengthening of silicon carbide ceramics. J. Am. Ceram. Soc., 1999, 82, 2924-2926.

42. Tanaka, H., Hirosaki, N., Nishimura, T., Shin, D. W., & Park, S. S., Nonequiaxial grain growth and polytype transformation of sintered α-silicon carbide and β-silicon carbide. J. Am. Ceram. Soc., 2003, 86, 2222-2224.

43. Lee, C. S., Kim, Y. W., Cho, D. H., Lee, H. B., & Lim, H. J., Microstructure and mechanical properties of self-reinforced alpha-silicon carbide. Ceramics International, 1998, 24, 489-495. 12

44. Rixecker, G., Biswas, K., Rosinus, A., Sharma, A., Wiedmann, I., & Aldinger, F., Fracture properties of SiC ceramics with oxynitride additives. J. Eur. Ceram. Soc., 2002, 22, 2669-2675.

45. Lee, S., Kim, Y., & Mitomo, M., Relationship between microstructure and fracture toughness of toughened silicon carbide ceramics. J. Am. Ceram. Soc., 2001, 84, 1347-1353.

46. Zhou, Y., Hirao, K., Toriyama, M., Yamauchi, Y., & Kanzaki, S., Tailoring the mechanical properties of silicon carbide ceramics by modification of the intergranular phase chemistry and microstructure. J. Eur. Ceram. Soc., 2002, 22, 2689-2696.

47. Zhou, Y., Hirao, K., Toriyama, M., Yamauchi, Y., & Kanzaki, S., Effects of intergranular phase chemistry on the microstructure and mechanical properties of silicon carbide ceramics densified with rare-earth oxide and alumina additions. J. Am. Ceram. Soc., 2001, 84, 1642-1644.

48. Cao, J. J., Moberlychan, W. J., DeJonghe, L. C., Gilbert, C. J., & Ritchie, R. O., Insitu toughened silicon carbide with Al-B-C additions. J. Am. Ceram. Soc., 1996, 79, 461–469.

49. Zhang, X. F., Yang, Q., & DeJonghe, L. C. Microstructure development in hot-pressed silicon carbide: effects of aluminum, boron, and carbon additives. Acta Materialia, 2003, 51, 3849-3860.

50. Suzuki, K. & Sasaki, M., Effects of sintering atmosphere on grain morphology of liquid-phase-sintered SiC with Al2O3 additions. J. European Ceramic Society, 2005, 25, 1611–1618.

51. Parish, C., T. Koyanagi, S. Kondo and Y. Katoh. “Irradiation-induced β to α SiC transformation at low temperature.” Scientific Reports 7 (2017): n. pag.

52. Warren J. MoberlyChan et.al., “Cubic to hexagonal phase transformation to toughen SiC.

53. R. G. Munro, "Material Properties of a Sintered α-SiC", Journal of Physical and Chemical Reference Data 26, 1195-1203 (1997) https://doi.org/10.1063/1.556000

54. Tanaka, Hidehiko et al. “Nonequiaxial Grain Growth and Polytype Transformation of Sintered α-Silicon Carbide and β-Silicon Carbide.” Journal of the American Ceramic Society 86.12 (2003): 2222–2224.

55. Kyeong-Sik, Cho. "Effect of alpha-SiC seed on microstructure and fracture toughness of pressureless-sintered beta-SiC". Journal of the Korean Crystal Growth and Crystal Technology 7, no. 1 (1997): 18-26.

56. Lancin, M., Anxionnaz, F., Thibault-Desseaux, J. et al. β → α Phase transformation in sintered SiC involving feather formation. J Mater Sci 22, 1150–1156 (1987). https://doi.org/10.1007/BF01233103

57. Jacobson, N.S., Myers, D.L. Active Oxidation of SiC. Oxid Met 75, 1–25 (2011). https://doi.org/10.1007/s11085-010-9216-4.

58. Roy, J and Chandra, S and Das, S and Maitra, S, Oxidation behavior of silicon carbide-a review, Reviews on advanced materials science, volume 38, 2014, pages 29-39.

59. Daniels, P. (1992). Structural effects of the incorporation of large-radius alkalis in high cordierite. American Mineralogist, 77(3-4), 407-411.

60. Putnis, A. (1980). The distortion index in anhydrous Mg-cordierite. Contributions to Mineralogy and Petrology, 74(2), 135-141.

# CHAPTER 4: (PAPER 3) SiC-MINERAL BINDER COMPOSITE FOR SPACE MIRROR AND THERMAL APPLICATIONS

Authors:

Sujithra Chandrasekaran, Ahmed El-Ghannam, James A. Monroe

## 4.1. INTRODUCTION

Large primary mirrors and mirror substrates that exhibit low density, high specific stiffness, and thermal stability are essential for astronomical and earth science observations. Space mirrors are used to study solar radiation management including crop engineering and energy storage [1,2]. Lightweight mirrors are desirable to decrease costs. Beryllium and SiC mirrors are an order of magnitude higher in cost compared to ULE, Zerodur, and Cordierite mirrors. Moreover, beryllium releases toxic gases and the fabrication of SiC possesses a high cost [3]. To decrease the weight of the mirrors, they are often made as a honeycomb structure and multi-hole structure by drilling holes and gluing plates which can cause damage to the mirror material [4]. Therefore, lightweight and stiff mirror materials are necessary. The most widely used material for mirrors are glass ceramics due to their excellent polishing capabilities and ease of manufacturing. However, glass ceramics have relatively poor thermo-mechanical stability and are heavyweight [5,6,7]. Search for alternative lightweight thermal materials included testing Cordierite ($Mg_2Al_4Si_5O_{18}$) and Spodumene ($LiAlSi_2O_6$) for mirror applications. Cordierite and Spodumene are rock-forming minerals characterized by low thermal expansion coefficient, high thermal shock resistance, and good mechanical and thermal stabilities. However, manufacturing of pure cordierite bodies is challenged by the need to add a sintering aid to obtain a fully dense

material. The sintering aids lower thermomechanical strength and fracture toughness [8], resulting in poor thermal performance and low strength of the glass-ceramics. For these reasons, glass ceramics such as Ultra Low Expansion glass (ULE®) by Corning, USA, CLEARCERAM™-Z from Ohara, Japan, and Zerodur® by Schott, Germany, were eliminated as candidates for mirror materials [9].

SiC is characterized by excellent mechanical and thermal properties including high stiffness, thermal shock resistance, high thermal conductivity, and low thermal expansion which are essential for many aerospace applications including mirrors for telescopes [10,11,12,13]. However, manufacturing a dense SiC is costly and time-consuming due to the extreme compact pressures and elevated temperatures required for processing. Hot isostatic pressing of SiC particles at elevated temperatures (>2000 ºC) [13,14] and a pressure of 1000-2000 atm with and without sintering aids has been used to produce dense SiC [15,16,17]. The densification of SiC relied on the oxidation mechanism where a silicon oxide surface layer forms in air at high temperatures and bonds the SiC particles together. However, bonding by thermal oxidation results in a porous SiC construct that requires further processing steps to densify and strengthen the material [18]. Filling porous SiC with molten silicon (Si) or aluminum (Al) metal has been used to successfully densify the material [11,19]. However, the use of Si or Al is problematic due to the lack of a stable interface between SiC and these filling materials. The infusion of Si through the porous structure maximize the density up to 99% of the theoretical density which makes the composite suitable for many applications [20]. Nevertheless, the SiC-Si composite exhibits many limitations including: low mechanical strength due to abnormal growth of SiC particles at the interface between Si and SiC, aggregation of SiC particles due to the release of CO and SiO gases during processing [20], and low thermal conductivity due to the formation of

a glassy carbon layer between Si and the SiC [21]. In addition, the relatively low melting point of silicon (1410 ºC) limits the use of SiC-Si at high temperatures.

Trial to enhance densify SiC by Al included hot pressing Al powder with SiC fiber-SiC composite at 21-31 MPa and 1700 ºC in vacuum. Analysis of the interfacial bond showed the formation of weak interfacial layers made of $Al_4C_3$ and $Al_4SiC_4$. The weak interfacial bond is responsible for the debonding and pullout of the fibers during mechanical test. Moreover, the $Al_4SiC_4$ interfacial bond has been associated with a significant increase in the strain to failure without affecting the fracture strength. The increase in the strain under mechanical loading is not desirable for optoelectronic applications that require dimensional stability [22].

Recent publications have demonstrated a novel SiC processing technology based on engineering the physicochemical properties of the surface of the material [23-27]. The creation of a nanoscale thin silica-gel layer on SiC particles facilitated low processing temperature in the range (800 ºC – 1000 ˚C), densification and strengthening of 3D SiC objects [26]. The silica gel layer nucleated the growth of crystalline silica nano wires inside the pores of the silicon carbide matrix resulting in a significant increase in the density and strength. This new mechanism of densification and strengthening of the porous SiC takes place without any measurable changes in the dimensions of the 3D objects. However, complete densification of porous SiC by silica nanowire growth is yet to be reported. Moreover, the relatively low melting point of cristobalite ($SiO_2$, 1713 ºC) compared to SiC may limit high temperature applications.

The present study hypothesized that the silica gel layer can promote reaction with mineral binders such as cordierite and spodumene to establish in situ mineralization at the interface between SiC particles. The ionic diffusion of Al from the minerals to the silica gel layer will create ionic concentration gradient between mineral binders and SiC that promotes a strong

interfacial bond responsible for the transduction of thermal and mechanical energy (Figure 4.1). To test these hypotheses, SiC was treated with NaOH at room temperature to create surface silanol groups. The surface modified SiC was mixed separately with Cordierite (Cord) or Spodumene (Spod), pressed at 250 MPa and sintered in the temperature range 800-1200 °C. The mechanical and thermal properties of the composites are measured as a function of processing parameters. Moreover, polishing ability of the composites to a mirror surface finish is reported. Taking all together the SiC-mineral composites can serve as a future space mirror material.

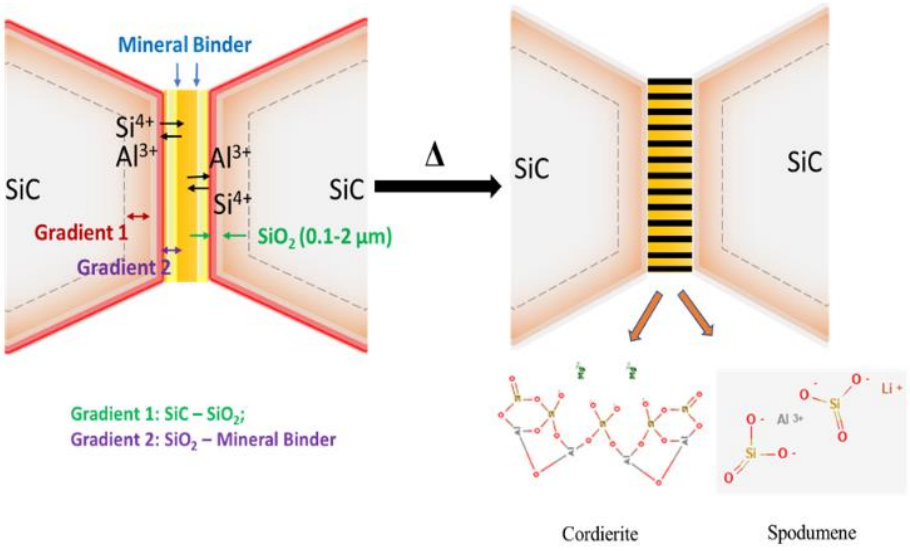


FIGURE 4.1: Graphical representation of the mechanism of the strong interfacial bonding in SiC-mineral binder composites [27]

## 4.2. MATERIALS AND METHODS

### 4.2.1 Preparation of Mineral Binders

Cordierite ($Mg_2Al_4Si_5O_{18}$) and Spodumene ($LiAlSi_2O_6$) were prepared by mixing appropriate stochiometric ratios of the ingredients [28-30]. The ingredient powder (40 gm) for each mineral was mixed with (70 ml) of ethanol and then milled in a high-energy planetary ball mill with powder to balls (6.23 mm) ratio of 1:10 at 180 rpm for 2 hrs. The powder mix was transferred into an alumina crucible and dried in an oven at 100 °C overnight. The balls were separated from the powder by sifting in ASTM standard sieves (mesh #60, #120, and #200). The powder was placed in an alumina crucible and sintered at: Spodumene 1000 °C/2hrs and Cordierite 1400 °C/2hrs at 1 °C/min. The phase composition was analyzed by XRD.

### 4.2.2. Preparation of SiC-Mineral Composites

SiC particles (US research nanomaterials, Houston, TX USA) with an average particle size of 40 μm was treated with 1% NaOH to create a silica gel surface layer. The formation of the silica gel layer through the surface activation technique at room temperature was discussed in the previous studies from our lab [23-27]. The surface-activated SiC was mixed separately with each mineral at a ratio 80% SiC: 20% mineral binder. The selected 80/20 ratio was based on a preliminary study that showed enhanced densification and mechanical properties without deformation during thermal treatment. Discs (10 mm diameter x 6 mm height) were prepared by pressing 1 gm of the SiC-mineral mixture in a tungsten carbide die at 250 MPa in a hydraulic press. The pressed green discs were sintered at 1200 ºC for 8 hours at a heating rate of 5ºC/min. Preliminary studies showed that treatment at a temperature higher than 1200 °C results in deformation due to melting of the mineral phase.

4.2.3 Structure Analysis

4.2.3.1. XRD analysis

X-Ray Diffraction analysis (XRD) was used to determine the crystalline structure of each composite. A PANalytical X'Pert Pro/MRD was used for all scans. The discs were ground to a powder and adhered to a silicon zero background disk with double-sided tape. The scanning X-ray beam was Ni-filtered Cu K alpha radiation with a wavelength of 1.54 Å. Radiation was produced at 45 kV and 40 mA. Incident beam optics included a 0.76 mm divergence slit and a 0.1 mm receiving slit. Scan time per step was 0.5 sec and the 2θ range was from 5° to 100°.

4.2.3.2. SEM/EDX morphology analysis

SEM fracture surface analysis of composite samples after compression test was performed using JEOL 6480 Scanning Electron Microscope (SEM). The samples were sputter coated with gold (10 nm thickness) and scanned in a secondary electron mode at 20 kV with a working distance of 10 mm.

4.2.4. Characterization of Properties

4.2.4.1. Density Measurements

Density of the sintered discs were measured using Archimedes principle (OHAUS Corporation, Parsippany, NJ, USA). The weights of the sample in air and in auxiliary liquid (deionized water) were measured for each composite (n = 7) at ambient atmospheres. The density was calculated using Eq. 4.1.

$$\rho = \frac{A}{A-B}\,(\rho_0 - \rho_L) + \rho_L \tag{4.1}$$

where,

$\rho$ = density of the sample,

A = weight of the sample in air,

B = weight of the sample in the auxiliary liquid,

$\rho_0$ = density of the auxiliary liquid,

$\rho_L$= density of the air (0.0012 g/cm$^3$).

The density of SiC discs obtained using Archimedes principle was compared to the theoretical values calculated using the actual density of each pure phase [SiC (3.2 g/cc), cordierite is 3.11 g/cc and spodumene is 2.8 g/cc] and the rule of mixtures.

4.2.4.2. Polishing protocol of SiC-Mineral composites

The composite discs were lapped using SiC papers grit size # 320, 400, 800, 1200 and 2400 (ANSI/CAMI standard (B74. 18-1996)) on Buehler grinding wheels at 200 rpm with water as a medium. The lapped discs were polished using MetaDiSupreme Diamond slurry of 6 µm and then 1 µm on a Verdutex polishing pad. Fine polishing of the sample was done using colloidal amorphous silica (0.06 µm) and non-crystallizing silica (0.01 µm) on a MasterTex polishing cloth (Buehler, Lake Bluff, Illinois). For each polishing step, the leveling of the surface was checked by Olympus DSX1000 microscope. The surface roughness of the final polished samples was measured using an atomic force microscope (AFM).

4.2.4.3. Atomic Force Microscopy Roughness Measurements

The surface roughness of the polished sample was measured using tapping mode AFM (Digital Instruments Nanoscope IIIm, Plainview, NY). The drive frequency ranged from 200 to 400 kHz, the set point was approximately 0-2 V, and the drive amplitude was 24 mV. In order to

obtain the general surface roughness, a large area of 3886.4 μm$^2$ was selected within which three spots (n=3) were scanned. The magnified images of the scanned areas were then plane fitted to the first order to remove the tilt artifacts due to the orientation of the particles in the composite. An area of 100 μm$^2$ was used to measure the roughness of individual SiC particles and an area of 600 μm$^2$ was used to measure the roughness of the bonded SiC particles.

4.2.4.4. Mechanical Property measurements

4.2.4.4.1. Hardness measurements

The hardness of the composite was measured using Vickers's Hardness tester (Wilson instruments, 402MVD). Vicker's indentation method uses a large indenter with indentation mark that covers all micro constituents of the composite. The machine uses a pyramid shaped diamond indenter with applied load of 4.9 N (500 gf). Indentations were made at 11 different locations on each sample and the average dimensions of each indentation was measured and used to calculate the hardness. The measurements of the diagonals were done using an optical microscope (Olympus DSX1000) at an objective lens of 40x magnification. The Hardness value HV (GPa) was calculated using Eq. (4.2):

$$HV = \frac{P}{d_a^2} \tag{4.2}$$

Where P is the applied load in Kg, $d_a^2$ is the average of the indented diagonal dimensions $d_1$ and $d_2$ in mm.

4.2.4.4.2. Strength and Modulus of Elasticity

The compressive strength of the thermally treated SiC-Cord and SiC-Spod discs were measured from the stress-strain curve obtained from the uniaxial compression using an Instron machine (Instron 5582, Norwood, MA) at a rate of 0.02 in /min until failure. The Modulus of elasticity of the SiC-mineral composites was measured using a nano-indenter (Agilent MTS G200, USA) that uses a three-sided pyramid Berkovich diamond indenter tip. The modulus is measured by a dynamic method, named CSM (continuous stiffness measurement), the properties being measured as a function of the indentation depth. A continuous indentation at a maximum load of 50 gf (490 mN) with a 10s hold time was applied. The mechanical properties were then derived using the Oliver-Parr technique using the below equations. The stiffness is calculated from the slope of the load vs depth curve according to Eq. 4.3.

$$S = \frac{dP}{dh} \tag{4.3}$$

The elastic modulus of each phase was calculated using equation (4.4)

$$\frac{1}{E_m} = \frac{(1-\nu^2{}_s)}{E_s} + \frac{(1-\nu^2{}_i)}{E_i} \tag{4.4}$$

where,

$\nu_s$ = Poisson ratio of the phase

$\nu_i$ = Poisson ratio of the indenter

$E_s$= elastic modulus of the phase

$E_i$= elastic modulus of the indenter

$E_m$=reduced contact modulus between the tip and the sample

The reduced contact modulus was found using the stiffness value found in Equation 3 and the projected contact area. The projected contact area is linked to the contact depth $h_c$ by the tip geometry, for a perfect pyramidal indenter:

$$E_m = \frac{S}{2}\sqrt{\frac{\pi}{A_c}} \quad (4.5)$$

The overall modulus of elasticity of each composite was calculated using the rule of mixtures and the elasticity of each phase in the composite.

4.2.4.4.3. Thermal Shock Test

The sintered SiC-Cordierite (SiC-Cord) and SiC-Spodumene (SiC-Spod) discs (n=7) were re-heated at 1200 ºC and held for 30 mins in Carbolite Gero (Verder Scientific, Hope valley, England) furnace then quenched in water at 22 ºC. The compression strength of the quenched samples was measured before and after thermal shock. The dimensional stability of the composites was determined by measuring the length and the diameter of the sample before and after the thermal shock. The strength of the samples was measured after thermal shock using the same method mentioned above. The fracture surface of the samples after the thermal shock was analyzed by SEM-EDX to study the failure mechanism.

4.2.4.5. Thermal Property Measurements

Thermal expansion coefficient of the SiC-Mineral composites was measured using a dual channel NETZSCH DIL 402 Expedis Supreme Pushrod Dilatometer using ASTM E 473-85 test method [31,32]. The samples were tested in one channel with a NIST Standard Reference Material (SRM) 731L1 Borosilicate Glass calibration standard in the second channel for calibration. Samples were heated to 100°C, held for 10 minutes for temperature stabilization, then continuously cooled at 2°C/min to -100°C.

Thermal conductivity (λ) was calculated from the thermal diffusivity using Eq. 4.6. The thermal diffusivity (D) and specific heat capacity ($C_p$) were measured at temperatures -100, 0, 100, 300, 600, 900, and 1000 ºC by the flash method using a NETZSCH LFA 467 HT HyperFlashTM instrument. The test method conforms to ASTM E1461-13, "Standard Test Method for Thermal Diffusivity by the Flash Method" [33,34]. The measurement of the thermal diffusivity of a material is usually carried out by rapidly heating one side of a sample and measuring the temperature rise curve on the opposite side. The sample is normally a disc with a standard diameter of 12.7 or 25.4 mm. Once the sample has been stabilized at the desired temperature, the power source is fired multiple times over a span of a few minutes and the necessary data is recorded for each "shot". The time that it takes for the heat to travel through the sample and cause the temperature to rise on the rear face can be used to determine the through-plane diffusivity. The resulting rear surface temperature rise is fairly small, ranging from about 0.5ºC to 2ºC.

$$\lambda = D(Cp * \rho) \tag{4.6}$$

where:

D = thermal diffusivity

λ = thermal conductivity

$C_p$ = specific heat

ρ = density

4.2.4.6. Electrical Property measurements

The electrical resistivities of the SiC-mineral composites were obtained through electrical conductivities using Eq. (4.7) and (4.8),

$$\rho = \frac{1}{\sigma} \tag{4.7}$$

where,

ρ is the electrical resistivity (Ωm),

σ is the electrical conductivity and is measured by,

$$\sigma = \frac{1}{R}\frac{L}{A} \tag{4.8}$$

where,

R is the resistance (Ω)

L is the length of the conductor in meters or cm

A is the cross-sectional area ($m^2$ or $cm^2$)

For the electrical conductivity measurements, the SiC-mineral composites of thickness ~1mm were arranged into a coin cell as in Figure 4.2 below. Either side of the crimped coin cell was then welded with the stainless-steel sheets to obtain contact with the positive and negative of the potentiostat.

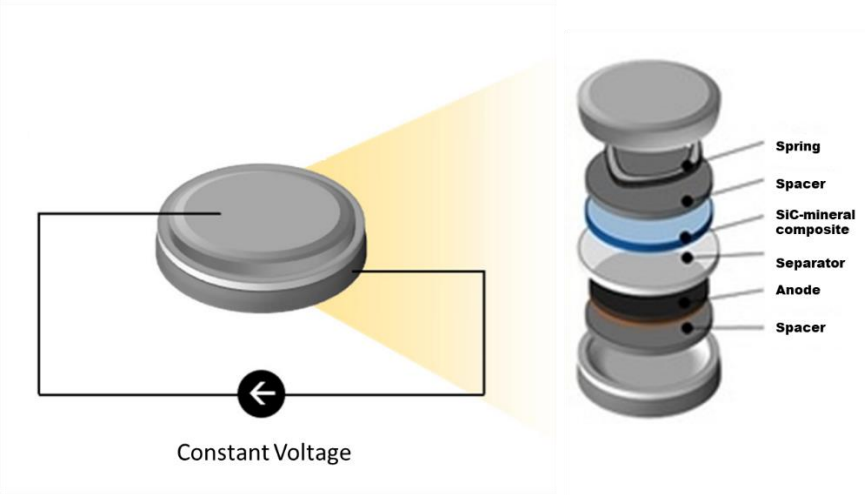


FIGURE 4.2: Coin cell set up of SiC-mineral composite for electrical conductivity measurements using constant voltage, the Figure was edited from ref [34].

A potentiostat (BioLogic SP-50, France) with EC-LAB control/data acquisition software was used to maintain constant potentials of 5V across the Pt mesh electrodes and simultaneously measure the resulting current through the protonic and electronic resistance measurement (PEM) mode at room temperature. These applied potentials were chosen so that the operational range of the potentiostat was not exceeded. The resulting current and resistance values were then used to calculate the electrical conductivity of the composites.

## 4.3. Results

### 4.3.1. X-Ray diffraction

Figure 4.3 below shows XRD analysis of the phase composition of control SiC, SiC-Cord and SiC-Spod after treatment at 1200 °C. Thermal treatment of control SiC showed the characteristic signals of α-SiC at d spacing 2.63, 2.52 and 2.36 nm and of Cristobalite at d spacing 0.41 nm. After the addition of mineral binders, the crystallite size, lattice parameters, and percentage of these phases were changed (Tables 4.1 and 4.2). The characteristic peaks for Cord, Spod, and Cristobalite showed a slight shift in the d spacing indicating ionic diffusion that led to the formation of a solid solution of each phase. Moreover, the change in crystallite size of cristobalite upon the introduction of mineral binders is shown in Table 4.1. Analysis of the lattice constants showed a difference in the a and c lattice parameters of the α-SiC phase in all SiC composites (Table 4.2). Maud rietveld analysis showed the percentages of phases in SiC-Cordierite composite are presented in Table 4.3. It is interesting to note that the addition of the mineral binders to SiC-Cris was associated with a decrease in percentages of cristobalite, SiC and the mineral binders compared to the initial phase composition prior to sintering.

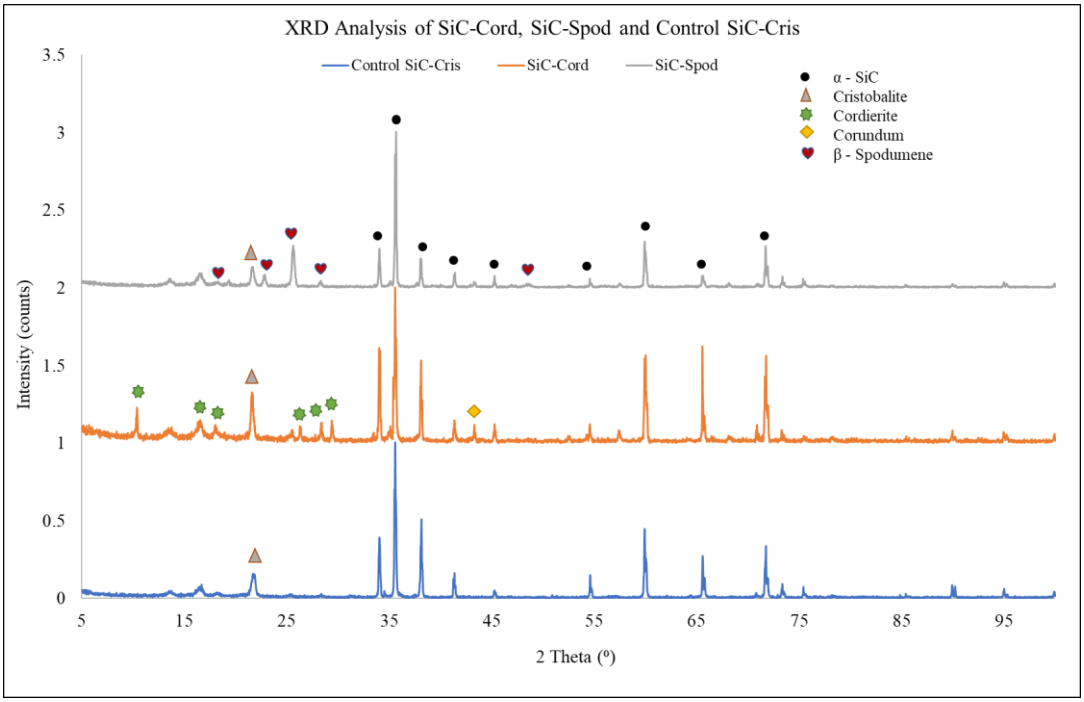


FIGURE 4.3: X-ray diffraction analysis showing the presence of phases of SiC, cristobalite, and mineral binders in the composites.

TABLE 4.1: Crystallite size of α-cristobalite and α-SiC in SiC-Mineral binder composites

| Crystallite size of Cristobalite (101) plane (in nm) | | |
|---|---|---|
| SiC-Cris | SiC-Cord | SiC-Spod |
| 18.43 | 27.29 | 24.35 |
| **Crystallite size of SiC (006) & (102) plane (in nm)** | | |
| SiC-Cris | SiC-Cord | SiC-Spod |
| 46.12 | 36.25 | 48.70 |

TABLE 4.2: Comparison of lattice constants of SiC-6H phase in SiC composites to the powder diffraction data.

| Lattice constants | SiC-6H PDF-01-075-8314 (in Å) | SiC-Cris (in Å) | SiC-Cord (in Å) | SiC-Spod (in Å) |
|---|---|---|---|---|
| a | 3.0810 | 3.0769 | 3.0830 | 3.0904 |
| c | 15.1248 | 15.1326 | 15.1326 | 15.0841 |
| a' (difference) | 0 | 0.0041 | -0.002 | -0.0094 |
| c' (difference) | 0 | -0.0078 | -0.0078 | 0.0407 |

TABLE 4.3: Quantitative analysis of the percentage composition of SiC-Mineral binder composites

| | SiC-Cris | SiC-Cord | SiC-Spod |
|---|---|---|---|
| α-SiC (%) | 89.87±3.11 | 78.61 ± 0.00 | 67.56 ± 1.82 |
| α-cristobalite (%) | 10.12±0.27 | 5.15 ± 0.34 | 7.08 ± 0.29 |
| β-cordierite (%) | N/A | 16.23 ± 0.90 | N/A |
| β-Spodumene (%) | N/A | N/A | 25.35 ± 0.0 |

4.3.2. SEM Morphology of the sintered SiC-mineral composite

The SEM micrographs (Figures 4.4a and 4.4b) show the fusion of the SiC particles by the mineral binders for SiC-Cord and SiC-Spod, respectively. The complete melting of the binders in the space between and on the surface of the SiC particles is strong evidence of the liquid phase sintering mechanism. EDS elemental composition analysis of the fracture surface showed a gradual decrease in the atomic percent of Al content from (5.5 atomic %) at the center of the bonding zone to (0.16 atomic %) at the SiC interface proving the diffusion of $Al^{3+}$ ions from mineral binder to the cristobalite layer on SiC surface (Figure. 4.4c).

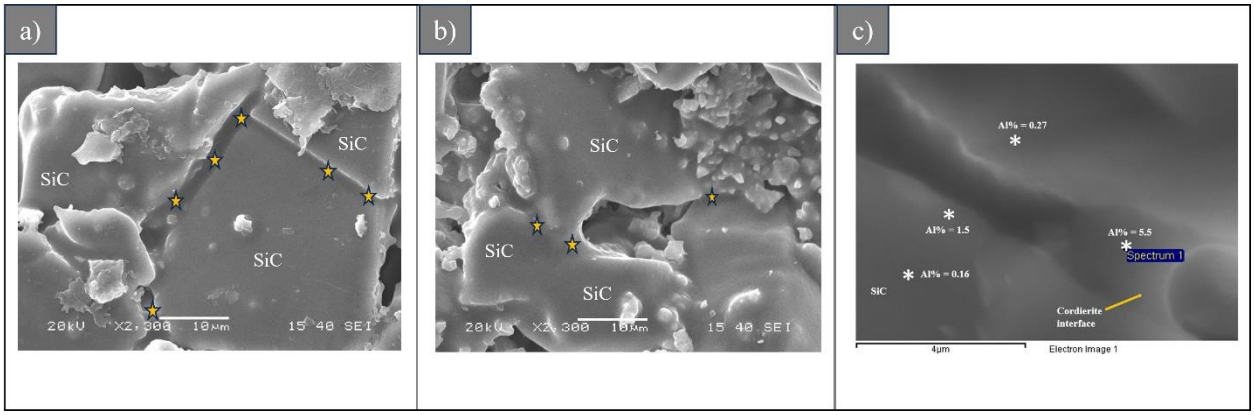


FIGURE 4.4: (a) SiC-Cordierite after sintering, (b) SiC-Spodumene after sintering (c) EDS micrograph showing variation in Al content due to the ionic migration of $Al^{3+}$ and $Si^{4+}$ between SiC and the interface. ☆ in a) and b) shows the bonding region between SiC particles comprised of cordierite and spodumene binders.

4.3.3. Density

The density of SiC-Cord and SiC-Spod samples were 2.74 ± 0.05 g/cm$^3$ and 2.61 ± 0.11 g/cm$^3$, respectively. Statistical analysis showed the density of SiC-Spod was significantly lower than that of SiC-Cord ($P < 0.03$). The light weight of the SiC-Cord and SiC-Spod composites are attributed to the relative low density of the mineral binders (Table 4). The apparent density measured by Archimedes for SiC-Cord and SiC-Spod are 86.2% and 83.5%, respectively of the theoretical density. The theoretical calculation of the density of each composite was done using the actual density of each pure phase.

TABLE 4.4: Comparison of the densities and the porosity percentage of SiC-Cord and SiC-Spod with data in the literature about SiC prepared by Chemical vapor Deposition (CVD), Reaction bonded (RB), Sintered, Hot pressed (HP) and Carbon (C) and Aluminum (Al) reinforced composites for space mirrors.

| Materials | Density ($g/cm^3$) | Porosity (%) |
|---|---|---|
| SiC-Cord | 2.74 | 13.80 |
| SiC-Spod | 2.61 | 16.50 |
| CVD SiC[64] | 3.21 | 0.00 |
| RB SiC[37] | 3.08 | 3.75 |
| Sintered SiC[64] | 3.1 | 3.12 |
| HP SiC[64] | 3.2 | 0.00 |
| C/SiC[64] | 2.6 | 18.75 |
| SiC/Al[38] | 2.94 | 8.13 |

4.3.4. Mirror surface finish of SiC-mineral binder composites

SiC-mineral binder composites were polished to a mirror finish using the conventional lapping and polishing technique mentioned in section 2.4.2. Figure 4.5 below shows the reflective surfaces of SiC-Cord and SiC-Spod.


FIGURE 4.5 (left to right): Reflectivity experiment using green laser light on the polished surface of SiC-Cord; Reflection of the letters UNC; Surface of SiC-Spod disc polished to mirror finish.

The general surface roughness of ($R_a$) of the polished surface was 343.58 nm, and the Ra roughness of areas comprised of SiC particles along with the mineral binder without pores was 20.89 nm. The mean roughness of the SiC microconstituent in the SiC-Cord composite was 2.37 ± 0.28 nm (Figure 4.6).

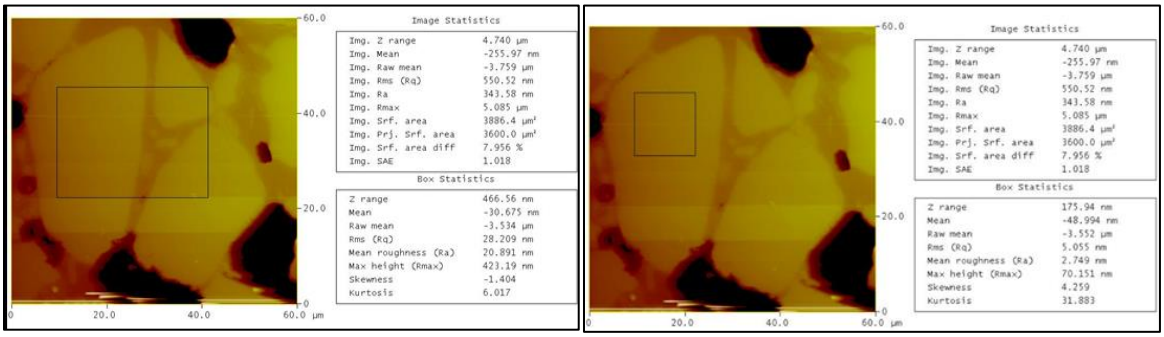


FIGURE 4.6: AFM images of the polished surface and its roughness analysis of the SiC-Cord composite.

4.3.5. Thermal Properties

The thermal expansion coefficient (α) (CTE) and the thermal strain ($\Delta L/L_0$) of SiC-Cord and SiC-Spod in the temperature range from -90 ºC to 80 ºC are shown in Figure 4.7(a and b). The CTE for SiC-Cord measured 0.58 x $10^{-6}$/ °C at -91.15 °C and 3.78 x $10^{-6}$/°C at 49.85 °C while that of SiC-Spod was 1.56 x $10^{-6}$/ °C at -91.15 °C and 3.68 x $10^{-6}$/°C at 49.85 °C (Figure 4.7. a). It can be noted that at -90 °C, the effect of the CTE of the binder is responsible for the observed lower CTE of SiC-Cord compared to SiC-Spod. The thermal conductivity measurements for SiC-Cord and SiC-Spod for the range of -100 °C to 1000 °C is shown in Figure 4.8.

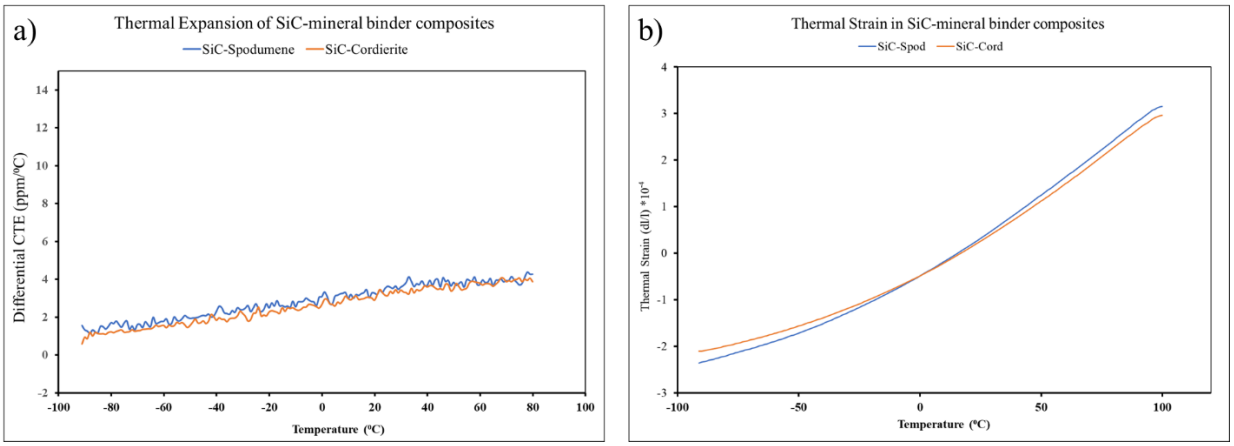


FIGURE 4.7: a) Thermodilatometry results showing temperature trends of differential thermal coefficient of expansion (α) and b) thermal Strain ($\Delta L/L_0$).

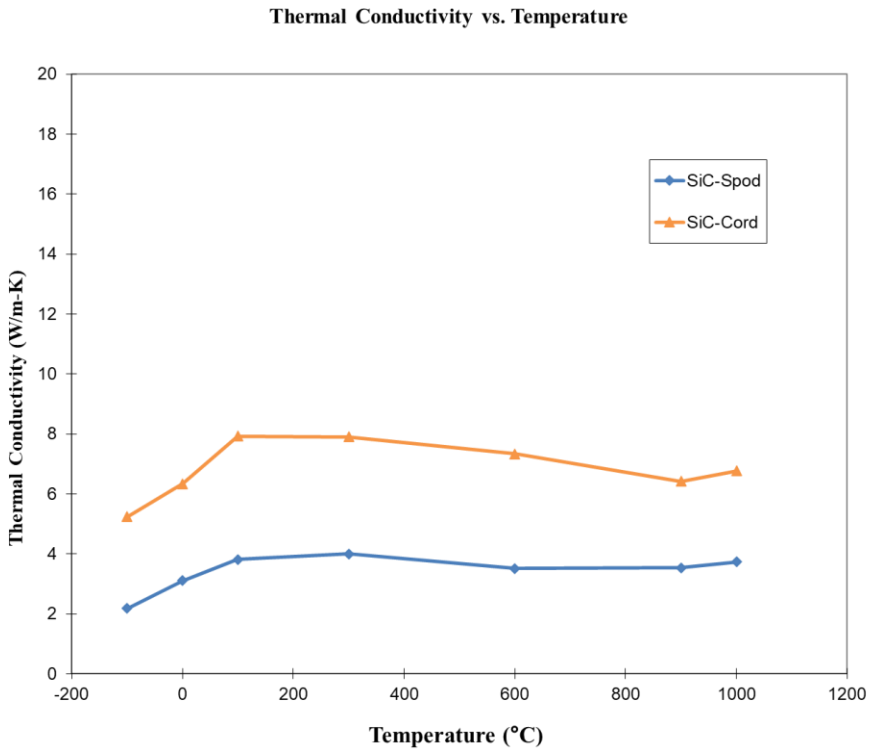


FIGURE 4.8: Thermal conductivity of SiC-Cord and SiC-Spod composites measured using "Standard Test Method for Thermal Diffusivity by the Flash Method."

4.3.6. Mechanical Properties:

The surface hardness of the polished surface of SiC-mineral composites measured 6.55 ± 1.25 GPa and 2.66 ± 0.87 GPa for SiC-Cord and SiC-Spod, respectively. The compression strength for SiC-Cord and SiC-Spod were 282.57 ± 37.94 and 184.58 ± 15.64 MPa, respectively (Figure 4.9). The elastic moduli for SiC and Cordierite micro constituents were 449.42 ± 29.52 GPa and 105.03 ± 16.08 GPa; respectively in the SiC-Cordierite composite. For the SiC-Spodumene composite, the modulus of elasticity for the SiC component measured 404.74 ± 68.98 GPa and that of spodumene measured 86.25 ± 33.29 GPa. Calculation of the moduli of elasticity of the composites based on the elasticity of the components using the rule of mixtures showed 380.54 ± 9.12 GPa for SiC-Cord and 341.04 ± 61.84 GPa for SiC-Spod (Figure 4.9).

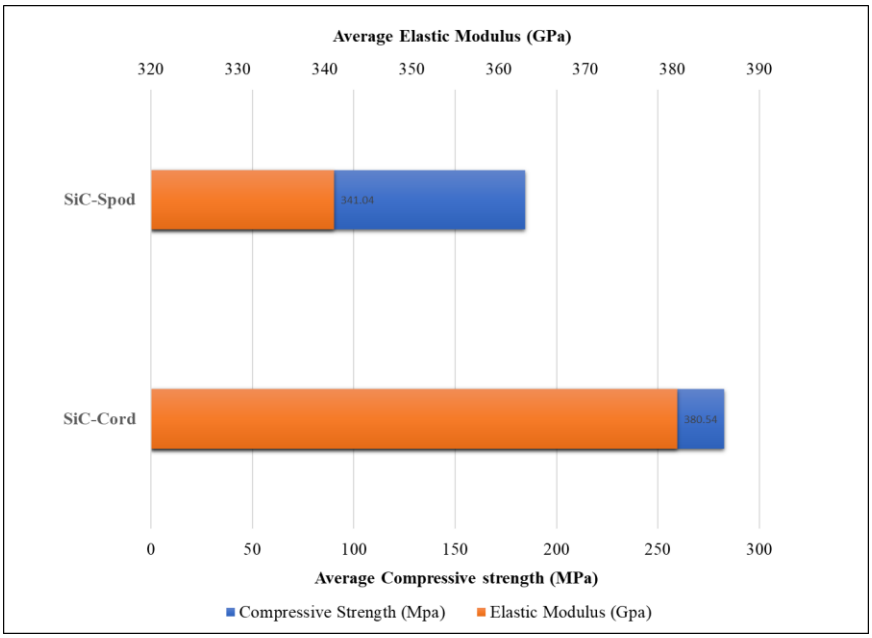


FIGURE 4.9: showing average compressive strength and elastic modulus for SiC-Cord, and SiC-Spod samples treated at 1200 °C for 8h.

4.3.7. SEM Morphology of the fractured surface

SEM analysis of the fracture surface showed a trans-granular fracture for both SiC-Cord (Figure 4.10a) and SiC-Spod (Figure 4.10b). The trans-granular fracture mechanism was accompanied by crack deflection created by the residual stress induced by the differences in CTE of microconstituents. SEM analysis also showed evidence of crack branching (Figure 4.10a and 4.10b).

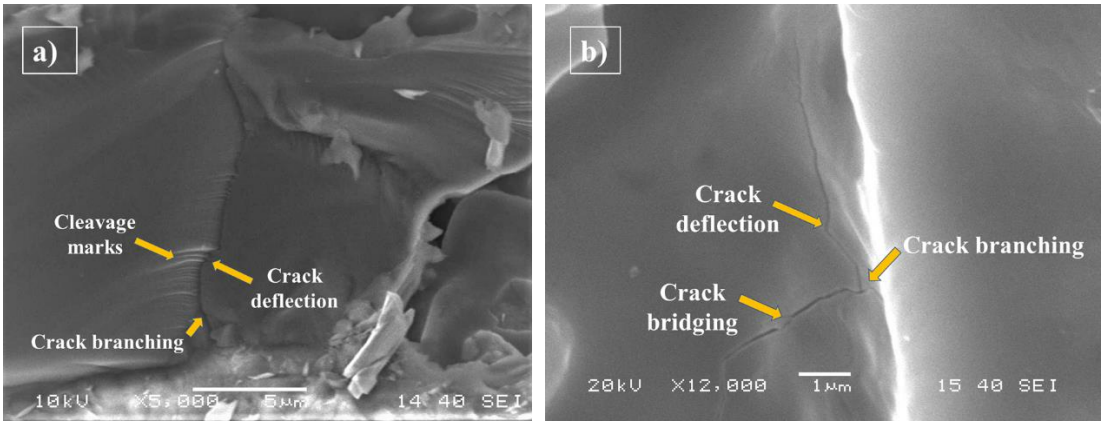


FIGURE 4.10: SEM micrograph showing transgranular fracture, crack deflection, crack bridging, and crack branching of the mineral binder composites of a) SiC-Cord and b) SiC-Spod.

4.3.8. Thermal Shock Resistance

Statistical analysis showed no significant change in the compressive strength for all SiC-mineral composites before and after thermal shock (Fig. 4.11a). The compressive strength and the strain to failure before and after thermal shock in water from 1200 ºC of the composite samples are shown in Figures 4.11a and 11b, respectively. Statistical analysis showed a significant decrease ($p < 0.0005$) in the strain to failure of control SiC-Cris after thermal shock. On the other hand, comparable strain to failure values were observed for SiC-Cord and SiC-Spod.

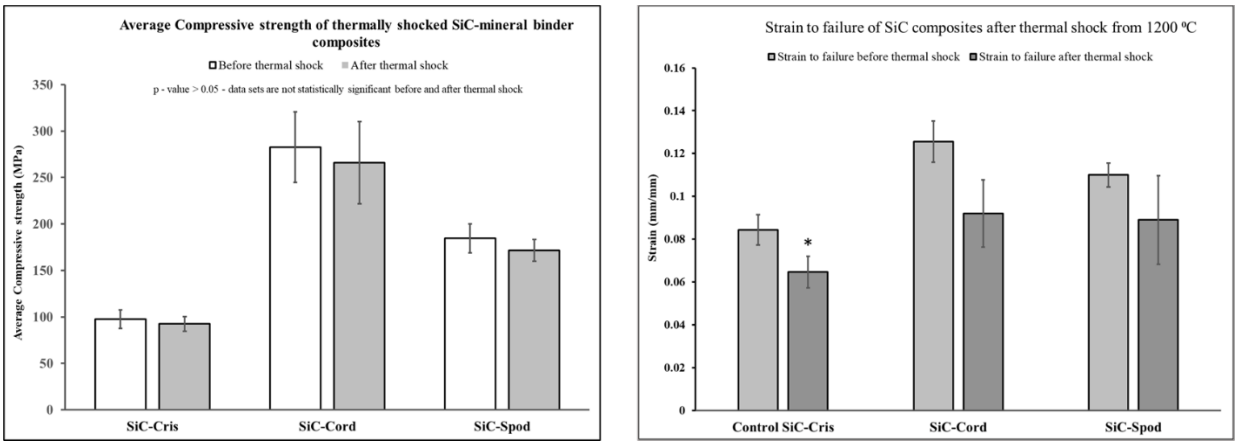


FIGURE 4.11: a) showing average compressive strength and b) showing strain to failure before and after thermal shock for control SiC-Cris, SiC-Cord, and SiC-Spod, quenched from 1200 °C to room temperature.

Moreover, the mechanical stability of the SiC-Cord after the thermal shock was associated with dimensional stability. (Figure 4.12) demonstrates the percent increase in diameter and height after thermal shock. The thermomechanical and dimensional stability of the SiC composites are mainly attributed to the smaller difference in the expansion coefficient between SiC and Cordierite or Spodumene.

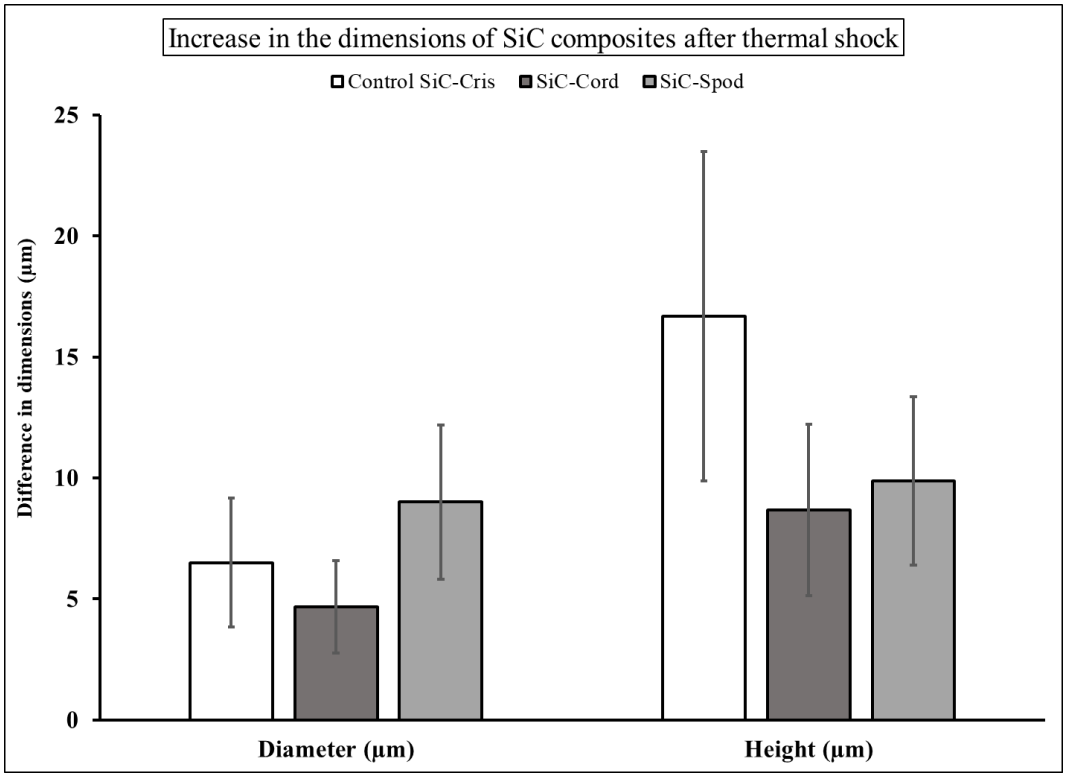


FIGURE 4.12: Increase in the dimensions in diameter and height of the SiC composite discs after thermal shock.

Table 4.5 summarizes the mechanical, thermal and electric properties of SiC-Cord and SiC-Spod in comparison to commercially available mirror materials like Cordierite CO720 (Kyocera, Elk Grove Village, IL), Zerodur Class 0 (Schott AG, Mainz, Germany) and SiC SPACE materials.

TABLE 4.5: Mechanical, thermal and electrical properties of SiC-mineral composites versus different mirror material [38]

| Property | Unit | SiC-Cord | SiC-Spod | Cordierite CO720 | Zerodur Class 0 | SiCSPACE |
|---|---|---|---|---|---|---|
| Young's Modulus E | GPa | 380.54 | 341.04 | 140 | 89 | 420 |
| Hardness | GPa | 6.55 | 2.87 | 8-8.5 | 6.08 | 22 |
| Density, ρ | $g/cm^3$ | 2.74 | 2.61 | 2.55 | 2.54 | 3.1-3.19 |
| Compression Strength | MPa | 282 | 184 | - | - | |
| CTE, α @23±5˚C | $10^{-6}/K$ | 3 | 3 | 0.02 | 0.05 | 2 |
| Thermal Conductivity, k @25˚C | W/m. K | 6.73 | 3.28 | 4.68 | 1.52 | 180 |
| Thermal Diffusivity | $10^{-6}$ $m^2/s$ | 5.48 | 2.23 | 2.37 | 0.75 | 84 |
| Specific Heat Capacity | J/g. K | 0.57 | 0.70 | 0.78 | 0.78 | 0.68 |
| Specific Stiffness, E/ρ | $MPa.m^3/kg$ | 138.73 | 130.76 | 55.0 | 35.1 | 133 |
| Electrical resistivity | Ω.cm | 1.38 $x10^8$ | 1.34 $x10^8$ | $10^{14}$ | 2.6 x $10^{13}$ | $10^5$ |

4.4. Discussion

SiC-Cord and SiC-Spod composites are introduced as candidates for mirror materials and mirror blanks for space applications. SiC-Cord and SiC-Spod stand out as mirror materials due to their: (i) high stiffness, (ii) thermal stability, (iii) ease of manufacturing and (iv) ability to be polished to a shiny surface.

The specific stiffness of SiC-Cord is 138.73 MPa $m^3$/kg and for SiC-Spod it is 130.76 MPa $m^3$/kg which is close to that of pure SiCSPACE (133 MPa $m^3$/kg) and significantly higher than that of Cord CO720 (55 MPa $m^3$/kg) and Zerodur (35.1 MPa $m^3$/kg). For space mirror applications, the specific stiffness is important as it refers to the structural weight of the component. Attempts to increase the specific stiffness of the composites include i) the addition of metal powders [40-42], ii) the addition of carbon or carbon-containing additives [43-45], iii) the addition of AlN additives [46]. These composites are hot-pressed, pressureless sintered, and spark-plasma sintered to obtain a high specific stiffness. The SPICA C/SiC mirror prepared by silicon infiltration with zero porosity showed a specific stiffness of 114.3 MPa $m^3$/kg [47]. Gyoung-Deuk Kim et.al., introduced strategies to increase the specific stiffness by reducing the density of composites by introducing pores, and adding additives that have low inherent density and increased modulus than SiC. The study showed that the addition of $B_4C$ which has lower density and higher modulus than SiC, increased the specific stiffness to 140 MPa $m^3$/kg [48]. However, carbon additives or $B_4C$ additives are prone to carbon contamination and require additional cleaning steps in optical applications [49]. The mechanical strength and fracture energy of cordierite is (250 MPa and 17.2 J/$m^2$, respectively which are greater than that of β-spodumene (150 MPa and 3.7 J/$m^2$, respectively) [50]. Therefore, the mechanical strength of the SiC-Cord composite was higher indicating the dominating role of the inherent strength. The

strength of the interfacial bond is further enhanced through the extensive ionic substitution that takes place at the interface between the surface silica and the Cord or Spod binders. The ionic traffic at the interface between the cordierite and the silica layer on SiC played an important role in phase transformation and strengthening the interfacial bond. The enhanced toughening is attributed to the crack deflections and crack branching (Figures 4.10a and 4.10b) redistributing the stress at the crack tip and increasing the energy to propagate the crack further into the composite [37]. In the case of fiber-reinforced composites, crack bridging happens when the applied stress is transferred to the fibers causing an elastic deformation that reduces the stress at the crack tip [51]. In the case of SiC-Cord and SiC-Spod composites, the crack bridging happens due to the residual stresses created on the SiC particle due to the strong interface of mineral binders which pushes the cracks together leading to crack closure (Figure 4.10b). The cleavage marks found in Figure 4.9a are representative of crack deflection [52]. The formation of crack deflection marks is due to the differences in the coefficient of thermal expansion of the present phases and is expected to increase the strength of the SiC/mineral binder composites. In the study of $Al_2O_3$ reinforced with SiC composite, the fracture strength was increased due to the transgranular failure mechanism caused by the pressure stresses on the grain boundaries caused by the reinforced nanoparticles [53]. Similarly, in SiC-Cord and SiC-Spod composites, the increased strength is due to the strong interfacial bond that created pressure stresses at the grain boundaries of SiC particles causing a transgranular failure. Therefore, the enhanced mechanical strength of SiC-Cord and SiC-Spod is attributed to three factors: i) a combination of crack deflection, crack branching, and crack bridging mechanisms, ii) transgranular failure due to the pressure stresses caused by the strong interfacial bond, iii) residual stress caused due to differences in thermal expansion among phases.

Materials used for mirror and mirror blank applications should have excellent thermal stability as they will be exposed to a large environmental change. It was reported that the dimensional variation of the mirror material with temperature can cause alignment drift in the optomechanical reference systems causing inaccurate measurements [54]. Measurements of the compressive strength of the SiC-mineral composites before and after thermal shock showed comparable values for each and a difference in the strain to failure was observed on the thermally shocked samples which is indicative of the thermal residual stresses created due to the differences in their thermal expansion coefficients. It was measured that the strain to failure decreased in the order of SiC-Spod (12.73%) < SiC-Cord (21.12%) < control SiC-Cris (23.81%). The dimensional stability measurements before and after thermal shock in Figure 4.12 showed a minimal increase in the diameter and height of the SiC-Cord and SiC-Spod composites. However, it showed a significant increase in height for the control SiC-Cris owing to the expansion of the cristobalite phase. The introduction of Cordierite and Spodumene minerals reduced the percentage reduction in the strain (dimensional change) upon thermal shock. Upon addition of the mineral binders such as cordierite and spodumene, crack sealing was observed in all composites during thermal shock. The crack healing and crack bridging process was facilitated due to the formation of the glassy phase of $SiO_2$, Mg/Li-based reacts which prevents cracks from growing [55–56].

The thermal expansion coefficient ($\alpha$) (CTE) and the thermal strain ($\Delta L/L_0$) of SiC-Cord and SiC-Spod in the temperature range from -90 ºC to 80 ºC are shown in Figure 4.7. The CTE for SiC-Cord measured 0.58 x $10^{-6}$/ °C at -91.15 °C and 3.78 x $10^{-6}$/°C at 49.85 °C while that of SiC-Spod was 1.56 x $10^{-6}$/ °C at -91.15 °C and 3.68 x $10^{-6}$/°C at 49.85 °C. It can be noted that at -90 °C, the effect of the CTE of the binder is responsible for the observed lower CTE of SiC-Cord compared to SiC-Spod. On the other hand, at 50 °C comparable values of the CTE were

recorded for the SiC-Cord and SiC-Spod which provides evidence of the ability of the surface activation treatment in creating a stable interface with mineral binders. The thermal conductivity of the SiC-Cord and SiC-Spod was 6.74 W/m. K and 3.28 W/m. K, respectively with an uncertainty of 0.07 (Figure 4.8). The thermal conductivities of SiC-Cord and SiC-Spod are lower than pure SiC ceramic. Such reduction in the thermal conductivities upon introduction of $Al_2O_3$-containing composites is expected due to the dissolved oxygen in the lattice of the non-oxide ceramic such as AlN and $Si_3N_4$. In the case of SiC, the presence of oxygen on the surface of SiC particles and the oxygen within the lattice of SiC grains are responsible for the detrimental effect on thermal conductivity. It was also reported that a larger volume percent of silicate secondary phases reduces the thermal diffusivity of the SiC composite [60]. However, these values are higher than those reported in the literature for commercially available mirror materials like Cordierite CO720 and Zerodur Class 0 which measured 4.68 W/m. K and 1.52 W/m. K, respectively. For both composites, the high percentage of SiC (80%) is responsible for the relative increase in the CTE and thermal conductivity compared to pure cord and Spod [62]. Therefore, the thermal properties of SiC-mineral binder composites can be tailored by modifying the ratio of SiC to mineral binders.

The differences in the lattice constants ‘a’ and ‘c’ of the composites (table 2) and the crystallite size of cristobalite in the mineral binder composites against control SiC-Cris (table 1) were measured. It was observed that both lattice parameters ‘a’ and ‘c’ showed a significant difference for SiC-Spod composites and SiC-Cord showed minimal to no change. The expansion in the c-axis of SiC-Spod is attributed to the changes in the bond angles between silica and alumina tetrahedra at the junction between SiC particles which was caused by the anisotropic thermal expansion of β-spodumene [63]. The changes in the lattice parameters are associated with strain

energy that induces mechanical strength and toughness of the mineral binder composites. The crystallite size of the cristobalite increased after the addition of mineral binders which was expected as the constituents of the composites formed a solid solution upon heat treatment at 1200 °C. Hence, the high thermomechanical and dimensional stabilities of the SiC-Cord and SiC-Spod can be attributed to the near-zero thermal expansion of the binder phases and the strong interfacial bond. Thus, the in-situ reaction between the silica layer on the SiC particles and the mineral binders created a bonding zone with transitional ionic concentration producing a composite that showed good thermo-mechanical properties.

The manufacturing of the SiC-mineral composites are done by sintering the pressed green bodies at 1200 °C (section 2.2). This is an innovative approach of sintering at a relatively low temperature using a surface activation technique [23-27]. This does not require techniques like high compact pressures including hot pressing and cold pressing, high-temperature sintering, sintering in controlled atmospheres, and glass melting. A strong interfacial bond between SiC particles was created by ionic substitution at the interface of SiC and the mineral binder. The density of SiC-Cord and SiC-Spod samples were $2.74 \pm 0.06$ g/cm$^3$ and $2.61 \pm 0.11$ g/cm$^3$, respectively. These values are lower than other mirror materials reported in the literature. For example, SiC mirrors processed by CVD, reaction bonding, or hot pressing had a density in the range of 3.1 – 3.2 g/cm$^3$ [64]. Metal-Matrix such as SiC/Al composite showed a density of 2.94 g/cm$^3$ [36]. In this study, the combination of lightweight cordierite (2.3 g/cc) and spodumene (2.4 g/cc) in SiC (3.2 g/cc) reduced the overall density of the composite.

Conventional SiC mirrors like SiCSPACE also require a CVD coating called cladding to obtain a mirror surface. This overcomes the difficulties of polishing pure SiC mirrors. However, the CVD technique possesses limitations that include: i) coating of large-size mirrors, ii) high

manufacturing cost, and iii) processing difficulties [38]. However, the novel sintering technique using silica gel and mineral binders in this study softens the edges and surface of the SiC particles by surface activation and solid solution formations that enable an easy mirror polish to the surface (Figure 4.5). On the other hand, choosing the right coating material is also crucial in polishing. The coating materials are chosen based on i) its removability, ii) smoothness to get polished, and iii) the close match of their CTEs. Hence silicon and fused silica were chosen as good coating materials for SiC [37]. Also, obtaining a mirror finish on a SiC composite is often challenging due to its abrasiveness and high surface hardness. In this study, the difficulties of getting a polished surface have been overcome by i) the formation of $SiO_2$ through surface activation, ii) including cordierite and spodumene as binders. The formation of a silica gel layer softens the rough edges of the SiC particles enabling smooth polishing. The high $R_a$ value obtained from AFM roughness analysis in section 3.4 is attributed to the difference in material removal between SiC and Mineral binder. However, that difference did not significantly affect the ability to polish the composite to a final mirror surface finish. Cordierite and Spodumene are silicate minerals used as mirror materials due to its smoothness and ease of polishing. Hence SiC-Cord and SiC-Spod composites can be used as mirror material without the need for a polishing layer. Also, the reflectivity of the surface of the SiC-Cord and SiC-Spod composites can be improved by controlling (i) the SiC to mineral binder ratio, (ii) the sintering parameters, (iii) and by adding fine polishing steps such as electropolishing.

## 4.5. Conclusions

The SiC-Cord and SiC -Spod composites exhibited excellent specific stiffness, thermal stability, low density, and a mirror surface finish. The Si-Al ionic substitution at the interface

between surface activated SiC and the mineral binder resulted in a strong interfacial bond with a gradient ionic concentration which facilitates thermal and mechanical signals transfers across phases. This facilitated high strength and modulus to the SiC-mineral composite. SiC-Cord and SiC-Spod composites showed good dimensional stability and reduction in strain-to-failure upon thermal shock were attributed to the strong interfacial bond and the low thermal expansion of the pure phases of cordierite and spodumene. The CTE at room temperature for SiC-Cord and SiC-Spod composites were 3 ppm/K and 3 ppm/K, respectively. These values are significantly lower than the CTE reported for commonly used spaceborne mirrors such as O-30 Be (11.4 ppm/K), 6061 Al (22.5 ppm/K), Mg (24.8 ppm/K), and TA6V (8.6 ppm/K). SiC-Cord and SiC-Spod composites also exhibited the capability to be polished to a mirror finish. It should be noted that commercially available cordierite and spodumene are glass-ceramics i.e., partially containing amorphous phase which affects the thermo mechanical properties of these materials. In our research, we prepared crystalline forms of cordierite and spodumene without prior glass preparation of either material. The mineral format of the binders among other structure parameters is responsible for the improved mechanical properties of SiC-Cord and SiC-Spod compared to the commercially available Zerodur and Cordierite. Therefore, SiC-Cord and SiC-Spod composite can be very well used for space mirrors. The applications of SiC-mineral composites can also be extended to power electronics as substrates for holding high-temperature components and as catalytic converters in automobile exhaust systems, filters, and in combustion engines.

# REFERENCES


1. Garoli, D., Rodriguez De Marcos, L. V., Larruquert, J. I., Corso, A. J., Proietti Zaccaria, R., & Pelizzo, M. G. (2020). Mirrors for space telescopes: Degradation issues. *Applied Sciences*, *10*(21), 7538.

2. Santi, G., Corso, A. J., & Pelizzo, M. G. (2021). Mirrors for space telescopes: degradation issues. *EUV and X-ray Optics, Sources, and Instrumentation*, *11776*, 9-19.

3. Gulati, S. T. (1996, November). Design considerations for mirror materials. In *Advanced materials for optical and precision structures* (Vol. 2857, pp. 2-11). SPIE.

4. Zhang, Y., Zhang, J., Han, J., He, X., & Yao, W. (2004). Large-scale fabrication of lightweight Si/SiC ceramic composite optical mirror. *Materials Letters*, *58*(7-8), 1204-1208.

5. Matson, L. E., & Mollenhauer, D. (2003, March). Advanced materials and processes for large, lightweight, space-based mirrors. In *2003 IEEE Aerospace Conference Proceedings (Cat. No. 03TH8652)* (Vol. 4, pp. 4_1681-4_1697). IEEE.

6. Guo, S., Zhang, G., Li, L., Wang, W., & Zhao, X. (2009). Effect of materials and modelling on the design of the space-based lightweight mirror. *Materials & Design*, *30*(1), 9-14.

7. Zhang, Z., Wang, B., Gong, H., Gu, Z., & Liu, Y. (2014, November). Research on materials for the large aperture space mirror. In *International Symposium on Optoelectronic Technology and Application 2014: Imaging Spectroscopy; and Telescopes and Large Optics* (Vol. 9298, pp. 294-299). SPIE.

8. Morrell, R. "The mineralogy and properties of sintered cordierite glass-ceramics." In *Proc. Br. Ceram. Soc (28), June, 1979*, p. 53. 1979.

9. Sandin, C. R., Allen, L. N., Amatucci, E. G., Arenberg, J. W., Carter, R. C., Corsetti, J. A., ... & Steeves, J. B. (2021). Materials evaluation for the origins space telescope. *Journal of Astronomical Telescopes, Instruments, and Systems*, *7*(1), 011011-011011.

10. Robichaud, Joseph, James J. Guregian, and Mark Schwalm. "SiC optics for Earth observing applications." In *Earth Observing Systems VIII*, vol. 5151, pp. 53-62. International Society for Optics and Photonics, 2003.

11. Zhang, Yumin, Jianhan Zhang, Jiecai Han, Xiaodong He, and Wang Yao. "Large-scale fabrication of lightweight Si/SiC ceramic composite optical mirror." *Materials Letters* 58, no. 7-8 (2004): 1204-1208.

12. Palusinski, Iwona A., and Isaac Ghozeil. "Developing SiC for optical system applications." In *Novel Optical Systems Design and Optimization VII*, vol. 5524, pp. 14-20. SPIE, 2004.

13. Harnisch, B., Kunkel, B., Deyerler, M., Bauereisen, S., & Papenburg, U. (1998). Ultra-lightweight C/SiC mirrors and structures. *ESA bulletin*, *95*(8), 148-152.

14. Shinoda, Yutaka, Takayuki Nagano, and Fumihiro Wakai. "Fabrication of nanograined silicon carbide by ultrahigh-pressure hot isostatic pressing." *Journal of the American Ceramic Society* 82, no. 3 (1999): 771-773.

15. Hu, Chunfeng, Fangzhi Li, Dong Qu, Qian Wang, Rongjun Xie, Haibin Zhang, Shuming Peng, Yiwang Bao, and Yanchun Zhou. "Developments in hot pressing (HP) and hot isostatic pressing (HIP) of ceramic matrix composites." In *Advances in Ceramic Matrix Composites*, pp. 177-202. Woodhead Publishing, 2014.

16. Tanaka, H., S. Somiya, and Y. Inomata. "Silicon Carbide Ceramics-1." *by S. Somiya and Y. Inomata, Elsevier Applied Science, London* (1991): 213-38.

17. Raju, Kati, and Dang-Hyok Yoon. "Sintering additives for SiC based on the reactivity: a review." *Ceramics International* 42, no. 16 (2016): 17947-17962.

18. Foster, D., and D. P. Thompson. "The use of MgO as a densification aid for α-SiC." *Journal of the European Ceramic Society* 19, no. 16 (1999): 2823-2831.

19. Dey, Atanu, Nijhuma Kayal, Atiar Rahaman Molla, and Omprakash Chakrabarti. "Investigation of thermal oxidation of Al2O3-coated SiC powder." *Thermochimica Acta* 583 (2014): 25-31.

20. Wilhelm, Matthias, Martin Kornfeld, and Werner Wruss. "Development of SiC–Si composites with fine-grained SiC microstructures." *Journal of the European Ceramic Society* 19, no. 12 (1999): 2155-2163.

21. Amirthan, G., and M. Balasubramanian. "Thermal conductivity studies on Si/SiC ceramic composites." *Ceramics International* 37, no. 1 (2011): 423-426.

22. Ding, Shuqiang, Sumin Zhu, Yu-Ping Zeng, and Dongliang Jiang. "Fabrication of mullite-bonded porous silicon carbide ceramics by in situ reaction bonding." *Journal of the European Ceramic Society* 27, no. 4 (2007): 2095-2102.

23. El-Ghannam, Ahmed, and Tony Schmitz. "Advanced 3D printing of silicon carbide-based optics through Amazon crystal growth, application number 62447641." (2017).

24. El-Ghannam, Ahmed, Madeline Greenier, Morgan Johnson, and Ian Marriott. "Synthesis and characterization of porous bioactive SiC tissue engineering scaffold." *Journal of Biomedical Materials Research Part A* 108, no. 11 (2020): 2162-2174.

25. Beasock, Damian, T. Michael Stokes, Ahmed El-Ghannam, and Tony Schmitz. "Effect of processing parameters on the microstructure and mechanical behavior of a silicon carbide-silica composite." *Procedia Manufacturing* 34 (2019): 747-753.

26. El-Ghannam, Ahmed, Sujithra Chandrasekaran, and Farjana Sultana. "Synthesis and characterization of a novel silica nanowire-reinforced SiC thermal material." *Journal of Solid-State Chemistry* 297 (2021): 122055.

27. Chandrasekaran, S., El-Ghannam, A., Monroe, J. A., & Xu, C. (2022, October). Thermo-Mechanical Properties of SiC-Mineral Binder Composites for Space Applications. In *ASME International Mechanical Engineering Congress and Exposition* (Vol. 86656, p. V003T04A004). American Society of Mechanical Engineers.

28. Cao, J., Shi, X., Zhang, C., Li, Z., Luo, N., & Cui, H. (2016, September). A study of synthesis of cordierite powder. In *6th International Conference on Mechatronics, Materials, Biotechnology and Environment (ICMMBE 2016)* (pp. 344-350). Atlantis Press.

29. Ghitulica, C., Andronescu, E., Nicola, O., Dicea, A., & Birsan, M. (2007). Preparation and characterization of cordierite powders. *Journal of the European Ceramic Society*, *27*(2-3), 711-713.

30. Yuan-Yuan, L., Gui-hua, L., Heng-Wei, Z., & Yi-Neng, H. (2020). Preparation and properties of spodumene/silicon carbide composite ceramic materials.

31. Mazurchevici, S. N., Vaideanu, D., Rapp, D., Varganici, C. D., Cărăușu, C., Boca, M., & Nedelcu, D. (2021). Dynamic Mechanical Analysis and Thermal Expansion of Lignin-Based Biopolymers. Polymers, 13(17), 2953.

32. Monroe, J. A., McAllister, J. S., Content, D. S., Zgarba, J., Huerta, X., & Karaman, I. (2018, July). Negative thermal expansion ALLVAR alloys for telescopes. In Advances in Optical and Mechanical Technologies for Telescopes and Instrumentation III (Vol. 10706, pp. 202-212). SPIE.

33. Cape J. and Lehman, G., "Temperature and Finite Pulse-Time Effects in the Flash Method for Measuring Thermal Diffusivity", J. Appl. Phys. 34, 1909 (1963).ASTM Committee E37 on Thermal Measurements. (2007). Standard Test Method for Determining Thermal Diffusivity by the Flash Method. ASTM International.

34. Möller, S., Joo, H., Rasinski, M., Mann, M., Figgemeier, E., & Finsterbusch, M. (2022). Quantitative Lithiation Depth Profiling in Silicon Containing Anodes Investigated by Ion Beam Analysis. Batteries, 8(2), 14.

35. Yan, Cui, Wang Lifeng, and Ren Jianyue. "Multi-functional SiC/Al composites for aerospace applications." Chinese Journal of Aeronautics 21, no. 6 (2008): 578-584.

36. Dutta, S. (2001). Fracture toughness and reliability in high-temperature structural ceramics and composites: prospects and challenges for the 21st century. *Bulletin of Materials Science*, *24*, 117-120.

37. Rodolfo, J., Ruch, E., Tarreau, M., Merceron, J. M., Ferré, J., Rousselet, N., ... & Harnisch, B. (2017, November). SIC mirrors polishing. In International Conference on Space Optics—ICSO 2014 (Vol. 10563, pp. 584-591). SPIE.

38. Bougoin, Michel. "SiC material and technology for space optics." In ICSO conference proceedings. 2000.

39. Li, J., Ren, X., Zhang, Y., & Hou, H. (2020). Porous process and its effects on the microstructure and properties of SiC ceramics sintered with Mg additive. *Journal of Materials Research and Technology*, *9*(1), 33-41.

40. Ray, D., Flinders, R. M., Anderson, A., Cutler, R. A., Campbell, J., & Adams, J. W. (2006). Effect of microstructure and mechanical properties on the ballistic performance of SiC-based ceramics. *Advances in Ceramic Armor II: Ceramic Engineering and Science Proceedings*, *27*, 85-96.

41. Carnahan, R. D. (1968). Elastic properties of silicon carbide. *Journal of the American Ceramic Society*, *51*(4), 223-224.

42. Magnani, G., Sico, G., Brentari, A., & Fabbri, P. (2014). Solid-state pressureless sintering of silicon carbide below 2000 C. *Journal of the European Ceramic Society*, *34*(15), 4095-4098.

43. Liu, M., Yang, Y., Wei, Y., Li, Y., Zhang, H., Liu, X., & Huang, Z. (2019). Preparation of dense and high-purity SiC ceramics by pressureless solid-state-sintering. *Ceramics International*, *45*(16), 19771-19776.

44. Yaşar, Z. A., & Haber, R. A. (2021). Evaluating the role of uniformity on the properties of B4C–SiC composites. *Ceramics International*, *47*(4), 4838-4844.

45. Ray, D., Flinders, R. M., Anderson, A., Cutler, R. A., Campbell, J., & Adams, J. W. (2006). Effect of microstructure and mechanical properties on the ballistic performance of SiC-based ceramics. *Advances in Ceramic Armor II: Ceramic Engineering and Science Proceedings*, *27*, 85-96.

46. Ozaki, T., Kume, M., Oshima, T., Nakagawa, T., Matsumoto, T., Kaneda, H., ... & Kroedel, M. (2005, August). Mechanical and thermal performance of C/SiC composites for SPICA mirror. In *Optical Materials and Structures Technologies II* (Vol. 5868, pp. 132-141). SPIE.

47. Kim, G. D., Kim, Y. W., Yong, S. M., & Jung, W. K. (2022). Improving specific stiffness of silicon carbide ceramics by adding boron carbide. *Journal of the European Ceramic Society*, *42*(15), 6827-6835.

48. Moreno Fernández, H., Rogler, D., Sauthier, G., Thomasset, M., Dietsch, R., Carlino, V., & Pellegrin, E. (2018). Characterization of carbon-contaminated B4C-coated optics after chemically selective cleaning with low-pressure RF plasma. *Scientific Reports*, *8*(1), 1293.

49. D.G. Grossman, Glass ceramics, Engineered Materials Handbook, Vol. 4 Ceramics and Glasses, ASM International, American Technical Publishers Ltd, Herts, UK (1991), pp. 170-176.

50. Naji, H. Z. S. M., Zebarjad, S. M., & Sajjadi, S. A. (2008). The effects of volume percent and aspect ratio of carbon fiber on fracture toughness of reinforced aluminum matrix composites. *Materials Science and Engineering: A*, *486*(1-2), 413-420.

51. Alireza Moradkhani, Hamidreza Baharvandi, Microstructural analysis of fracture surfaces and determination of mechanical properties of Al2O3–SiC–MgO nanocomposites, International Journal of Refractory Metals and Hard Materials, Volume 67, 2017, Pages 40-55, ISSN 0263-4368, https://doi.org/10.1016/j.ijrmhm.2017.05.004.

52. Sun, X., Li, J. G., Guo, S., Xiu, Z., Duan, K., & Hu, X. Z. (2005). Intragranular particle residual stress strengthening of $Al_2O_3$–SiC nanocomposites. *Journal of the American Ceramic Society*, *88*(6), 1536-1543.

53. Baskaran, R., Sivakumar, P., & Arivuoli, D. (2013). Dimensional stability of mirror materials for opto-mechanical reference system. *International Journal*, *8*(19), 997-1004.

54. T.P. Nguyen, Y. Pazhouhanfar, S.A. Delbari, A. Sabahi Namini, A. Babapoor, Y. Mohammadpourderakhshi, S. Shaddel, Q. Van Le, M. Shokouhimehr, M. Shahedi Asl, Physical, mechanical and microstructural characterization of TiC–ZrN ceramics, Ceram. Int. (2020), https://doi.org/10.1016/j.ceramint.2020.05.292.

55. T.P. Nguyen, M. Dashti Germi, Z. Hamidzadeh Mahaseni, S.A. Delbari, Q. Van Le, Z. Ahmadi, M. Shokouhimehr, A. Sabahi Namini, M. Shahedi Asl, Enhanced densification of spark plasma sintered $TiB_2$ ceramics with low content AlN additive, Ceram. Int. (2020), https://doi.org/10.1016/j.ceramint.2020.05.278.

56. M. Vajdi, M. Shahedi Asl, S. Nekahi, F. Sadegh Moghanlou, S. Jafargholinejad, M. Mohammadi, Numerical assessment of beryllium oxide as an alternative material for micro heat exchangers, Ceram. Int. (2020), https://doi.org/10.1016/j. ceramint.2020.04.263.

57. T.P. Nguyen, Y. Pazhouhanfar, S.A. Delbari, Q. Van Le, S. Shaddel, M. Pazhouhanfar, A. Sabahi Namini, M. Shokouhimehr, M. Shahedi Asl, Characterization of spark plasma sintered TiC ceramics reinforced with graphene nano-platelets, Ceram. Int. (2020), https://doi.org/10.1016/j.ceramint.2020.04. 189.

58. Sabahi Namini, S.A. Delbari, B. Nayebi, M. Shahedi Asl, S. Parvizi, Effect of B4C content on sintering behavior, microstructure and mechanical properties of Ti based composites fabricated via spark plasma sintering, Mater. Chem. Phys. 251 (2020) 123087, https://doi.org/10.1016/j.matchemphys.2020.123087.

59. F. Sharifianjazi, M. Moradi, N. Parvin, A. Nemati, A. Jafari Rad, N. Sheysi, A. Abouchenari, A. Mohammadi, S. Karbasi, Z. Ahmadi, A. Esmaeilkhanian, M. Irani, A. Pakseresht, S. Sahmani,

M. Shahedi Asl, Magnetic $CoFe_2O_4$ nanoparticles doped with metal ions: a review, Ceram. Int. (2020), https://doi.org/10. 1016/j.ceramint.2020.04.202.

60. Zhou, Y., Hirao, K., Watari, K., Yamauchi, Y., & Kanzaki, S. (2004). Thermal conductivity of silicon carbide densified with rare-earth oxide additives. Journal of the European Ceramic Society, 24(2), 265-270.

61. Khalil, N. M., and S. H. Kenawy. "In-Situ Cordierite–Silicon Carbide Composite." American Ceramic Society Bulletin 87, no. 7 (2009): 9201-9207.

62. Kelsey Jr, P. V., Schmunk, R. E., & Henslee, S. P. (1981). Preliminary evaluation of beta-spodumene as a fusion reactor structural material. Journal of Nuclear Materials, 103, 145-148.

63. Zhou, H., Zhang, C. R., Cao, Y. B., & Zhou, X. G. (2006, May). Lightweight C/SiC mirrors for space application. In 2nd International Symposium on Advanced Optical Manufacturing and Testing Technologies: Large Mirrors and Telescopes (Vol. 6148, pp. 169-174). SPIE.

# CHAPTER 5: CONCLUSION

The focus of the dissertation is to obtain processing techniques to successfully 3D print SiC composites. Secondary surface activation, use of mineral binders were two major phenomena which were used to achieve maximum densification and strengthening to the composites. 3D printed SiC samples were densified and strengthened using siloxane bonding and secondary surface activation. Further, by using SiC-mineral binders another post-treatment approach for 3D printed discs were obtained. The ionic diffusion of Al and Si at the interface of silica gel and the mineral binders created a strong adhesion between SiC particles. Due to which a trans granular failure mechanism was observed. Further, by characterizing the thermo-mechanical properties of SiC-mineral binder composites, it was found that they high strength, specific stiffness, low coefficient of thermal expansion, excellent thermal shock resistance, and comparable thermal conductivity which makes them a suitable candidate for space mirrors and high temperature applications.

Chapter 2 focused on the 3D printing of SiC in powder bed binder jet with water binder. To improve the green density of the printed part, coarse and fine particle sizes of SiC are homogenously mixed. The coarse particles of average particle size ~40 μm were pre-treated with NaOH to create silica gel layer at the room temperature. 70% of this pre-treated SiC was mixed with 15% of 2 μm and 15% of 600 nm randomly shaped particles of SiC. This combination of particle sizes enabled good spreading of the powders and mechanically filled the voids between particles. Further, the handling strength was improved by creating a siloxane bonding between particles of the as-printed green parts at 650 °C for 5 h. These discs were further impregnated in various concentrations of NaOH (1%, 10% and 20%) and various temperatures (800 ºC, 900 ºC,

1000 ºC) to improve its mechanical strength. The optimal concentration of NaOH, temperature, and dwell time were found to be 10%, 1000 °C, and 2h. At these processing parameters, the 3D printed samples showed excellent strength and dimensional stability.

Chapter 3 focused on creating a novel sintering technique to densify and strengthen SiC particles by introducing mineral binders such as cordierite and spodumene as a bonding material. Cordierite and spodumene are known for their excellent thermal stability and nearly zero thermal expansion coefficient. Strength of SiC-Cord and SiC-Spod were found to increase due to the lattice distortion and the ionic diffusion of $Al^{3+}$ into the silica layer at the interface with the mineral binder of the binder phase. The liquid phase transformation of the binders facilitated particle fusion and reduced the porosity percentage and the pores size. SiC-Cord and SiC-Spod samples showed excellent thermal shock resistance and dimensional stability after quenching in water from 1200 ºC. Results of the study suggest that the SiC-mineral binder composites can be used as thermal materials and can be used as a post-treatment technique for the samples that are 3D printed in powder bed binder jet.

Chapter 4 focused on commercializing the SiC-Cord and SiC -Spod composites for space applications. The strong interfacial bond with a gradient ionic concentration facilitated thermal and mechanical signals transfers across phases. This imparts the high strength and modulus to the SiC-mineral composite. SiC-Cord and SiC-Spod composites showed good dimensional stability and reduction in strain-to-failure upon thermal shock. A significantly low CTE at room temperature for SiC-Cord and SiC-Spod composites were 3 ppm/K and 3 ppm/K, respectively. These values are significantly lower than the CTE reported for commonly used spaceborne mirrors such as O-30 Be (11.4 ppm/K), 6061 Al (22.5 ppm/K), Mg (24.8 ppm/K), and TA6V (8.6 ppm/K). We were also able to obtain a mirror like surface finish with SiC-Cord and SiC-

Spod composites. Usually, the commercially available cordierite and zerodur are glass-ceramics i.e., partially containing amorphous phase which affects the thermo mechanical properties of these materials. In our research, we prepared crystalline forms of cordierite and spodumene without prior glass preparation of either material. The mineral format of the binders among with other structure parameters is responsible for the improved mechanical properties of SiC-Cord and SiC-Spod. Therefore, SiC-mineral binder composite can be very well used for space mirrors. The applications of SiC-mineral composites can also be extended to power electronics as substrates for holding high-temperature components and as catalytic converters in automobile exhaust systems, filters, and in combustion engines.

# APPENDIX A: DEPTH CURING DATA FROM DIGITAL LIGHT PRINTING (DLP)

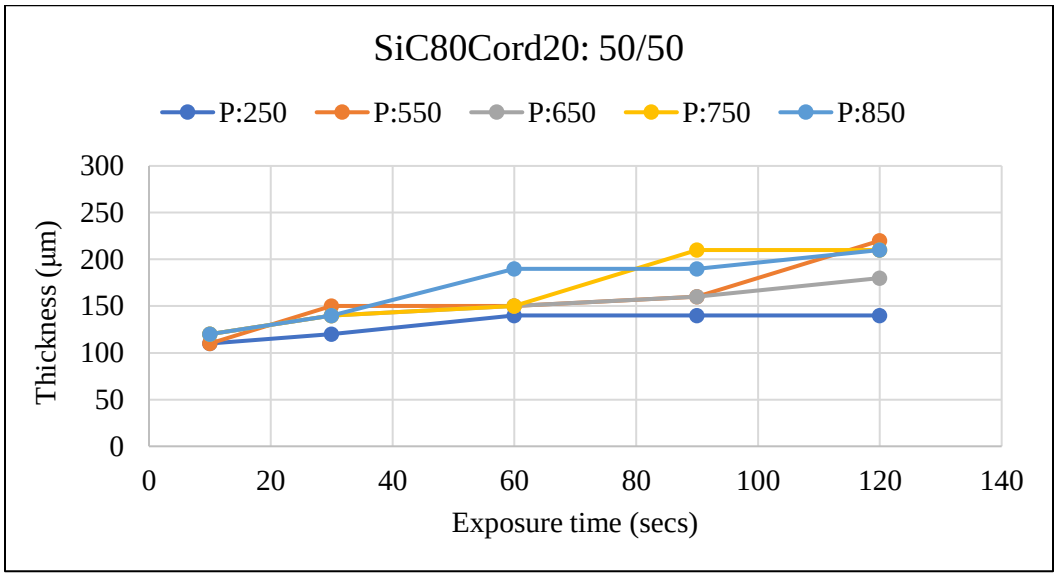


FIGURE A1: Thickness of one layer from depth curing of SiC-Cordierite composite at different exposure times at a loading of 50/50.

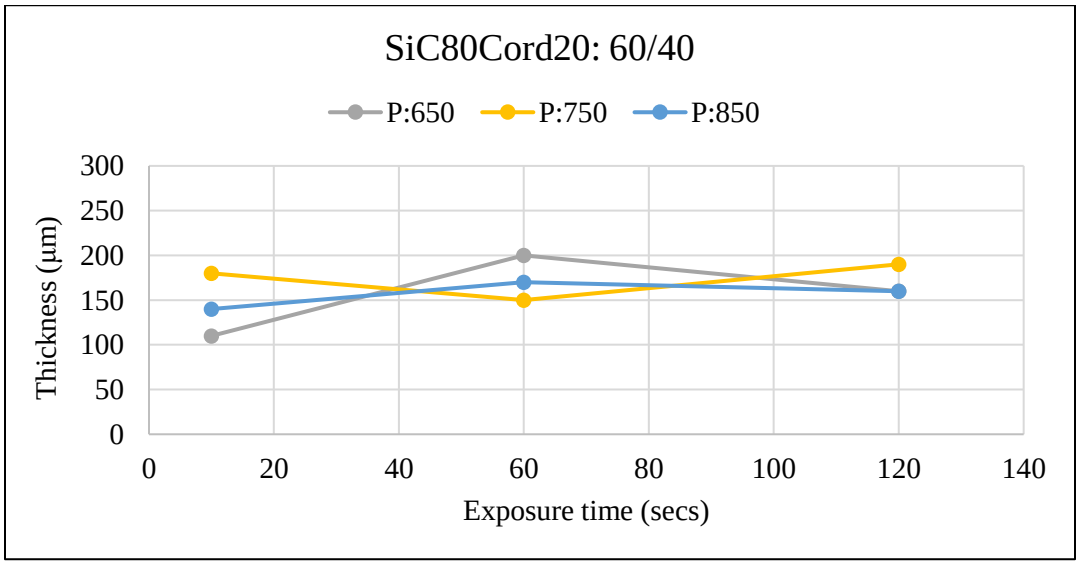


FIGURE A2: Thickness of one layer from depth curing of SiC-Cordierite composite at different exposure times at a loading of 60/40.

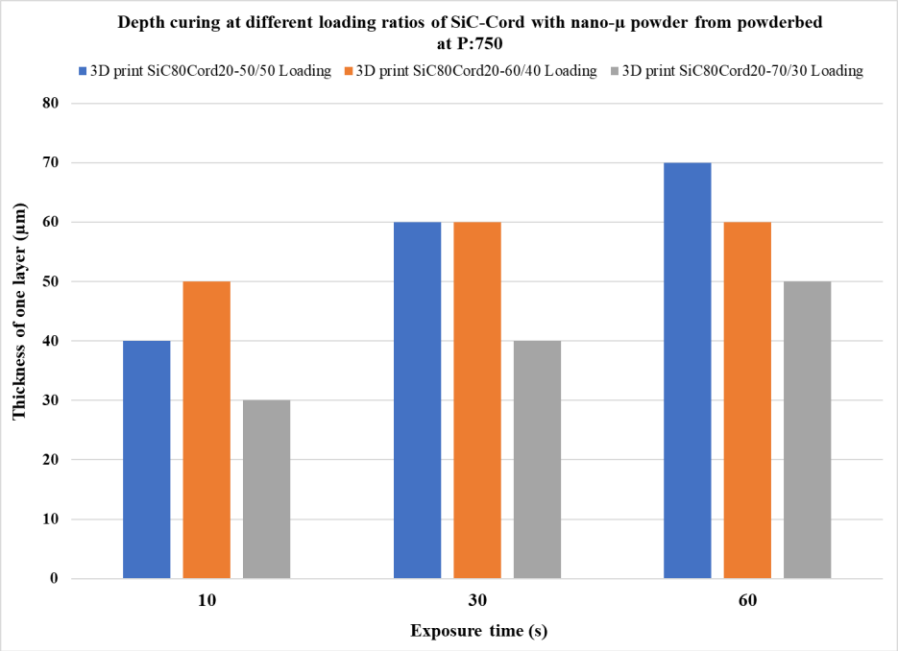


FIGURE A3: Thickness of one layer from depth curing of SiC-Cordierite composite at different exposure times and loading ratios. SiC powder used here is a combination of pre-treated 40 µm (70%), 2 µm (15%) and 600 nm (15%) at a power of 750.

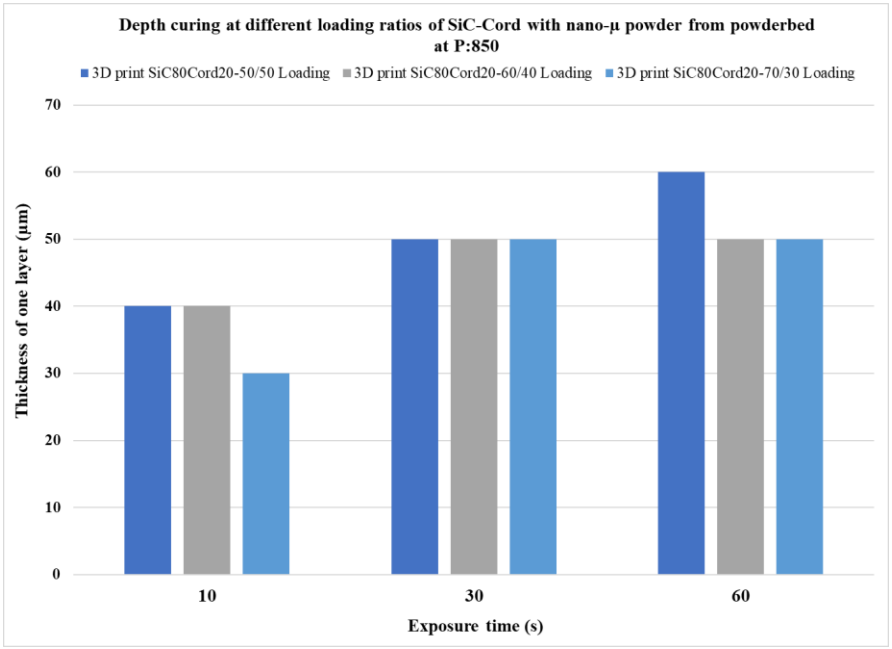


FIGURE A4: Thickness of one layer from depth curing of SiC-Cordierite composite at different exposure times and loading ratios. SiC powder used here is a combination of pre-treated 40 µm (70%), 2 µm (15%) and 600 nm (15%) at a power of 850.

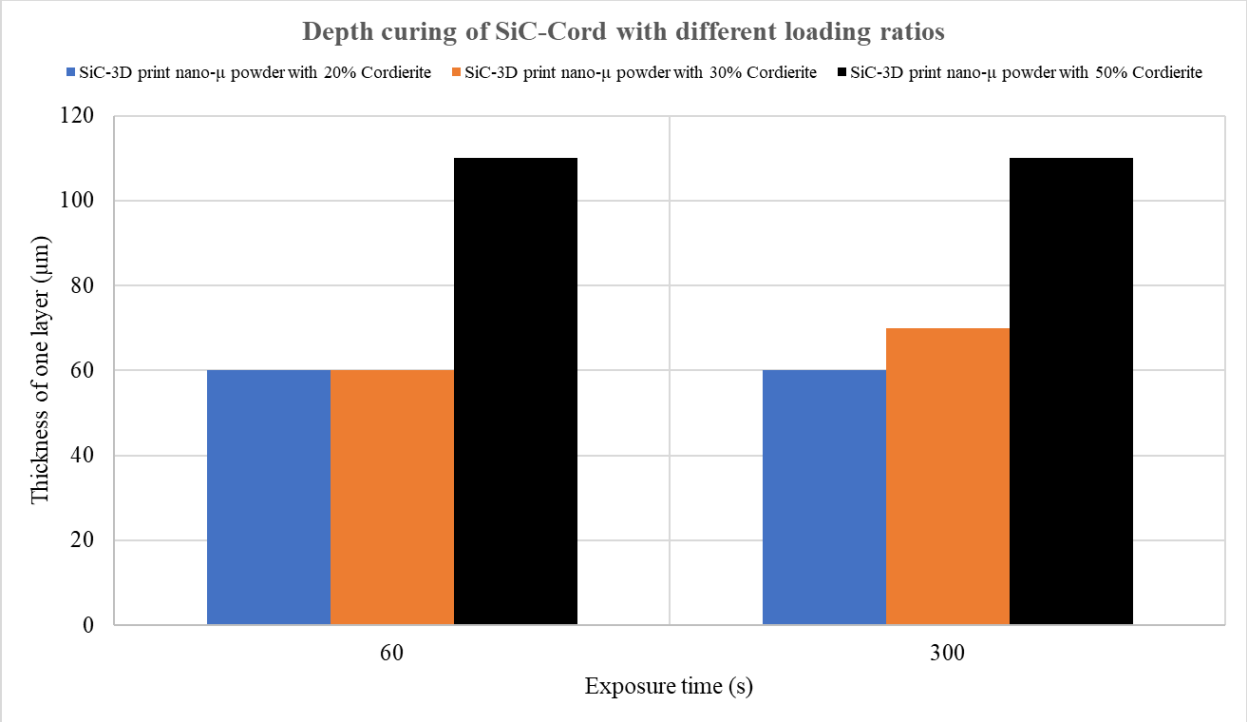


FIGURE A5: Thickness of one layer from depth curing of SiC-Cordierite composite with different ratios of cordierite at a loading ratio of 60/40 at a power of 750.